DEVELOPMENT OF A COMPUTER CONTROLLED FABRICATION SYSTEM FOR INTERVENTIONAL MAGNETIC RESONANCE IMAGING DEVICE PRODUCTION

by

Dursun Korel YILDIRIM

B.S., Mechatronics Sciences, Marmara University, 2010

Submitted to the Institute of Biomedical Engineering
in partial fulfillment of the requirements
for the degree of
Master of Science
in
Biomedical Engineering

Boğaziçi University
2016

ACKNOWLEDGMENTS

It is a priceless gift that having understanding and helpful people around in troublesome times. I feel this fortune through the duration of my thesis studies.

I would like to thank to my supervisors, Asst. Prof. Özgür Kocatürk and Prof. Cengizhan Öztürk. I was very pleased to work with them for all these years, and experience their patience and constructive guidance. I owe them so much for their priceless contributions to my knowledge and to this dissertation.

I also would like to thank a lot to Dr. Robert J. Lederman, Senior Investigator of Cardiovascular Intervention Program, (NHLBI, National Institutes of Health), and his team for sharing their facilities and for their invaluable contributions to the key issues during this thesis study.

Another person, who I would like to name here is Engin Baysoy whom I have always felt the support of. It is a rare thing for someone to be able to see the full side of the glass. And Engin added this study a lot with not only his academic skills, but also with his positive attitude. I also would like to thank to Ahmet Turan Talaş for his determination and his help with the clean room studies, which motivated our team to achieve the goals of this project.

There are some other dearest people without whom I could have some trouble to complete my studies. I would like to thank Zahid Sağıroğlu, who spent most of his time for understanding pain in the neck simulation software and saved me from time consuming calculations. I also would like to mention the names of Ozan Ertop and Emre İşeri here. They always make the time that I spend in the laboratory valuable.

I also would like to thank to my sisters Egemen Tarısever and Dilara Öcal for making the life better for me and for motivating me at the every step of this study.

Finally, I owe my greatest gratitude to my family for their priceless support which I always felt with me during my life and for always being either a phone call away or just beside of me to help for any trouble I had during this thesis study.

ACADEMIC ETHICS AND INTEGRITY STATEMENT

I, Dursun Korel Yıldırım, hereby certify that I am aware of the Academic Ethics and Integrity Policy issued by the Council of Higher Education (YÖK) and I fully acknowledge all the consequences due to its violation by plagiarism or any other way.

Name : Signature:

Date:

ABSTRACT

DEVELOPMENT OF A COMPUTER CONTROLLED FABRICATION SYSTEM FOR INTERVENTIONAL MAGNETIC RESONANCE IMAGING DEVICE PRODUCTION

Magnetic Resonance Imaging (MRI) is a promising candidate against X-Ray fluoroscopy for interventional cardiovascular procedures due to its ionizing radiation free mechanism and superior soft tissue contrast. However, Interventıonal MRI fıeld lacks of dedicated clinical grade MRI safe and visible devices. Aim of this thesis study is to design and develop a Computer Numerical Control (CNC) based 4-axis conductive ink dispenser system for developing low profile "active" interventional devices for cardiovascular procedures under MRI. The proposed 4 axis CNC controlled dispenser system allows to form three dimensional receiver antenna configurations automatically onto non-planar catheter shaft surfaces. The developed system decreases the process time and increases the repeatability significantly compared to alternative lithography based techniques also used for low profile active device development. The validation and calibration test results showed that the motion control system works within tolerance of 3.1μm and the dispenser unit works with more than %90 accuracy during several trials. As a part of this thesis study, a resonator marker on a 6 Fr catheter shaft was designed and formed based on former Electromagnetic (EM) simulation results. The resonator marker is basically an LC tank circuit incorporating a solenoid coil and a capacitor. It is used to visualize the distal tip of a 6Fr catheter under 1.5T MR systems. The impedance and resonant frequency of resonant marker were measured with a vector network analyzer and necessary modifications were made via copper electroplating until the resonant marker is tuned to 63.66 MHz. The visibility and RF induced heating tests were performed successfully for prototype marker device under MRI.

ÖZET

GİRİŞİMSEL MANYETİK REZONANS GÖRÜNTÜLEME CİHAZLARININ ÜRETİMİ İÇİN BİLGİSAYAR KONTROLLÜ ÜRETİM SİSTEMİNİN GELİŞTİRİLMESİ

İyonlaşan radyasyondan bağımsız çalışma prensibi ve üstün yumuşak doku görüntüleme yeteneği ile Manyetik Rezonans Görüntüleme (MRG) girişimsel kalp ve damar operasyonları için X-Ray floroskopi karşısında oldukça güçlü bir aday haline gelmektedir. Ancak, MRG alanında halen klinik seviyede güvenli ve görüntülenebilir cihazlara ihtiyaç duyulmaktadır. Bu tez kapsamında, MRG ile girişimsel kalp ve damar sistemi operasyonları gerçekleştirmek için kullanılan düşük profile sahip aktif kateter cihazlarının üretiminde kullanılacak bilgisayar kontrollü bir üretim sisteminin tasarımı ve geliştirilmesi amaçlanmıştır. Bu amaç doğrultusun-da, bilgisayar kontrollü özel bir pompa ünitesi tasarlanarak tasarlanan karmaşık, üç boyutlu yapıların direkt olarak doğrusal olmayan yüzeyler üzerine oluşturulmasına imkân verilmiştir. Geliştirilen sistemin düşük profile sahip aktif cihaz geliştirilmesinde kullanılan litografi bazlı diğer üretim metotlarına göre üretim zamanını kayda değer şekilde düşürdüğü, tekrarlanabilirliği ise aynı şekilde arttırdığı görülmüştür. Yapılan testler ve ölçümleme sonucunda hareket kontrol sisteminin 3.1μm hassasiyet, dispanser ünitesinin de %90'ın üzerinde doğruluk ile çalıştıkları kanıtlanmıştır. Çalışmalar kapsamında, önceden elde edilen benzetim sonuçları dikkate alınarak, 6Fr kateter şaftı için bir rezonans işaret cihazı tasarımı ve uygulaması yapılmıştır. Tasarlanan işaret cihazı basit olarak bir LC tank devresi olup bir sarmal bobin ve bir kondansatörden oluşmakta ve 6Fr kateterin uç kısmının 1.5T MR sistemleri ile görüntülenmesi için kullanılmaktadır. Oluşturulan bu yapının direnç ve indüktans ölçümleri bir ağ çözümleyici cihazı ile alınarak gerekli iyileştirmeler bakır elektro-kaplama yöntemi ile yapılmış ve cihaz frekansı 63.66 MHz'e ayarlanmıştır. Üretilen bu cihaz MRG altında görüntüleme ve güvenlik testlerine tabi tutularak, testler başarı ile sonuçlandırılmıştır.

TABLE OF CONTENTS

LIST OF FIGURES

LIST OF TABLES

LIST OF SYMBOLS

A	Area of plates of capacitor
B	Magnetic Flux Density
C_{coil}	Self capacitance of inductor
C_{Int}	Intermediary capacitor
$C_{Overlap}$	Overlap capacitor
C_{Ring}	Ring capacitor
d	Distance between two plates of capacitor
dB	Decibel, logarithmic unit
$D_{Cyliner}$	Diameter of core cylinder of inductor
F	Gauge
f_c	Center frequency
fF	Femto-farads, capacitor unit
Fr	French, catheter scale
GHz	Giga-hertz, frequency unit
H	Magnetic field
I	Current
L	Inductance
L_{Inner}	Inner tilted helix inductor
L_{Outer}	Outer tilted helix inductor
MHz	Mega-hertz, frequency unit
mm	Milli-meters, metric unit
mm^2	Area in metric system
N	Number of coils turns
nH	Nano-henries, inductor unit
pF	Pico-farads, capacitor unit
$Port_1$	Excitation port 1
$Port_2$	Excitation port 2
R	Resistance

R_{Coil}	Self resistance of inductor
R_{mean}	Mean radius for curvature of capacitor pads
$t_{Insulator}$	Insulator thickness
t_{wire}	Wire thickness
μm	Micro-meters, metric unit
ϕ	Magnetic flux
ε_0	Permittivity of vacuum
ε_r	Relative permittivity
Δf	Half-frequency bandwidth
Ω	Ohm
μ_0	Permeability of free space

LIST OF ABBREVIATIONS

2D	Two-dimensional
3D	Three-dimensional
AC	Alternative Current
CMR	Cardiovascular Magnetic Resonance
CO_2	Carbon Dioxide
DC	Direct Current
FOV	Field Of View
FISP	Fast Imaging with Steady State Precision
GRE	Gradient Echo
IMRI	Interventıonal Magnetic Resonance Imaging
HFSS	High Frequency Structure Simulator
MEMS	Micro Electro Mechanical Systems
MF	Magnetic Field
MR	Magnetic Resonance
MRI	Magnetic Resonance Imaging
NMR	Nuclear Magnetic Resonance
RF	Radio Frequency
SSFP	Steady State Free Precession

1. INTRODUCTION

The current treatment option for congenital cardiac diseases for pediatric patients is cardiac surgery that has high mortality and morbidity rates. The interventional procedures under conventional fluoroscopy are not feasible due to the late cancer risk of the ionizing radiation. At this point Magnetic Resonance Imaging (MRI) becomes a promising alternative with its ionizing radiation free imaging mechanism.

Children with congenital heart diseases generally require multiple catheterizations in order to evaluate their physiological parameters and for treatment purposes that might help to avoid or delay open-heart surgery. When these catheterizations are conducted under X-Ray fluoroscopy, each operation is an offset by the risk for mechanical complications and possible cumulative long term consequences from X-Ray exposure. Children are especially susceptible to radiation injury, and pediatric interventions often are protracted, contributing further to the risk of chromosomal damage and malignancy [10, 20].

The use of MRI technique as an imaging modality in interventional pediatric congenital cardiac diseases treatment is a recent concept. Therefore, the requirement for advance and convenient tools are valid, and several research studies are being carried out to improve the existing devices for imaging. Different structures such as micro solenoids or saddle coils have been studied as tracking devices for similar applications [30, 31]. Although there are multiple fabrication methods for developing MRI compatible devices, none of them completely meets the low profile and MR safety requirements.

This thesis study focuses on a novel computer controlled microstructure fabrication platform that uses conductive ink to form micro-patterns (especially micro-coils and other resonator components) over interventional catheter shafts, and aims to indicate its advantages and feasibility for interventional MRI (iMRI) device production, especially proper catheter devices for MRI of interventional congenital cardiac diseases.

2. BACKGROUND

Imaging of human body and internal organs with accurate and non-invasive methods has a great importance for medical diagnosis, treatment and follow-up. The principles of Nuclear Magnetic Resonance were implemented to be used for body imaging in early 1970's. In 1972, Paul Laterbur described how the addition of the gradient magnets to the static magnetic field made it possible to form two-dimensional images [1]. The idea was detecting the sources of gradients by analyzing the characteristics of the emitted radio waves. With this method, it became possible to construct two-dimensional images of structures that could not be visualized with other methods so far. In 1974, Peter Mansfield introduced a new method for the first three-dimensional imaging application. Mansfield developed the utilization of gradients in the magnetic field, and explained how the signals could be analyzed mathematically, which made it possible to develop a useful imaging technique [2]. Thus, Magnetic Resonance Imaging (MRI) was introduced.

Since the introduction of MRI, as a result of ongoing research studies, MRI has been transformed into a suitable tool for physiological imaging and medical treatment. Beside all the advantages that MRI brought to medical studies, the interventional imaging with MRI in congenital cardiac diseases of pediatric patients is stated out as one of the most merging fields [3]-[6]. Fluoroscopy is one of the essential imaging techniques that is used for the interventions in congenital cardiac diseases. However, the existence of ionizing radiation causes high cancer risk for young pediatric patients [7]. At this point, MRI is a promising alternative to fluoroscopy with its multi plane imaging ability without ionizing radiation risk.

The custom design interventional devices are needed to use MRI as an imaging tool for interventional congenital cardiac interventions. One of the most essential intravascular devices for cardiac interventional procedures is a guiding catheter. The distal tip of a guiding catheter should be visible during interventional procedure under

MRI to perform a safe procedure.

2.1 Catheterization and Imaging in Congenital Cardiac Diseases

The human heart completes its development between eighth and tenth weeks after conception and any congenital abnormalities are already occurred [8]. Numerous factors, including genetic and environmental ones, such as parasites, viruses, exposure to certain medications, metabolic disorders (like uncontrolled diabetes), excessive alcohol consumption and drugs can cause the malformation of the hearth in this period [9].

Forms of congenital heart diseases include ventricular septal defects and atrial septal defects that infant have an opening in the atrioventricular septum, pulmonic and aortic stenosis that the pulmonic or aortic valves are narrower than normal, coarctation (narrowing) of the aorta that the aorta is pinched or narrowed after it leaves the heart, and holes in the inner, separating walls of the heart that allow blood to leak or flow directly from one chamber or artery into another rather than flowing in the proper sequence through the valves [8,9]. In the past, all these congenital defects were treated through surgical operations by physicians. However, interventional approaches for adults have been preferred against surgical procedures recently due to the reduction of operation time, patient discomfort, hospitalization time, and procedure related risks [20].

The interventional procedures are performed by inserting a small diameter intravascular catheter (a small diameter flexible tube) over a guidewire into a vein or an artery and then steering it to the target cardiac chambers and/or blood vessels with the guidance of a medical imaging system (i.e. fluoroscopy, MRI, ultrasound etc.) that shows the position of the catheter relative to the background anatomy during the procedure. However, each interventional imaging modality has its own advantages and disadvantages in terms of dedicated device design, visualization of both device and anatomy at the same time and potential side effects.

2.1.1 Interventional Imaging with Fluoroscopy

Fluoroscopy is an imaging technique that exploits ionizing radiation to generate real-time images of the interior of an object, of human body at this point. During the procedure, a radiopaque contrast agent - X-Ray dye - (barium solution) is injected through the patient's vessel while the body is under frequent X-ray exposures in order to enhance the visibility and tracking of intravascular devices.

Despite the fact that X-Ray fluoroscopy is widely used as an imaging technique for the minimally invasive procedures, it has a drawback as poor soft tissue contrast and requires assumptions on device position and orientation based on anatomic landmarks and physician's experiences which may be inaccurate. X-ray exposes patient and operator to ionizing radiation that increases with procedure complexity, and significant career musculoskeletal injury to operators forced to wear protective lead aprons. X-ray fluoroscopy simply provides luminographic data without insight into the vessel wall structure and underlying plaque morphology. These data, however, are believed to be crucial for determining the origin of intimal proliferation and thus for the outcome of vascular interventions [10-13].

Moreover, X-ray exposures used for fluoroscopy consist of ionizing radiation that has enough energy to potentially cause DNA damage and may increase a person's lifetime risk of developing cancer. Based on the researches, it is known that even though the exposure to the radiation for a short period of time may increase the potential of having cancer in following life time [14]. Although radiation exposure for a single procedure might be low, since the pediatric patients need further examinations later on to evaluate their conditions, the cumulative dose of radiation they are exposed can cause higher risks.

Most importantly, children are considerably more sensitive to the carcinogenic effects of ionizing radiation than adults, and children have a longer life expectancy resulting in a larger window of opportunity for expressing radiation damage [7]. In addition, fluoroscopy can result in relatively high radiation doses, especially for interventional procedures which require fluoroscopy be administered for a long period of time. A study showed that pediatric cardiac catheterization can induce, both acutely and in the long term, increased chromosomal DNA damage in circulating lymphocytes, which represents an intermediate endpoint of cancer. Chromosomal damage was evident in the peripheral blood of children exposed to catheterization-related radiation. [15].

2.1.2 Interventional Imaging with MRI

Over the last decade, significant developments in magnetic resonance imaging technology, its superior soft tissue contrast against fluoroscopy and potential for complete multi planar soft tissue imaging and immediate functional assessment during cardiac interventions make MRI an extremely promising candidate to replace fluoroscopy. Image-guided catheter intervention on real-time imaging [3]-[7] and patient-handling [16] capabilities have been demonstrated. Nevertheless, clinical-grade interventional catheter devices for use during MRI, such as catheters and guidewires, remain the most significant obstacle to wider clinical translation because of MR compatible material problems and RF safety concerns. Current non-clinical implementations tend to offer reduced visibility under MR or excessive size which is not convenient for pediatric interventions and reduced mechanical performance [17].

Till now, there is no known harm of MRI [18] when used within well-defined technical constraints and precautions [19]. MRI provides superior soft tissue contrast for therapeutic use in cardiovascular procedures as well as it is eliminating the ionizing radiation exposure on both patient and operator [20]. MRI also provides multi slice imaging and allows physiological measurements such as temperature, perfusion, blood flow and motion. The feasibility of endovascular interventional procedures such as renal artery stenosis treatment [21], abdominal aortic aneurysm treatment [22] recanalization of carotid chronic total occlusion [23], atrial septal puncture [24] and trans-catheter aortic valve implantation [25] and electrophysiology mapping for atrial fibrillation treatment [26,28] have been successfully tested on animal models under MRI

2.2 Catheter Devices for Interventional MRI

X-Ray fluoroscopy is based on a technology that uses ionizing radiation to generate images, which increases lifelong cancer development risk and has a possibility to cause DNA damage. Also, due to its poor soft tissue contrast, it is not easy to observe cardiovascular tissue and blood leakage well during the operation which is crucial for cardiovascular procedure quality. However, since to create contrast under X-Ray is relatively easier and to fabricate suitable interventional devices for X-Ray fluoroscopy is not a complex task, X-Ray fluoroscopy has been the most common interventional imaging technique so far. On the other hand, with its ionizing radiation free mechanism, superior soft tissue contrast and its growing abilities thanks to developing technology, MRI is being a strong interventional imaging alternative. However due to safety and compatibility problems, suitable interventional devices for MRI are still needed. When the positive and negative contributions of imaging techniques are taken into account, MRI excels as the most convenient technique for imaging of pediatric cardiovascular interventions thanks to its ionizing radiation free working principle. However, MRI has been used for diagnostic purpose in clinical settings so far due to lack of safe and conspicuous interventional devices. Image-guided catheter intervention using MR remains tantalizing. Cardiovascular catheter devices used under X-ray guidance are visible based on their simple attenuation of incident X-ray photons, regardless of configuration or orientation. Comparable devices for operation under MR are more complex. They must be safe for use in the high magnetic field and must not distort the homogenous main (B_0) magnetic field, which in turn distorts imaging of surrounding anatomy. They must preserve the mechanical properties expected by the interventional operator accustomed to X-ray operation. Finally, they must be conspicuous, from the tip throughout the length inserted in the body, for safe procedure conduct during especially complicated procedures [29]. Engineering safe and conspicuous MRI catheters are especially challenging because of the combination of electrical and mechanical requirements and profile constraints. Interventional cardiovascular devices in MRI typically classified by the visualization techniques called as passive, semi-active (inductively coupled) and active.

2.2.1 Passive Devices

Passive catheters are attractive in their simplicity, but suffer from low contrast-to-noise ratios and non-specificity of image appearance. Passive devices are visible because of their intrinsic material properties during cardiac magnetic resonance imaging (CMRI). Material magnetic susceptibility, or how it responds to a magnetic field, can cause inhomogeneity in the main magnetic field that results in signal losses (negative contrast or dark spots) on images. Positive contrast (bright spots) can be generated by the use of paramagnetic T1 shortening contrast agents [20]. The ferromagnetic [30], paramagnetic [31] or other approaches include filling catheter balloons with CO2 (See Fig. 2.1) [32, 39] or more novel contrast agent materials such as 19F (Fluorine) [33] are used to improve device visibility. Off-resonance imaging techniques [34, 35] improve the specificity of the device-related signal but usually sacrifice visibility of surrounding anatomy. Recently, nonmetallic conspicuous guidewires have been developed that consist of small metal (susceptibility) markers, mimic the mechanical properties of metallic X-ray guidewires [36, 37].

Passive devices avoid many of the radiofrequency (RF) safety concerns and often are constructed easily. It is possible that the passive design preserve all desired mechanical properties while RF heating is not greater than 1oC [38]. However, they remain difficult to discern from background tissue in vivo, especially within curved vascular structures [20]. Beside that the appearance of the susceptibility artifact is influenced by deflection and by orientation. For example, when the tip is deflected perpendicular to the main magnetic field, the artifact is large and blurry and may difficult for the operator to visualize the exact location of the catheter tip [38].

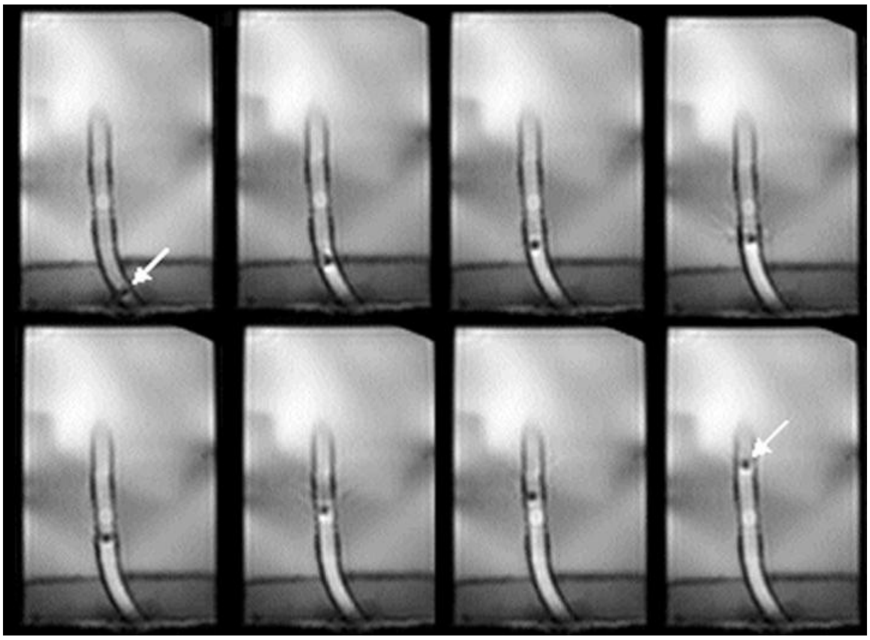

Figure 2.1 A series of Cartesian images (128x128) showing the CO2 filled balloon catheter (arrow) being manipulated in the flow phantom [39].

2.2.2 Inductively Coupled (Semi Active) Devices

Semi active devices consist of basic circuit elements such as capacitor and inductor to form inductively coupled resonant markers [21]. Wireless inductive coupled devices (i.e. catheters) act as local RF signal amplifier [14] whose signal could be coupled to outside surface coils. Therefore, these resonant markers do not require long transmission lines (connecting electrical cables) to connect the receiver marker directly to the MR scanner. but may be more visible than passive devices. There are several inductively coupled marker designs such as single loop, Gianturco, helix, tilted helix and solenoid [21].

In RF transmit mode of a MRI sequence, the detuning of RF resonators (passive decoupling) helps to limit RF energy deposition in the catheter resonators and enhance the RF safety of the interventional MRI devices. [40]. However, the device visualization of inductively coupled devices is limited to the distal tip of the catheters that contains markers [41, 42]. Further optical tuning [43, 44] or signal separation [45] techniques may be required to clearly distinguish these devices from background imaging.

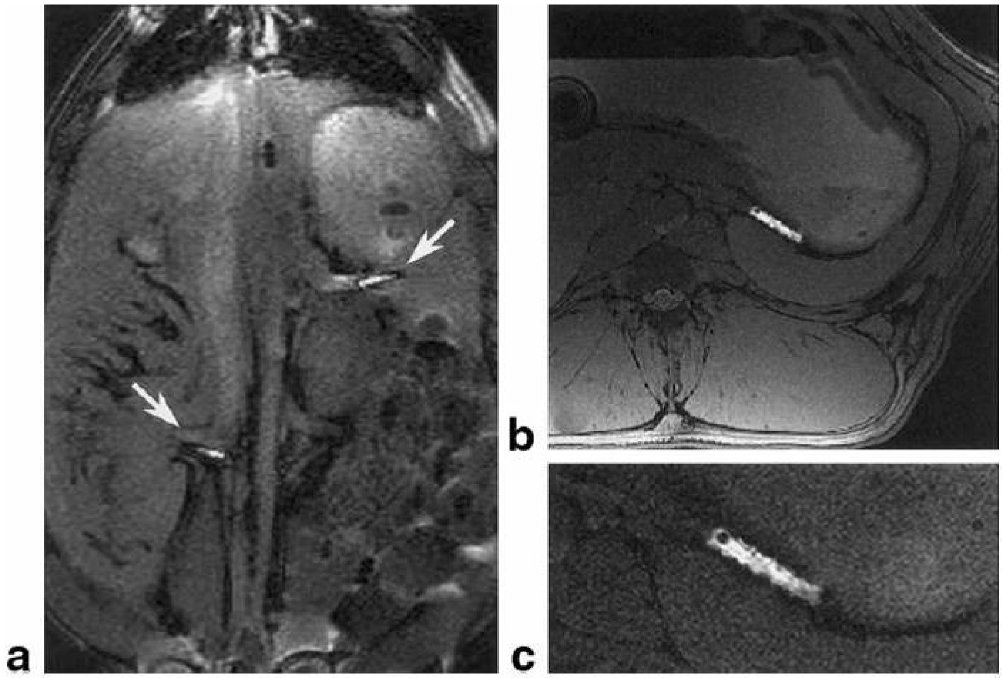

Figure 2.2 In vivo images acquired with two balloon expandable stents implanted into the right renal artery and the splenic artery of a pig. (a) The large FOV True FISP localizer image shows both implanted stents with high signal (arrows). (b) Image acquired during one breath-hold with a True FISP sequence. (c) Further reduction of the FOV to 140*140 mm, maintaining all other imaging parameters enabled full assessment of the stent lumen [14].

2.2.3 Active Devices

Active devices incorporate small coils or antennae connected to the MR scanner on separate channels through long transmission lines for device tracking or profiling purpose [46]. The device tracking requires special cardiovascular MR sequences to locate the tracking coil in 3D space with the computer-synthesized device position overlaid onto image which can be seen in Figure 2.3. Clinical-grade active guidewires and catheters are nearing clinical reality [47], but thorough performance and safety evaluation remains an important step [21].

Since long, metallic components have the potential for heating during MRI radiofrequency (RF) excitation [52], MRI compatible materials and instruments have to be used during construction of dedicated interventional MRI devices.

Clinical grade active endovascular catheters and guidewires are nearing clinical reality [48], but before moving on clinical trials, the radiofrequency (RF) induced heating risk over long conductor components of the devices needs to be addressed. The pulsed electromagnetic RF field (B1) may induce currents over long conductors in intravascular devices and cause heating especially near the device tips [49] due to resistive losses.

Several methods have been developed to limit or minimize the active device heating, including detuning the devices during radio frequency transmission (two channels), the use of RF chokes [50] or transformers [51] in transmission lines to modify the electrical length under MRI. However, although their promising improvements in terms of RF induced heating problem, none of these techniques can offer an active device design that can have clinically acceptable mechanical performance such as pushability, torqueability, flexibility, and kink resistance [52].

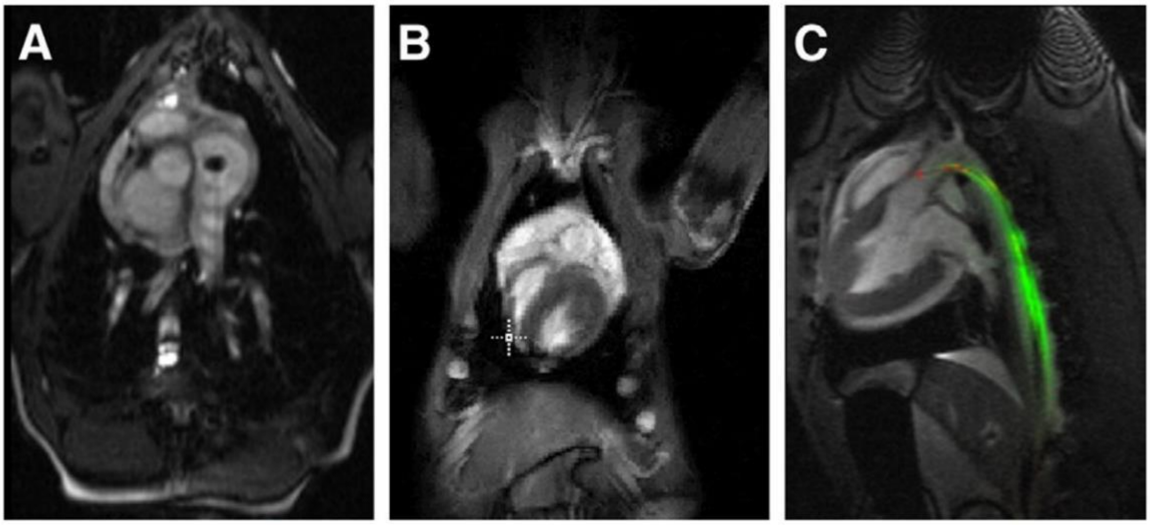

Figure 2.3 Interventional CMR Devices [5]. Three representative approaches to catheters designed to be tracked using cardiovascular magnetic resonance (CMR). (A) Passive non braided balloon catheter filled with CO2 in a right atrium. (B) Active tracking catheter in the right heart. (C) Two-channel active guidewire in the aorta approaching the left heart [21].

2.3 Catheter Device Design for Interventional MRI and Potential Manufacturing Methods

Catheter device design for interventional MRI differs from device design for X-ray fluoroscopy, regarding to MRI's ionizing radiation free mechanism. As mentioned in previous sections, X-Ray fluoroscopy works on images obtained via ionizing radiation. So that, catheter device design for X-ray fluoroscopy is based on material's contrast properties as long as the material is biocompatible and it meets mechanical requirements for the operation. On the other hand, for MRI catheter device design, other factors have to be taken into account. MRI uses strong magnetic fields and radio frequency (RF) power to generate anatomical images. Thus, MRI compatible catheter devices have to interact with at least one of these two components while preserving magnetic and electromagnetic safety. Therefore, MRI catheter devices requires RF coils so that device designs include RF receiver coil designs. Miniature RF coils have a variety of applications in MRI and magnetic resonance spectroscopy (MRS). They are increasingly used in human and animal studies. They have been used as markers to locate interventional tools like catheters, needles and endoscopes throughout the body, and also to obtain images from localized regions of tissue, aiming at micron-scale resolution [61].

Regarding MRI applications, coils are generally evaluated using remarkable parameters like B0 homogeneity [53], B1 uniformity [54], RF power efficiency [55], and SNR of their sensitive volume [56, 57]. Numerous strategies over the years have been investigated to increase sensitivity of the MRI experiment. One of the oldest strategies is to introduce successively stronger magnetic fields, as the sensitivity depends on the magnetic field. This solution, unfortunately, requires large, heavy and expensive hardware - that can limit versatility and portability- for highly sensitive MR studies. Fortunately the sensitivity also depends on the magnitude of the RF field per unit current, which has prompted parametric studies of both typical and atypical RF coil designs used in magnetic resonance. These studies have led to the development of so-called micro coils (typically, coils with outer diameters less than 2 mm) for enhancing

MR sensitivity [58].

The first micro coils were produced via hand winding solenoid coils with small gauge copper wire, though in recent years a number of alternate fabrication methods have been introduced, including lithographic production. Recently, NMR spectroscopists have borrowed from telecommunication and electronic circuit fabrication to miniaturize the RF coils and their corresponding sample volumes. For example, techniques for planar MR microcoil fabrication have been used extensively, using fabrication techniques of microelectronic and micro mechanical devices, such as lithography, electroplating, molding [59-63] and wrapping flexible circuit sheet [72] which is not convenient for small diameter features. However, these coils typically have magnetic field inhomogeneity and susceptibility effects, and are not always optimally shaped to maximize the filling factor. The results are less than optimal signal-to-noise ratio (SNR) of the MR measurement [58].

The use of solenoids over other coil geometries is the typical approach for alleviating some of these problems and achieving optimal sensitivity. Recent methods have been reported for producing three dimensional shapes such as micro solenoids or even saddle coil forms, including focused ion beam sputtering and thermal evaporation[64, 65], micro contact printing using elastomeric stamps [66, 67], three dimensional (3D) laser photolithography [68] and Inkjet printing onto non-planar substrates [71].

2.3.1 Inkjet Printing Directly onto a Flexible Surface

Inkjet printing technique has been used in the field of biology to deposit cells, and in the field of electronics to print polymers with semi-conducting properties. Recently, it is introduced as a technique for producing conductive features with desired patterns (micro coils) on planar and non-planar surfaces.

For MRI catheter device production, silver tracks are printed onto flexible polyamide (Kapton) substrate. Then this polyamide substrate with printed conductive pattern on it is used either directly for planar device designs or as wrapped around a curved surface for non-planar device designs. Silver as a material requires 962 °C to get into molten state. With today's technology, print heads which are stable at this temperature can't be produced. So, instead of using molten silver, printable inks that are stable for printing at room temperatures and includes solid silver particles are used. After printing process, silver ink is sintered at around 300 °C to get rid of non-conductive ingredients and reach a certain conductivity. By repeating this printing and sintering processes, thickness of the conductive pattern and so that the conductivity is increased. The most important advantage of this method according to lithography is that it eliminates intermediate mask stages [71].

2.3.2 3D Laser Photolithography

3D laser photolithography is used for applying photolithography technique to non-planar substrates. In this technique, initially a glass capillary or other non-planar substrate such as catheter wall, is coated with a copper seed layer by sputtering or thermal evaporation method. Coated seed layer is then electroplated with an electrophoretic photoresist. Generally a computer controlled 3D laser pointer system is used to expose laser beam and form micro-coil pattern on the photoresist. The exposed photoresist is chemically removed to obtain the copper seed layer. Since the first seed layer is around 200 nm thickness, obtained seed layer is again copper electroplated to increase thickness. Finally, with a chemical process, the remaining photoresist and coinciding seed layer are removed and only micro-coil itself is formed on the non-planar substrate. This technique is highly repeatable and versatile allowing the fabrication of complex geometries [68, 69].

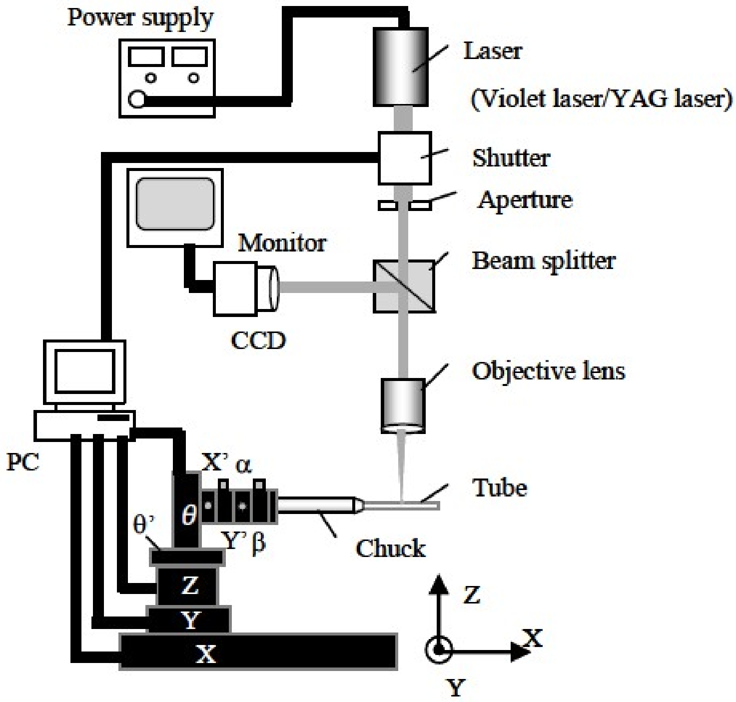

Figure 2.4 Computer controlled 3D laser pointer system. [69].

2.3.3 Optical Soft-Lithography on Non-planar Surfaces

Conventional photolithography method has some difficulties caused by rigid planar photomask contacting with the substrate at a single point, thus only small area of the features on the exposed region can be transferred onto the surface. To overcome this difficulty; soft-lithography method is introduced which transfers patterns effectively even onto very small surface irregularities via conformal contact by integrating usage of soft-photomask to the conventional process.

Optical soft-lithography is divided into two main processes as fabrication of a flexible photomask and transferring micro patterns onto small radius curved surfaces. For the first process, a PDMS thin film type photomask is fabricated. Surface of the silicon wafer is modified with alkylsilane SAM to increase the hydrophobic property (to enhance releasing). Then, desired patterns of micro metal features are formed on the substrate by photolithography. Again, each metal feature is selectively coated with alkanethiol self-assembled monolayers (SAM) for hydrophilic surface property (to create adhesive surface). PDMS mixture is spin-coated on the whole substrate. Finally, by separating PDMS film from the substrate (including the metal features), flexible photomask is obtained. To transfer the desired pattern on the curved surfaces, first, curved surface is completely coated with photoresist and then the flexible photomask, including metal features, is wrapped around the curved substrate to make conformal contact. The substrate covered with film photomask is exposed to UV light and photomask is peeled off the surface. After conventional photolithographic chemical processes, desired micro patterns are formed on the curved surface [70].

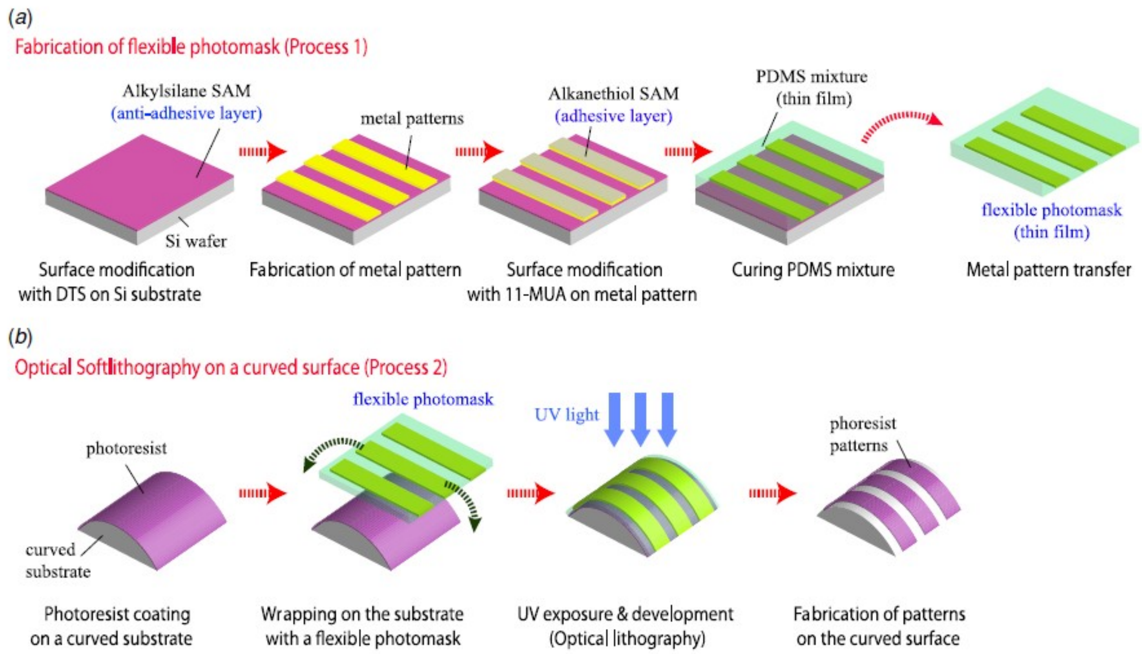

Figure 2.5 The schematic of optical soft-lithography. (a) Pattern transfer process for fabricating micro-metal patterns on the PDMS film surface. (b) Optical lithography on a curved surface using a flexible film type of a photomask [70].

2.3.4 Sputtering and Thermal Evaporation

In both sputtering and thermal evaporation methods, a high vacuum thin film deposition chamber is used to increase the mean free pathway of deposited electrons from targets as much as possible.

For sputtering, sample to be coated is cleaned with acetone and isopropyl alcohol first and then rinsed with deionized water to clean the surface. This procedure is called wet chemical treatment. Then treated sample is dried with nitrogen to prevent oxidization, masked to limit coating area and positioned in the vacuum chamber (equal distance to all metal deposition sources is preferred). The metal targets to be deposited onto sample are bombarded with electron beams to initiate electron beam evaporation in an order. First Chromium is coated as an adhesive layer which enhances adhesion between sample surface and seed layer. Then Gold or Copper is coated as a seed layer. Then the coated sample is removed from vacuum chamber and the masks are peeled. To form the desired pattern on the coated sample, sample is positioned for rotation within the focused ion beam (FIB) system. High keV Ga ions are emitted to remove Cr/Au or Cr/Cu layer in order to define desired geometry (microcoil) on the sample [64].

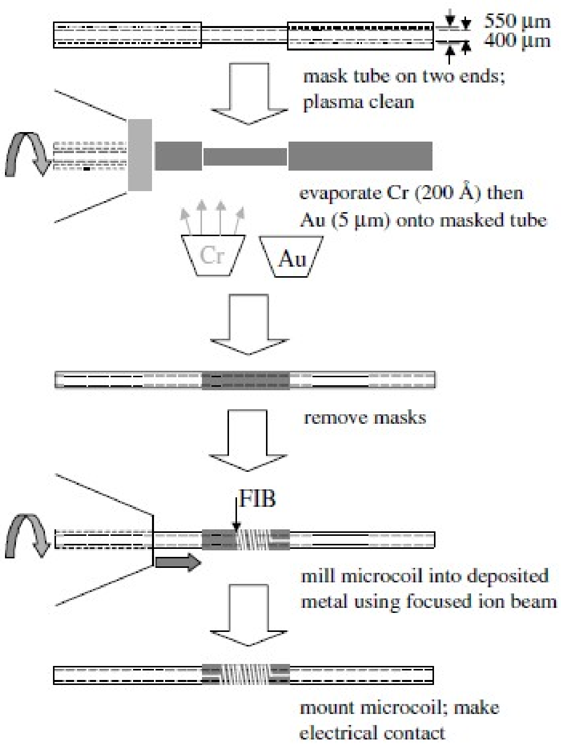

Figure 2.6 The sequence of steps used in the fabrication of the microcoil [64].

For thermal evaporation, wet treatment and nitrogen drying is applied as in sputtering. Then sample is masked with vacuum compatible materials for desired geometry and positioned in the thermal evaporation vacuum chamber. In thermal evaporation, instead of bombarding targets with electron beams, targets are heated with high electric current and with the help of high vacuum environment target electrons are deposited by evaporation and coated onto sample. Again the chromium is first coated as the adhesive layer and then the gold or copper is coated as seed layer. Deposition rate is set regarding to targeted surface tension. After coating process, sample is removed from vacuum chamber and mask is peeled. Since the underside of the mask is not exposed to the electron deposition, desired coil geometry is formed on the sample.

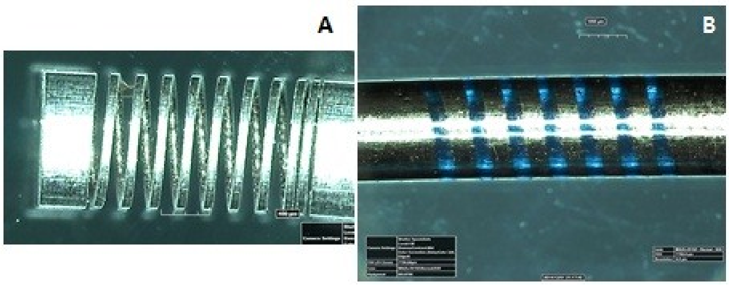

Figure 2.7 . (a) Mask used for coil geometry. (b) Cr/Au Coil geometry formed on 6Fr catheter wall by thermal evaporation.

2.3.5 Elastomeric Stamps by Usage of Micro-contact Printing

Micro-contact printing (μCP) is used for generating patterns with high spatial resolutions on planar and curved surfaces. Elastomeric stamps which are formed by means of photolithography or μCP (for high precision applications), are used to deliver ink to desired locations on the substrate. The ink is used to prevent selected areas from material removal.

First, substrate (catheter itself for interventional MRI) is coated with silver or a demanded material as seed layer. Then, an elastomeric stamp is printed as a pattern of straight or tilted lines according to desired coil geometry. Then, seed layer coated sample is rolled on the printed stamp to transfer the ink on the stamp onto cylindrical substrate. Start position of the sample on the stamp determines the aim of coil turns according to geometrical relationship. Then by means of chemical etching processes, unmasked (without ink on) seed layer portions are removed from surface. Although the obtained feature is sufficient as a coil geometry, it does not fulfill the electrical requirements. To overcome this insufficiency, formed coil pattern is finally copper or gold electroplated to increase the conductive path thickness and so that to reduce resistivity [65, 66].

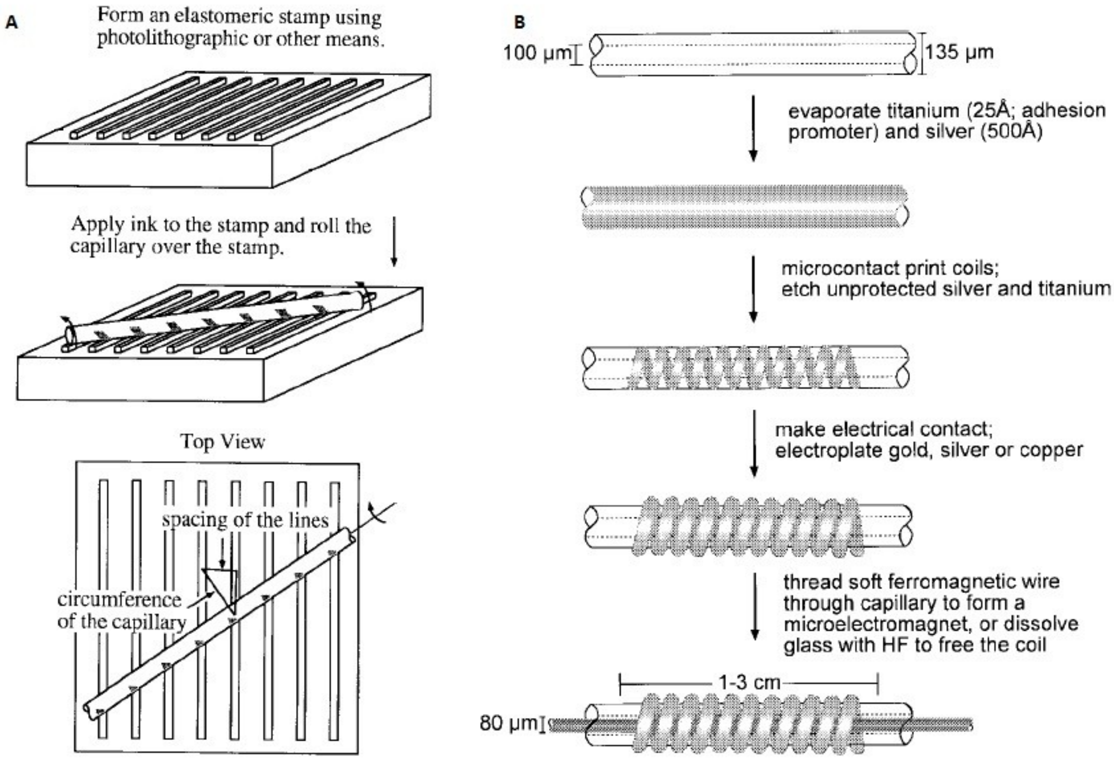

Figure 2.8 (a) Scheme for fabricating 3-D helical microcoils using microcontact printing. (b) Procedure for fabricating supported and free-standing microcoils, micro-inductors, and micro-electromagnets using micro-contact printing and electroplating [65].

3. OBJECTIVE

Active and semi-active imaging devices are needed to conduct interventional diagnostic and treatment procedures with MRI. Among the constraints mentioned in previous chapters, the main challenge for developing pediatric "active" devices is to achieve MRI visibility in low profile devices (with diameter less than 2 mm) under MRI. Passive visualization techniques cannot provide reliable device visualization in pediatric applications due to much smaller anatomical structures obscured by the susceptibility artifact of the markers. Therefore, active visualization method is more attractive. However, the active and semi-active (inductively coupled) device designs include conductive wires and analog circuit elements to form embedded RF receiver antennas. These analog components increase the overall device profile and therefore it is almost impossible to design clinical grade pediatric active devices using conventional techniques and existing commercially available circuit components.

There have been some reports of microfabrication on cylindrical substrates such as using laser ablation [74], mask lithography [75, 76], maskless lithography [73, 77, 78], wrapping flexible circuit sheet [84] or pattern transfer by elastomeric stamps. Wrapping flexible sheet is unsuitable for the tube with small diameters thanks to its difficulty of sustaining flexible circuit's structural integrity, possibility of misalignment of both end, final adhesion of circuit sheet to catheter wall and discontinuity of conductivity problems. Mask lithography is unsuitable for performing multilayer patterning since the method often causes axial and circumferential misalignment between photomask and patterns. Laser ablation and maskless lithography methods could form micro-patterns and microstructures with straightforward alignment. However, laser ablation is unsuitable for forming multilayer structures since it is difficult to control depth of ablation. Also, since lithography method uses chemical etchants to remove portions of seed layer and photo resistive material, residual chemical etchants must seriously be taken into account and final isolation must be done perfectly. Since any remaining chemical etchant particle would damage biocompatibility, lithography is not fairly suitable for developing interventional devices, although it is the major fabrication modality for electronic and electro mechanic device fabrication. Pattern transfer by elastomeric stamps is a good candidate for radially repetitive patterns on cylindrical substrates, however they cannot be used for non-repeating and complex designs and it is not suitable for non-cylindrical substrates. All these methods mentioned so far, except inkjet printing and elastomeric stamp technique, need relatively long vacuum times for seed layer coating. For multilayer device designs, this causes really long overall process times (2-3 days for some applications) and any fault at these fabrication steps can cause all procedure to fail.

The main objective of this study is to design and form a prototype of a computer controlled four axis motion control system including a smart dispenser unit,and to use conductive ink as seed layer material over planar and/or non-planar surfaces, for developing proper catheter devices for interventional procedures with MRI. Achieving this goal with expected influence requires combination of broader perspectives and methodologies. Performing fabrications with high vacuum times and with existence of non-biocompatible materials can cause time and effort loss in case of a fault during procedures. Also, special additional preparations such as masks with desired pattern geometries are needed for these fabrication methods mentioned above. This thesis study aims to introduce a reliable fabrication platform for multilayer and 3D patterning over planar and non-planar substrates, by eliminating the need for using mask layers, long procedure times including vacuum steps for seed layer generation, usage of non-biocompatible materials and usage of difficult to control ablation methods and finally to allow direct formation of desired complex patterns over substrates by reducing the number of fabrication steps so that to significantly reduce the production time.

During the thesis study, once completing the final system design and manufacturing, the accuracy of the motion control system and overall repeatability will be tested systematically. After the validation of the overall system is confirmed, straight and tilted helix coils, first and second layers of a capacitor are planned to be fabricated as the resonator parts for catheter devices and their characterizations are planned to be evaluated via vector network analyzer.

As a product of this fabrication system, a distal tip resonant marker for 6Fr iMRI catheter is planned to be designed in the simulation environment and to be prototyped with the developed fabrication platform. Finite element method (FEM) based former simulation results which were confirmed with physical measurements, are planned to be used in order to eliminate the time and effort loss for device design. Finally, all the resonant marker device measurements and MRI tests are planned to be performed.

3.1 Thesis Outline

In Chapter 1, 2 and 3 the imaging methods for interventions of congenital cardiac diseases are discussed. The advantages and disadvantages of fluoroscopy and MRI are investigated in this perspective. The ionizing radiation free mechanism of MRI brings a considerable advantage to reduce down the risk of cancer for patients. The MRI catheter device types, and their working principles are presented. At this point the objectives of this thesis study and overall project are revealed as bringing out a proper method to design and fabricate convenient tools for the interventions of congenital cardiac diseases with MRI.

In chapter 4, design and manufacturing steps of the fabrication system are described. Suitable actuators are chosen for moving parts and rotary to linear motion conversion is briefly explained. Mechanical constraints are discussed for design purposes and convenient mechanical and electrical components are chosen. Overall design of the system and dispenser unit is depicted. The computer control method, related software and the need for computer aided manufacturing software for fabrication are mentioned. Measurements of the mechanical and electronic system are carried out. Calibration of the whole system is done according to measurement results. Control software configuration is modified for calibration purposes. Once the calibration is confirmed, different coil, capacitor and stent geometries are formed on non-planar substrates. Consistency of the formed patterns are compared with the designs. Once confirming the reliability and repeatability of the fabrication system, a novel distal tip resonant marker for MRI is designed and fabricated. First, dimensional design of the circuit components is done regarding to simulation results then this design is implemented on a 6Fr catheter. Various process steps are carried out in order to meet inductance and conductivity requirements of the coil and capacitor, for 63.66 MHz. Resonance frequency of marker is tuned to 63.66 MHz within the liquid phantom. This well-tuned sample is tested under MRI for visibility and safety purposes.

In chapter 5, all mechanical measurement results are discussed. Error margins of motion system and dispenser unit were indicated. Calibrated system test results are mentioned. During fabrication steps of resonant marker, inductance and resistivity measurements are done with vector network analyzer and dimensional measurements are performed under well calibrated microscope. When the final prototype is fabricated, resonance frequency of resonant marker is measured both in the air and in a liquid phantom environment. Results of the MRI tests are shown as MRI images and heating graphics.

In chapter 6, the document is concluded with a brief summary of the achieved work within the thesis study. The precision of the system and its ability of complex geometry fabrication are discussed. Advantages brought by this new fabrication system against conventional fabrication methods are described and deficiencies of the system are pointed. As the conclusion, modifications planned for the developed system and to design and fabricate a new resonant marker which incorporates tilted helical coils, are mentioned as the future work.

4. METHODS

4.1 iMRI Device Fabrication System Design and Manufacturing

With the Computer Controlled iMRI Device Fabrication System (CCDFS), developing MRI receiver antenna patterns directly onto both planar and/or non-planar substrates via a computer controlled motion control mechanism and by using commercially available conductive ink, is aimed. Since the dispensed ink amount needs to be regulated during the operation, a computer controlled custom dispenser unit system is also planned to be designed.

The motion control system design incorporates three linear axes as X, Y and Z Cartesian coordinate axes. For planar substrates, while X and Y axes carry out the 2D movement horizontally, Z axis provides the vertical movement so that 3D movement is realized. For non-planar substrates, the sample needs to be rotated perpendicularly to the dispenser unit (mounted on Z axis). Therefore, a rotary axis is added to the system as 4th axis. Furthermore, a linearly moving mechanical pump mechanism is designed to regulate the conductive ink dose.

All these moving axes and dispenser unit are required to be computer controlled. So that a controller interface card is included to the system to control the electrical motors of each axis via an open source CNC control software.

Final fabrication system design incorporates system components as three linear motion axes, a rotary axis, a conductive ink dispenser, and a control system that controls the electrical unit.

4.1.1 Linear Motion Axis.

Linear motion task can be carried out via different components such as hydraulic, pneumatic and electrical actuators. Hydraulic actuators require a hydraulic pump unit and special hydraulic liquids that are generally not biocompatible. Also, acceleration and deceleration of these actuators are not enough for high resolution systems, instead, they are preferred for slow but high torque/force requiring systems. Pneumatic actuators also need an additional air compressor unit as power supply. Also because of the compressibility of the air, bulky and expensive control valves are required to control the pneumatic actuators with desired precision. On the other hand, electrical actuators do not need any additional bulky unit. They use a current and voltage regulator as their driver and since they are used with mechanical parts, control of the moving parts with required precision mostly depends on the accuracy of the mechanical components rather than the electrical control system. Therefore, electrical motors are used as actuators.

There are two common ways for obtaining linear motion with electrical actuators. The first is to use directly linear motors or linear actuators and the second is to use a regular rotary electrical motor and to convert this rotary motion to linear motion via mechanical interfaces. Linear motors are big in size when it is compared with the rotary motors and they are generally used in big machines because of their sizes and precisions. Also on the financial basis, they are more expensive relative to rotary motors. When all the advantages and disadvantages are taken into account, electrical rotary motors are used within linear motion axis design.

There are also several mechanisms to convert the rotary motion to linear motion. The most common ones are chain and belt mechanisms, toothed racks and pinion gears or power (trapezoidal/ball) screw mechanisms [79]. The size and precision of the moving parts have a great importance in terms of processing micro antenna patterns on low diameter catheter tube with small dimensions. For this reason, ball screw was preferred instead of trapezoidal screw because the friction force between balls and bedding is much less for ball screw and the mechanical gap between components is almost zero.

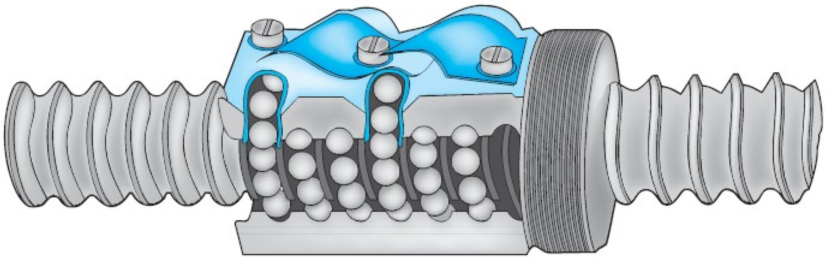

Figure 4.1 Ball-bearing screw assembly with a portion of the nut cut away to show construction [80].

4.1.1.1 Power Screw. Instead of calculating the desired power (ball) screw dimensions and trying to fabricate it, a suitable commercially available product was chosen and its dimensions and mechanical properties were tested with physical loads of the system. From THK product catalog, SBN 1605-05 single thread stainless steel ball screw was chosen. Its mean screw shaft diameter is 16 mm, outer shaft diameter with balls is 20 mm, its lead is 5 mm and friction coefficient between balls, screw shaft and nuts is 0.05 [82].

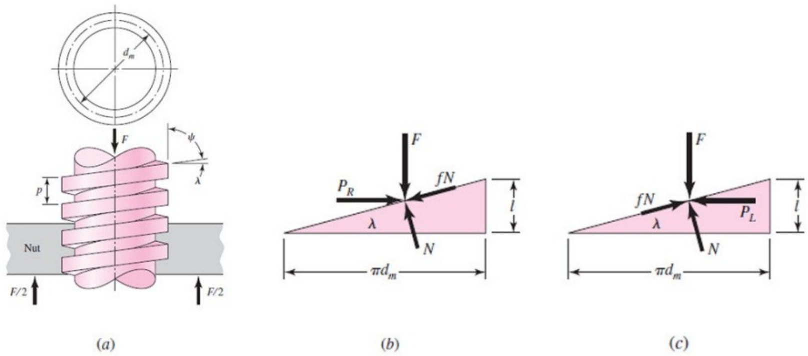

Figure 4.2 (a) Portion of a power screw with load indications (b) Force diagram, lifting the load (c) Force diagram, lowering the load [81].

The torque required for moving parts with selected power screw can be calculated by following equations.

$$T_R = \frac{Fd_m}{2}\left(\frac{l + \pi f d_m}{\pi d_m - fl}\right) + \frac{F f_c d_c}{2} \tag{4.1}$$

$$T_l = \frac{Fd_m}{2}\left(\frac{\pi f d_m - l}{\pi d_m + fl}\right) + \frac{F f_c d_c}{2} \tag{4.2}$$

Equation 4.1 is used for the torque calculation for lifting the load and Eq. 4.2 is used for torque calculation required for lowering the load. Where, F is used for load, dm stands for mean diameter and f is the friction coefficient between screw shaft, balls and nuts, dc is the outer screw shaft diameter with balls [81].

The only components exposed to thrust loads within the final fabrication system design are conductive ink dispenser and Z axis screw shafts. X and Y axes are exposed mainly to axial loads. Support bars on both sides of the screw shaft are used to eliminate the axial load exposure on X and Y axes. Same support bars are also used for Z axis and dispenser unit for both support and alignment purposes so that Z axis design and its load is taken as the main constraint and screw shaft calculations were done for Z axis.

Z axis mainly carries the dispenser unit of which weight is approximately 5 kg. Potential future modifications and safety factors were also taken into account therefore all the calculations were done for 15 kg as load of Z axis.

When all the dimensional values of THK brand power screw is placed into Eq. 4.1 and Eq. 4.2 ($f=f_c$ assumed),

$$T_R = \frac{0.15*16}{2}\left(\frac{5+\pi*0.05*16}{\pi*16-0.05*5}\right) + \frac{0.15*0.05*20}{2}$$

T_R=1.507 Nm

$$T_R = \frac{0.15*16}{2}\left(\frac{\pi*0.05*16-5}{\pi*16+0.05*5}\right) + \frac{0.15*0.05*20}{2}$$

$$T_L=0.690 \text{ Nm}$$

Required torque for lifting the load is calculated as 1.507 Nm. and required torque for lowering the load is calculated as 0.69 Nm.

Commercially available 2.2 Nm bipolar step motors (NEMA, Virginia, USA) were chosen to supply the required torque of 1.507 Nm.

4.1.1.2 Coupling and Bearing Elements. The electrical motor and the power screw need to be coupled via mechanical elements and screw shaft has to be supported with a bearing element at both end. Various coupling and bearing types are valid for this purpose [79]. For coupling purpose, most suitable coupling type was chosen as flexible, beam coupling due to its superior axial misalignment allowance, its common usage in servo control field and its reaction against impact forces [79] which would be common in our system. As the bearing element, standard rolling element ball bearings were used and commercially available SKF 634-Z ball bearing was chosen due to its inner ring diameter of 16 mm (which is the mean diameter of our power screw) and its estimated life time (with 30000 rpm under 100N axial load, life time expectancy is 30000 hours) [83]. Since only Z axis and dispenser unit mechanism are exposed mainly to thrust load and this thrust load value (50N approximately) is in the range of selected bearing element's specifications, any other thrust load bearing element was not needed and same type of bearing was used for all axes.

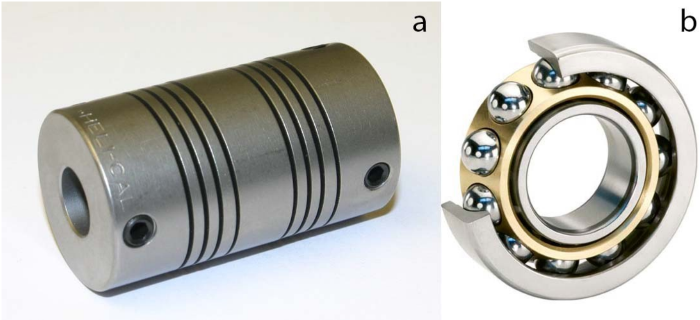

Figure 4.3 (a) Flexible beam coupling. (b) Rolling element ball bearing.

Electrical motors were chosen as step motors and they are driven with micro stepping method in this study and this method provides minimum movement of 0.003125mm (3.125 μm) for 5 mm power screw lead. Since this resolution is in the scope of our target applications, mechanical units are directly driven without using any reduction system or transfer element. Final mechanism design for converting rotary motion to linear motion is depicted in figure 4.4. A power screw with 5mm lead is connected to an electrical step motor via a flexible beam coupling element. Both the shaft of step motor and the distal end of the screw shaft are supported with a rolling element ball bearing. Motion conversion is realized via nuts of the power screw. A moving carrier is connected to nuts and it is supported by two round support bars at both side. Support bars mainly handle the alignment task for vertical axes, but for horizontal axes they also support the load and eliminate the axial loading of power screw so that prevent it from bending. Friction between moving carrier and the bars is minimized by lubrication.

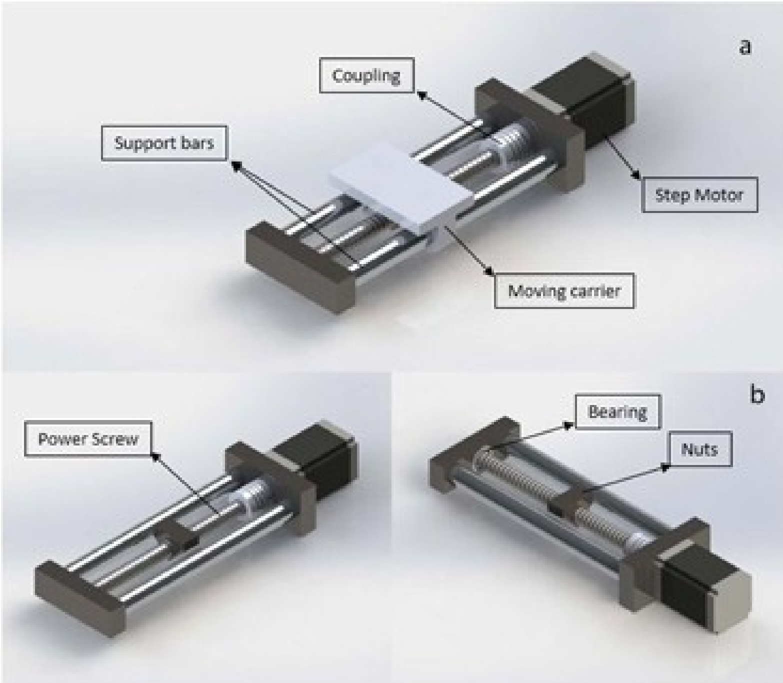

Figure 4.4 (a) Linear motion mechanism with moving carrier is mounted. (b) Components of mechanism from different perspectives.

X, Y and Z axes were designed by using the same linear motion mechanism. To provide 3D movement, Z axis is planned to be mounted on X axis and Y axis is planned to be the base moving axis, other two axes are planned to be mounted on Y axis.

Z axis' movement range was decided to be 250mm and final Z axis design is depicted in figure 4.5.

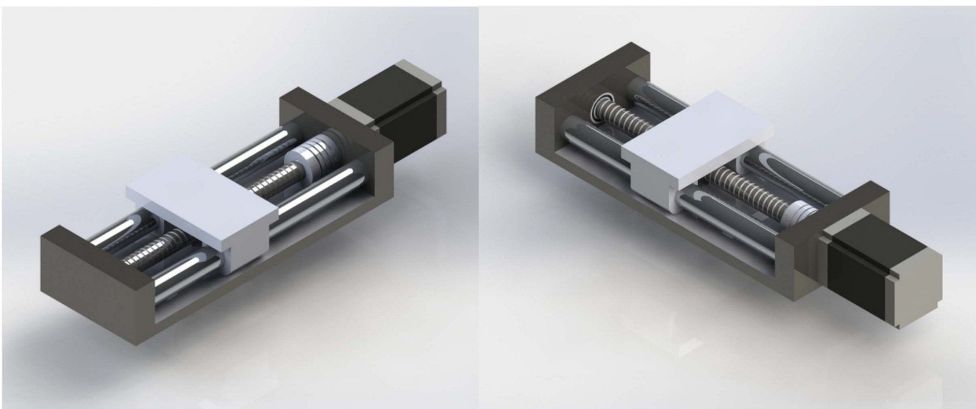

Figure 4.5 Final Z axis design with moving carrier is mounted.

With the same design, X axis' movement range was decided to be 500mm and final X axis design is depicted in figure 4.6.

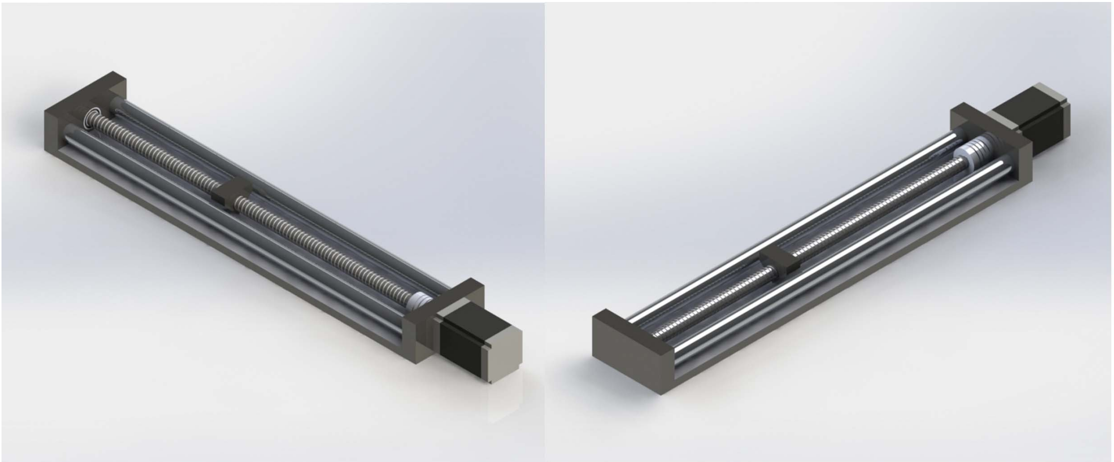

Figure 4.6 Final X axis design, without moving carrier is mounted.

Since Z axis requires to move on X axis, Z axis' base plate was mounted on X axis' moving carrier and assembly of two axes is depicted in figure 4.7.

Figure 4.7 Z axis is assembled onto X axis' moving carrier.

Finally as the base linear motion axis, Y axis' movement range was decided to be 600 mm. So that, accessible work space of the designed motion platform would be a cube with dimensions of 600mm X 500mm X 250mm. Final Y axis design with its moving carrier is mounted, is depicted in figure 4.8.

Figure 4.8 Z axis is assembled onto X axis' moving carrier.

Z axis was directly assembled to X axis' moving carrier. However, additional side plates are used mounted over Y axis' moving carrier with the dimension of 250mm (movement range of Z axis) to provide enough space for Z axis in order to use its whole movement range. Final design of three axes is depicted in figure 4.9.

Figure 4.9 All three axes are assembled with usage of side plates over Y axis.

4.1.2 Rotary Axis

Substrate itself or the print head needs to be rotated in order to process over non-planar surfaces. In final design, print head is mounted directly on the Z axis and since the samples to be processed are small catheter tubes, it was decided to rotate samples. Thanks to the advantages of micro stepping technique, rotary motion mechanism was connected directly to electrical motor. A miniature lathe chuck is used to hold and fix the samples to be printed. Final rotary axis design is depicted in figure 4.10.

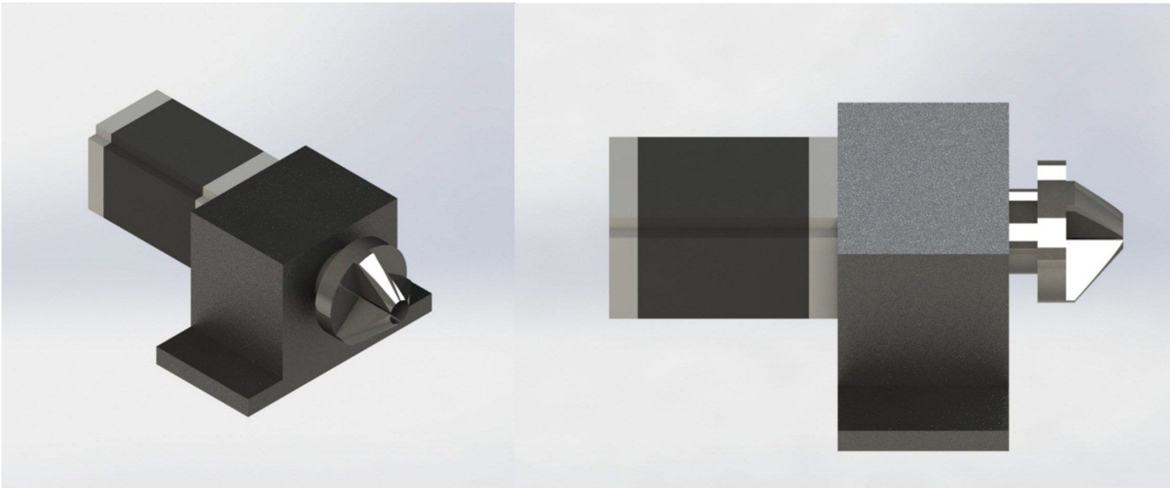

Figure 4.10 Final rotary axis design.

Rotary axis needs to be accessible by Z axis, so that it was mounted between base axis Y and Z axis. A sheet plate with grooves on it was used on machine body over Y axis to allow a mounting plate and to enable longitudinal adjustments. Final design, including all three axes and their placements over machine body is depicted in figure 4.11.

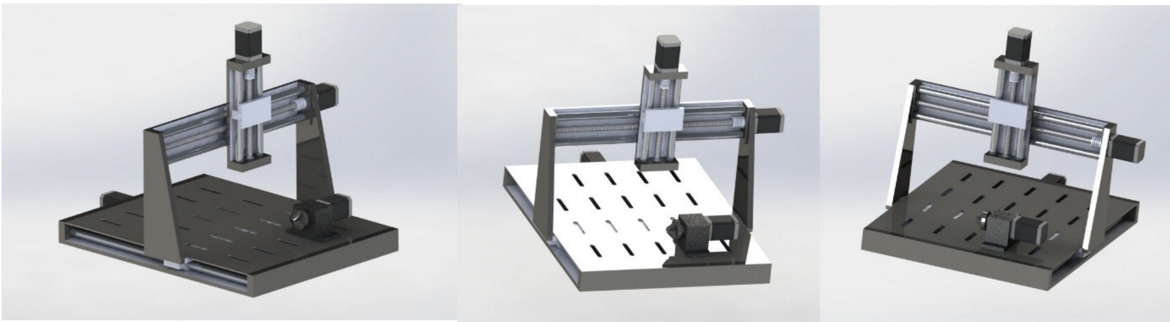

Figure 4.11 Rotary axis and sheet plate are mounted onto machine body.

4.1.3 Conductive Ink Dispenser

In the industry and literature there are several methods and equipment like pneumatic, hydraulic or mechanical dispensers and etc. for liquid dispensing. The most popular technique is to use a pneumatic pump. However, usage of this technique and equipment requires an additional air compressor. Also because of air's disadvantage of compressibility, small doses are very difficult to obtain and control [84]. In this thesis study, controlling the dispensing rate in amounts as small as possible was aimed. Since, electrical motors and motion conversation systems are used at the rest of the system, for also dispensing unit, same components were used to design a mechanical air-free dispensing unit.

A linear motion system was modified and syringe barrels with desired volumes as liquid containers were used to achieve this goal. Again, a power screw with 5mm lead was used and driven directly by an electrical motor. The minimum theoretical liquid dispensing rate was calculated as $0.15\text{x}10^{-3}$ cc per pulse with the usage of a commercially available 3cc syringe barrel (Fishman Corp. Boston, USA) with 60mm stroke and 3.1 μm linear motion resolution. A pair of springs were mounted between back plate of dispenser unit and Z axis' moving carrier to keep the clearance constant between distal tip of syringe nozzle and sample shaft. Since this distance can change due to uneven substrate surface, these springs apply a gentle force downwards to keep the nozzle always touching substrate. A linear motion mechanism similar to Z axis was modified as depicted in figure 4.12 in order to use disposable commercial syringe barrels and their pistons.

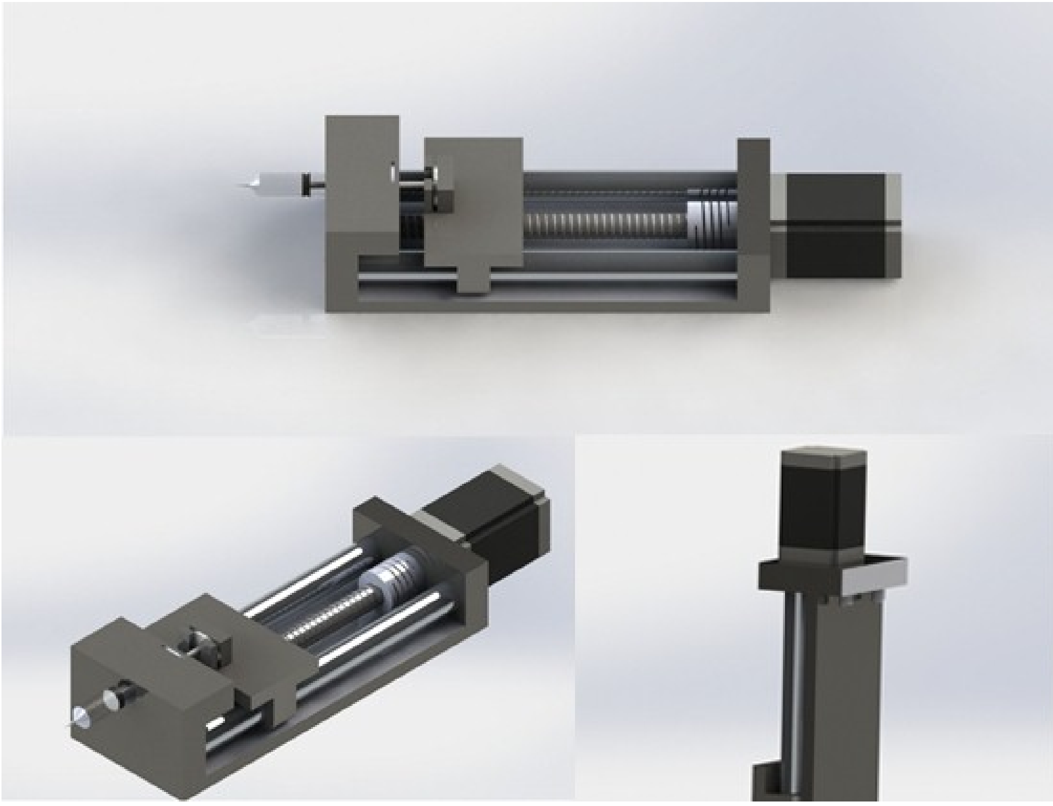

Figure 4.12 Air-free, mechanical dispensing unit mechanism, with 3cc syringe barrel.

In this design, syringe barrel is fixed at the base plate's extension. On the other hand plunger of the syringe is fixed on the moving carrier but plunged into syringe barrel. So that, by the movement of moving carrier, plunger's piston mechanism works in syringe barrel and dispensing with the controlled amount of liquid is realized.

This dispenser unit design mounted on the Z axis and used as printing head. In figure 4.13 and figure 4.14 final assembly of all mechanical parts and dispenser unit is depicted.

Figure 4.13 Complete assembly of all mechanical parts and dispenser unit on Z axis.

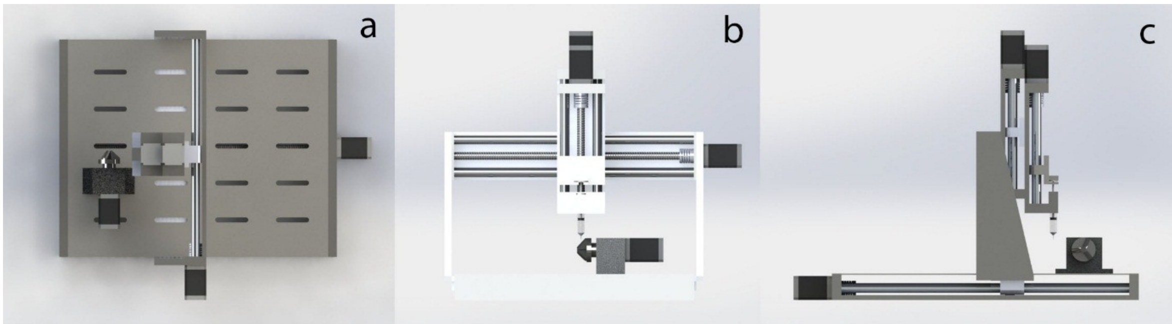

Figure 4.14 (a) Top view (b) Front view and (c) left view of the system.

Complete design of the mechanical system and the dispenser unit was produced via a local machine builder adhering to specified technical drawings. Mechanical connection elements and power screws were chosen among commercially available products as described in design section. Manufactured form of designed system and dispenser unit is shown in figure 4.15 and 4.16.

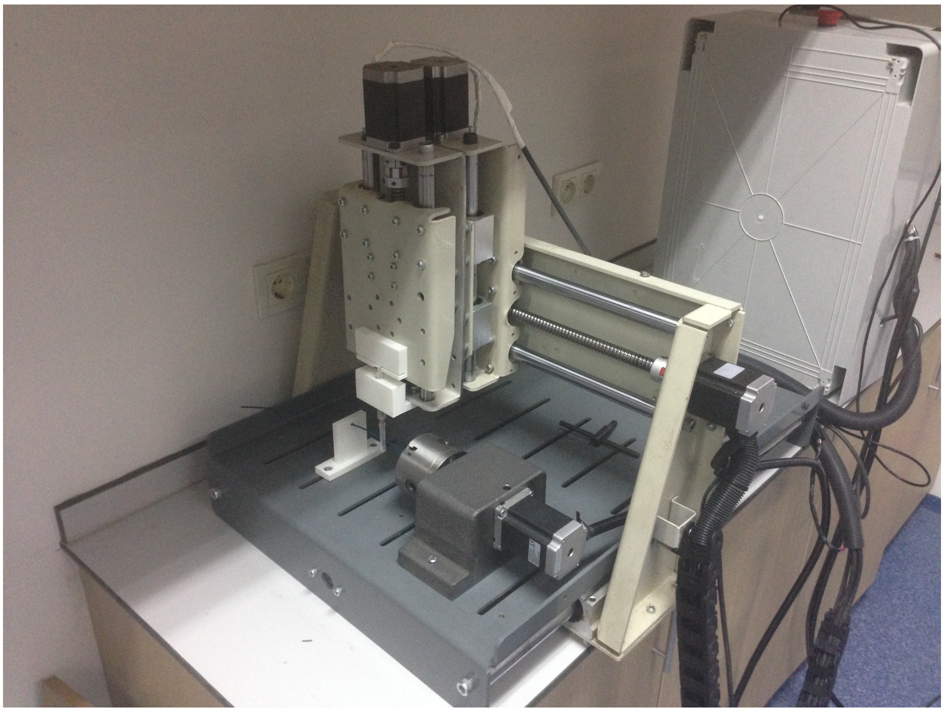

Figure 4.15 Final motion control system with mounted dispenser unit.

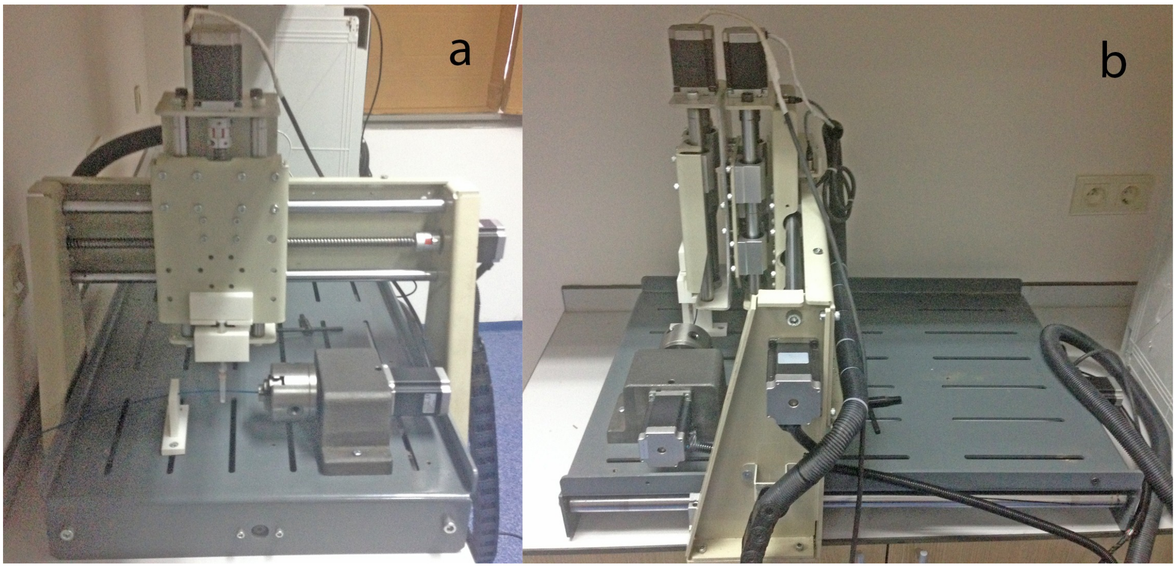

Figure 4.16 (a) Front and (b) left view of the system.

Manufactured dispenser system is also shown in figure 4.17 with a commercially available 2cc volume and 80mm stroke length medical syringe used for test purposes. Alignment of the sample within the system is depicted in figure 4.18.

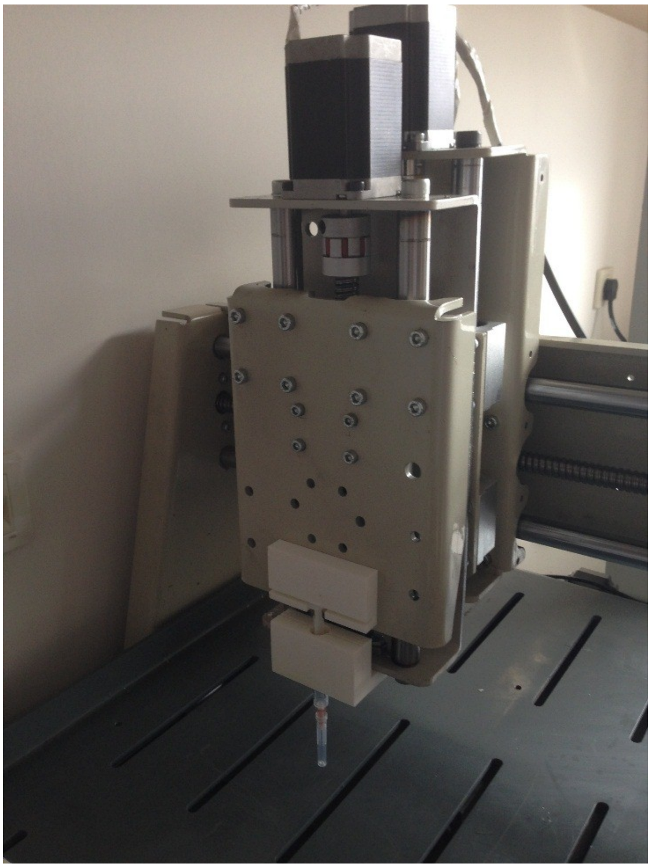

Figure 4.17 Manufactured form of smart dispenser unit.

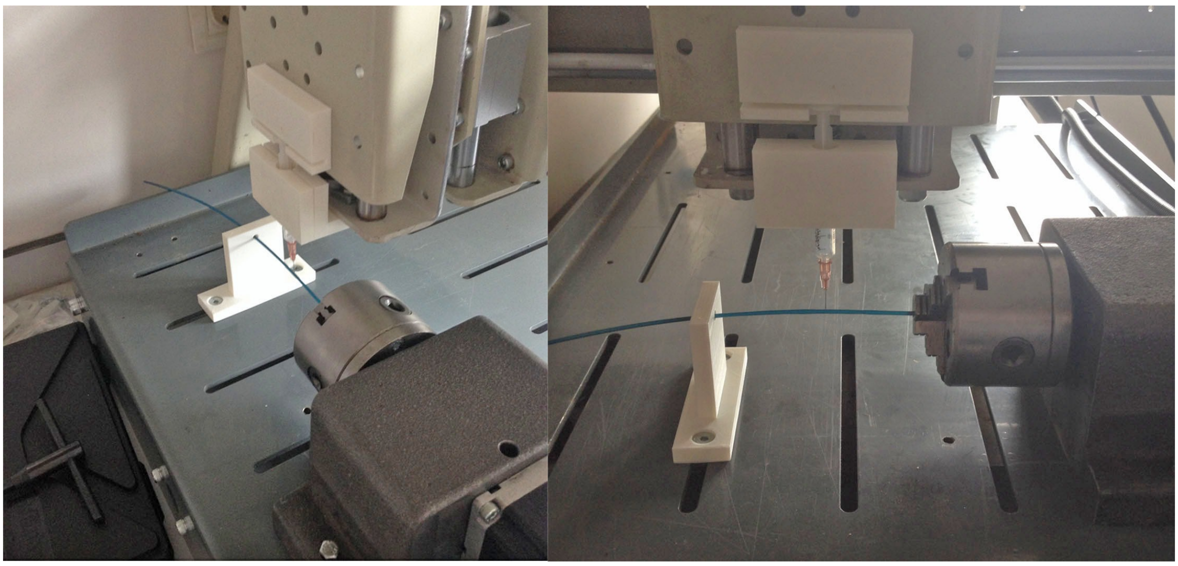

Figure 4.18 Dispenser and syringe positions in operation.

4.1.4 Control and Electrical System

It was decided to use rotary electrical motors as actuators in order to move designed mechanical system. Then, voltage and current controller units were needed as motor drivers to control these electrical motors. Since it is required to control the movement of the system via a computer, a human-machine interface software is needed. Finally, an interface circuit between control software and motor drivers is needed to allow that software to communicate with motor drivers so that to control the movement physically.

Electrical motors are mainly separated into two groups as alternative current (AC) and direct current (DC) electrical motors. AC motors are generally used in industrial applications require high power and torque capacities. On the other hand, DC motors are used in applications that require relatively lower power and torque. DC motors are also separated into several groups as brushless DC motors, stepper motors and servo motors, etc. Conventional DC motors and brushless DC motors are very suitable for the applications in which only speed control is needed and no rapid change in speed is required. However, for position control which is our concern in this thesis study, acceleration and deceleration of the motor has a great importance in order to control the position via the control of the speed in a period of time. For this purpose there are two suitable alternatives as stepper motors and servo motors. Servo motors has a great position control ability due to their optimal physical design and they are the most common motor types in motion control applications. However, they require complicated current and voltage control circuits and a reliable feedback mechanism to control their position precisely. On the other hand, stepper motor technology can be placed between servo motors and conventional DC motors for position control purposes. Stepper motors realize their rotational movements with constant angles. So that, they require less complicated voltage and current control units relative to servo motors. Also at the financial basis, servo motors and their driver units are extremely expensive according to stepper motors [85]. When all the advantages and disadvantages are considered, bipolar step motors with permanent magnets were decided to be used. Since the maximum required torque in designed system was calculated as 1.507 Nm, to stay at the safe side, a commercially available step motor with 2.2 Nm torque (Nema, Virginia, USA) is decided to be used (Figure 4.19).

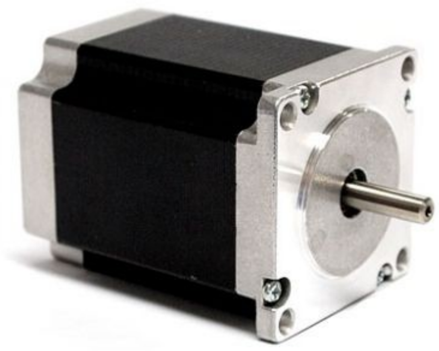

Figure 4.19 A commercially available 2.2 Nm step motor.

In a standard motion control application, motors work against loads like lifting something, machining metal blocks, winding and releasing strings or metal bars, etc. So, motor control units require a special feedback mechanism which is called encoder in order to know the actual position of the motor so that to handle motion control accurately. Via this feedback, set position of motor is changed according to error between actual and reference position of the motor. This method is called closed-loop control. However, in our application, motors work only against frictional forces between mechanical components which are negligible. So that, it was decided not to use encoders and to control motors with open-loop control.

Step motors are controlled with several control techniques as full step, half step and micro stepping. With full step control method, with each control pulse, motor rotates for its basic rotation angle. For the motors used in this study, basic rotation angle is 1.8° so that the required amount of pulses for a complete 360° turn is 200 pulses. In full step control mode, just one phase at a time or two phases at the same time can be energized depending on the control technique. Maximum torque is obtained in this mode. With half step control method, energization of windings is alternated and required number of pulses for a full turn rotation is doubled so that the resolution of rotation is increased. On the other hand, because of alternating the current on phases motor torque is decreased roughly %15 according to full step control. With micro stepping control method, both the direction and amplitude of current flow in each winding is controlled. Current is proportioned in the windings according to sine and cosine function. With this method, basic step angle of a step motor can be divided to 256 and the resolution of the motor can be increased up to 256 times [85].

In this thesis study, power screws with 5mm lead were used for linear motion and this 5mm distance is covered when the motor completes its full turn rotation. Maximum allowable error was decided as 4μm for designed system. Since chosen step motor's basic step angle is 1.8° it requires 200 pulses for a full turn with full step mode which enables minimum linear movement of 25μm. Micro stepping method is planned to be used and each step is divided into 8 sub steps to obtain desired motion resolution, so that 1600 steps in total were obtained for a full turn rotation. This method allows 3.125μm resolution which is in permissible range.

A commercially available stepper motor controller with the ability of micro stepping up to 16 sub steps (M542, Leadshine Tech, Shenzen, China) was decided to be used for all axes and dispenser unit (figure 4.20) in order to control motors with micro stepping method with 8 sub steps.

Figure 4.20 Step motor control unit.

A special programming language called G-Code programming is commonly used for motion control systems. This language uses special codes that starts with the letter of G or M and continues with numbers. With these codes, motion of the axes and status of input and output ports can be controlled. For the motion control industry, G-Code programming is considered as the master programming language and it is used in almost all computer numeric control (CNC) machines. There are also other less common and generally custom programming languages like graphical programming or pulse counting, etc. However, nowadays with the help of developed computer and software technology, a special software is used for complex manufacturing tasks within motion control systems and these software are called computer aided manufacturing (CAM) post generators. CAM post generators generates motion control programs according to a desired design that is drawn in a computer aided design (CAD) software environment and CAM software generate these codes in G-Code programming language.

In this thesis study, processing complex geometries that is very difficult to program manually and to use a CAM software to generate the required program code are also aimed. So that, it was decided to use a software that can read the G-Codes and converts them into logical signs for electronic control units. When the complexity of writing an interface software for this purpose is taken into account, it can be considered as an independent thesis study. For this reason, a commercially available, and free to use up to limited rows of code, software (MACH3, Newfangled Solutions, ME, USA) was decided to be used (Figure 4.21).

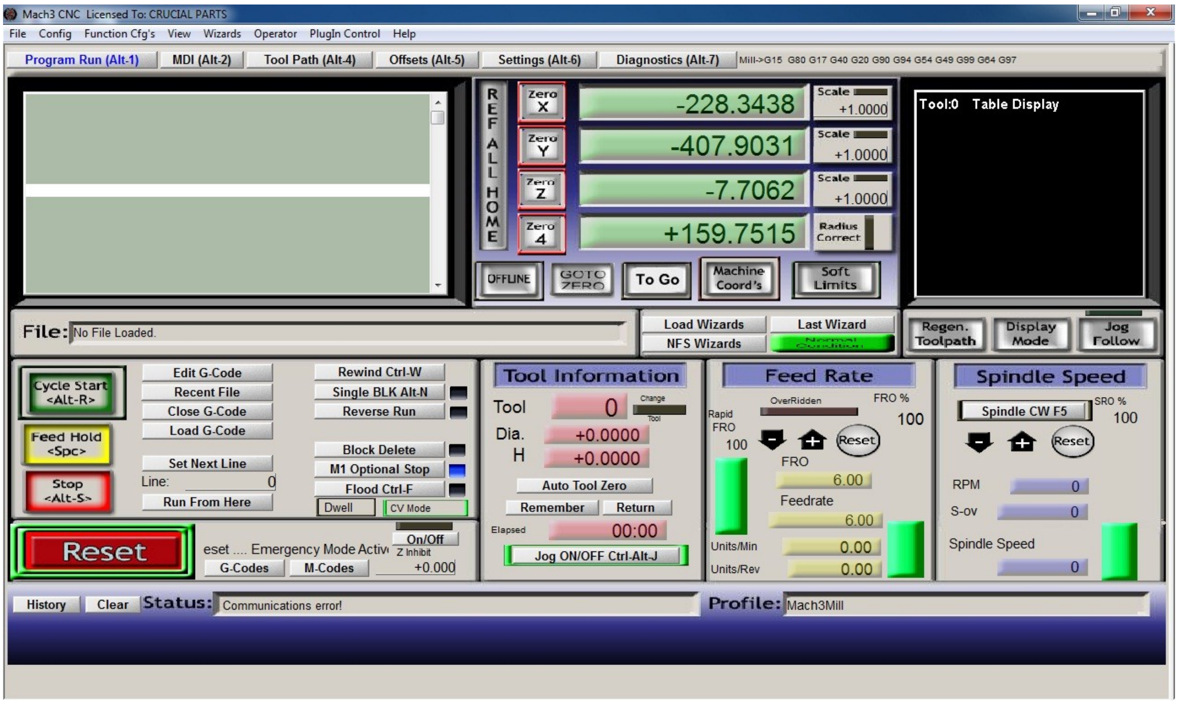

Figure 4.21 MACH3 CNC Control Software Interface.

MACH3 software normally uses parallel port of the computer to communicate with external environment thanks to ease of its control and easy design of convenient breakout boards. However, with nowadays technology and hardware configuration of the computers, parallel ports are so rare and very difficult to find on new computers. Also since parallel port's pin number is limited, controllable device number is limited when it is used. For these reasons, an interface card that communicates with computer so that with MACH3 via universal serial bus (USB) port was decided to be used. By this way, to be able to use various number of input/output signals (for emergency switch, homing and limit sensors, etc.) besides controlling motor control units, is also aimed. For all these purposes, a USB interface card with the capabilities of controlling 5 step motor drivers and 8 Input / 8 Output signals (Leadshine, Shenzen, China) was decided to be used (Figure 4.22).

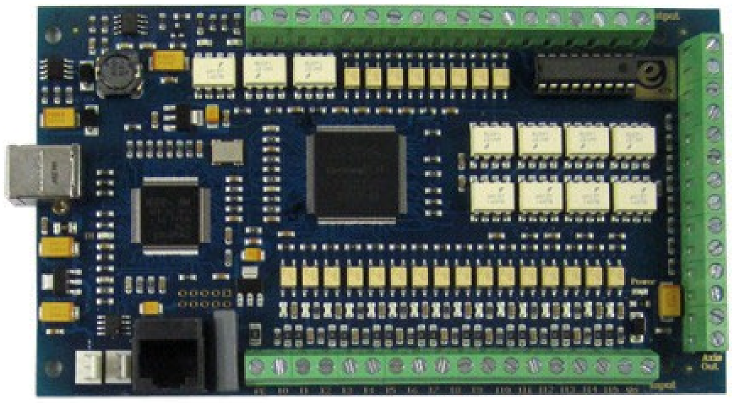

Figure 4.22 USB MACH3 Interface card with 16 bit digital I/O.

4.1.4.1 Control of Dispenser Unit. Again commercially available micro stepping step motor driver is used in order to control the stepper motor of dispenser unit. Due to the difficulty of finding a parallel port, dispenser unit is controlled via two ways. First, for the computers that have no parallel port, motor driver is connected to MACH3 interface card as 5th axis. Then by programming this 5th axis in software, pump mechanism is controlled simultaneously while other axes are moving. Second, for the computers with parallel port, motor driver of dispenser unit is connected to parallel port of the computer via a simple breakout board just to ensure parallel port's electrical safety. Then with a custom software, dispenser unit is controlled with desired parameters via parallel port (Figure 4.23).

By using this custom software, dispenser unit can be controlled either in automatic mode or in manual mode. In manual mode, pump mechanism is moved upward or downward with the specified step sizes of 0.001, 0.01 or 0.1 cc. In automatic mode, flow rate can be set to a constant value for a period of time, or the total amount to be dispensed in a period of time can be set. The viscosity of dispensed liquid is important to calculate the maximum allowable velocity of dispenser mechanism. So that, this software does not exceed the velocity limit regarding to entered viscosity even if it is set to a higher value. Finally, at the end of dispensing process, plunger is retracted

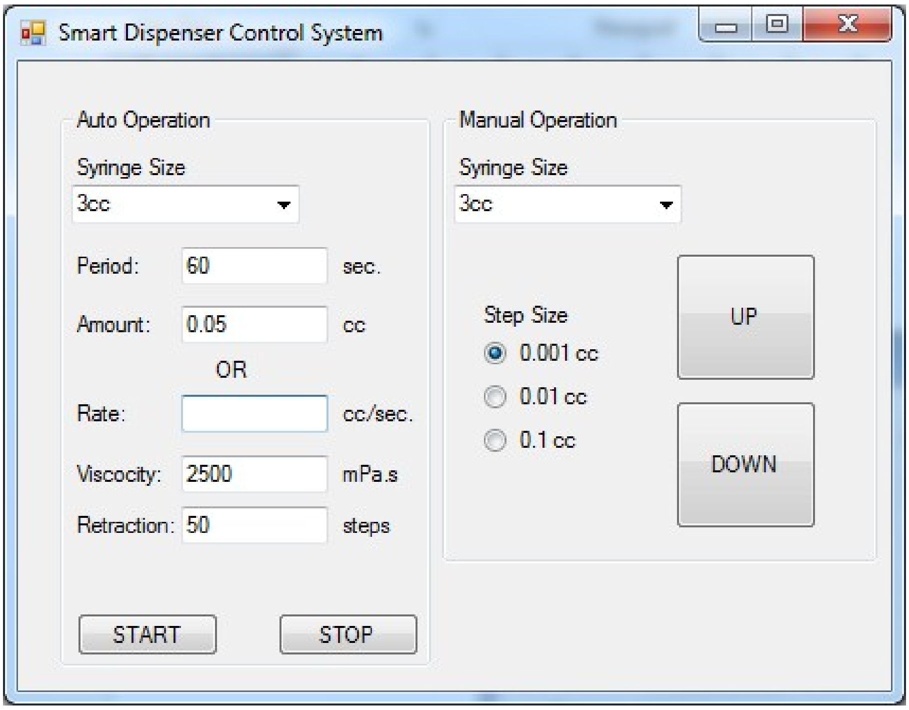

Figure 4.23 Custom Dispenser Unit Control Software Interface.

for specified steps to prevent the residual amount of liquid in the syringe nozzle from dropping.

For now, due to lack of our programming skills about USB port control, this software works with parallel port only. However, since this dispenser unit is required to perform standalone also, to communicate with this software via USB port so that with the MACH3 interface card, and to control dispenser motor driver as a separate channel is planned as a future work.

Finally, control unit of the system and electronic design includes a computer that runs the G-Code editor and dispenser controller software, then a USB interface card for the communication between computer and motor drivers, four motor drivers for four motion axes and another motor driver for dispenser unit's motor, a simple breakout board for parallel port's electrical safety and a DC power supply for electronic units. The schematic diagram of the system is depicted in figure 4.24.

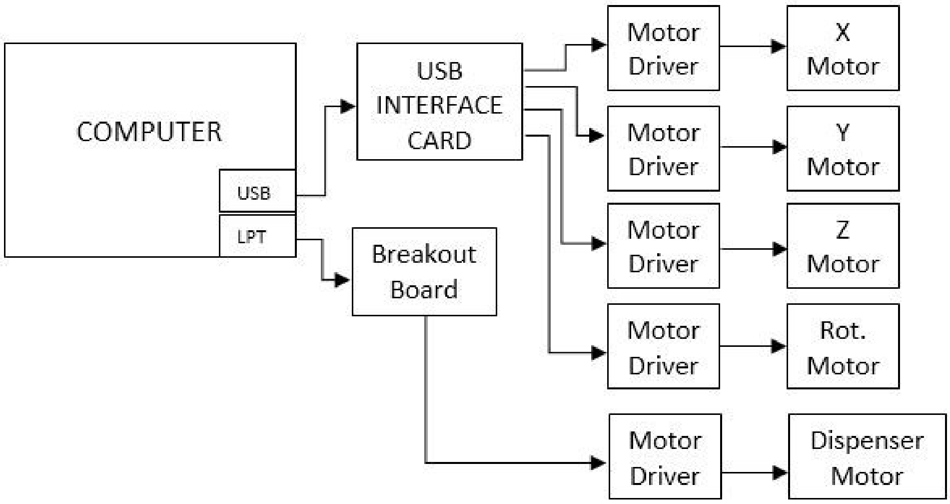

Figure 4.24 Schematic diagram of control and electronic system.

Electrical system components in an electrical cabinet are shown in figure 4.25.

Figure 4.25 Electrical cabinet of motion control system.

4.2 The System Calibration and Test

Within all the linear motion axes of designed fabrication system, power screws with 5 mm lead screw pitch were used. These power screws are driven by electrical step motors that are controlled in micro stepping mode and complete their one turn rotation with 1600 steps. This means the distance of 5 mm can be divided into 1600 steps and with one step 3.125 μm can be traversed. This minimum obtainable movement of 3.125 μm is the theoretical linear motion resolution of designed system and to obtain it physically was aimed. Same is valid for rotary axis and by dividing rotation of 360° into 1600 steps, to obtain minimum rotation of 0,225° is aimed.

Theoretically, for 1600 pulses, linear axes are planned to move 5mm and rotary axis is planned to rotate 360°. However, because of mechanical faults like gaps due to misassembled parts or faults in mechanical parts' dimensions, these values might change in manufactured form of the system and they need to be calibrated. For this purpose, at the beginning MACH3 software was configured to be 1600 pulses for 5mm traverse of linear axes and 1600 pulses for 360° rotation of rotary axis. Then these configuration was planned to be compared with physical measurements. According to physical measurements and the error margin, number of pulses for each axis is planned to be modified on MACH3 side and the fault is corrected so that the calibration is planned to be carried out.

Axes were moved for integer distance values as 1, 3, 5 and 10 millimeters. Then physical distances that are traversed by the axes were measured in order to test if the motors complete their one turn rotation with 1600 pulses. These calibration tests are done by using existing conductive ink dispenser and the tiniest syringe nozzle we have with diameter of 32G. With this setup, straight lines are drawn around catheter wall in specified intervals. By taking drawn line width into account, distance between beginnings of two lines were measured under a well calibrated microscope (HIROX KH-8700, NJ, USA). This procedure was repeated for three times for each interval value. According to measurements, so that to error, number of pulses were modified. In this chapter, calibration steps for X axis are explained and same steps are repeated for all axes.

According to measurements, mean error margin at 5mm distance is calculated as 100.625 μm for X axis after 3 trials. Pulse number of X axis required for 5 mm movement was modified to 1635 pulses to compensate this error. Same measurements and correction were done for Y and Z axes also and the modified pulse numbers are 1642 for Y axis due to 120.75 μm mean error, 1623 for Z axis because of 66.125 μm mean error and rotary axis was left with 1600 pulses.

Once the calibration is done and confirmed, there is also another measurement called backlash is needed to be performed and corrected for this kind of systems. Backlash is a clearance or a lost motion caused by gaps between mechanical parts and occurs when the axis performs reverse traverses consequently. Due to this gap between mechanical parts, when the axis tries to move to reverse direction after one direction, first, this gap is filled then the movement occurs, so that a portion of the movement is lost. For systems like this fabrication system design, this gap has to be measured and control unit has to be configured to compensate this loss while reverse traverses.

A straight line is drawn on the catheter wall in order to measure backlash of axes, then axis is moved to one direction for 5mm then axis is moved to reverse direction for 10mm in order to pass the first line. By measuring the distance between the two lines at both ends backlash was measured.

Since, backlash would be same for all amount of distances, control software was configured to compensate backlash of 145 μm for X axis, 137 μm for Y axis and 12μm for Z axis. After this configuration, same test was carried out and distance was measured. After that all the mechanical faults were compensated and the calibration of the system was confirmed, several geometries such as straight helix coil, tilted helix coil, capacitor layers and stent patterns which are the focus components for iMRI devices, were formed over catheter wall.

4.2.1 Dispenser Unit Calibration

During this thesis study, a commercially available silver based conductive ink (AG-610, Conductive Compounds, NH, USA) is used. Specified amounts of ink were dispensed by controlling the volume and since the density of the ink is known, weight of the dispensed liquid is weighted with a precision scale (Precisa XB 220-A, Dietikon, Switzerland) with the precision of 0.0001 g in order to test the accuracy of dispenser unit.

Since the dispenser unit is driven by a linear motion mechanism, at first this mechanism is needed to be calibrated. By marking the position of the moving carrier of dispenser unit, before and after moving it for 5 mm on mechanism body and by measuring the distance between two marks so that the actual movement, motion error was measured as 37.3 μm. According to this error margin, dispenser unit's required pulse number for 5mm movement was modified to 1613. After this modification, calibration of linear motion mechanism was confirmed.

Once the calibration is confirmed, dispenser unit was tested with dispensing volumes of 0.1, 0.01 and 0.001cc. During this test, first, syringe nozzle was approached to a petri dish, then specified volume was dispensed, after that the drop occurs at the tip of nozzle, nozzle was touched to petri dish and it was traversed for 20mm to transfer all the dispensed liquid to petri dish surface to prevent residual liquid from remaining at the nozzle tip because of adhesion. Then petri dishes were weighted by subtracting the tare.

Density of the silver based conductive ink is declared as 1147 g/L by the manufacturer company [86]. So that, it is expected to be weighted 0.1147g for 0.1 cc, 0.0114g for 0.01cc and 0.0011 g for 0.001cc.

Dispensed volumes were controlled by custom smart dispenser control software. Dosing tests were repeated for three times and dispensed volumes were measured.

Measurement results showed that for volumes of 0.1cc and 0.01cc, dispenser works with the accuracy more than %90, however for very small volumes such as 0.001cc, dispenser accuracy drops to 60 per cent. When this fault was investigated, it was understood that, since the ejected amount is so little, a portion of the liquid cannot be ejected from the nozzle and remains in the ejection channel. Dispensing process for 0.001cc was repeated for 20 times to obtain 0.02cc ejection to test this small amount of ejection. At the end of 20th ejection cycle, rest of the process was carried out and the weight was measured as 0.0207g which is more than %90 accurate.

Finally, it was measured that dispenser unit works with more than %90 accuracy.

4.3 A Novel Distal Tip MRI Catheter Marker Design and Fabrication

The need for conspicuous and MR safe interventional devices especially for pediatric interventions is mentioned in previous chapters.

Fabrication of such devices with conventional fabrication methods and existing rigid analog circuit components is not feasible due to MR safety and profile constraints. A novel marker device for 6 Fr catheters was designed and fabricated by using the fabrication platform which was designed and manufactured within the scope of this thesis study in order to overcome this problem. This marker device was planned to be an encapsulated resonator tank circuit and mounted to tip of any MR compatible catheter structure.

Marker device was designed to work with 1.5T MR systems of which larmour frequency is 63.8 MHz. This device incorporates a micro-coil as RF antenna and a capacitor component to resonate at the larmour frequency. Since this device is planned to be used within pediatric applications and the vessel structures of pediatric patients are narrower than adult patients, final form of the design needs to be a low profile flexible structure to be steered and traversed within the vessels. Resonator components were fabricated as flexible thin film layers over catheter wall and formed by usage of conductive ink to meet these requirements. Parylene-C was coated between two capacitor layers as dielectric material to create a capacitor component. Thickness of the conductive ink layers was increased by copper electroplating in order to overcome resistance and skin effect problems. Finally, final form of the device was coated with a parylene layer for insulation purposes to ensure both device safety and biocompatibility.

Former EM simulation results were used to eliminate time and effort loss at design step. Then simulated design results were compared with physical measurements of fabricated device with a vector network analyzer (ZVB 4, Rhode and Schwarz, Munich, Germany). When the consistency of the device was confirmed, the prototype device was tested in a phantom with MRI system for imaging and heating purposes.

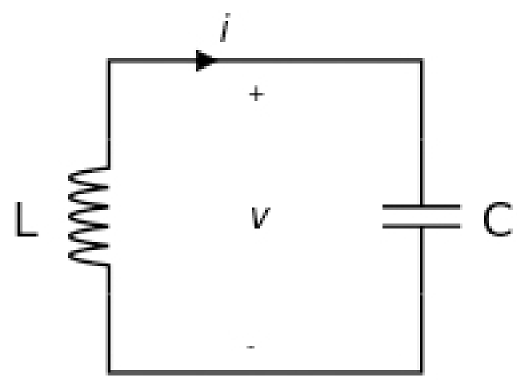

Figure 4.26 Electrical diagram of LC resonant circuit.

4.3.1 Circuit Design and Simulation

Straight and tilted helical coils are generally used as micro-coils for semi-active MRI device designs. According to Faraday's law, as helical coil creates magnetic field in space, it is also possible to create current within a coil by introducing a changing magnetic field around it.

In MRI applications the existing RF magnetic field generates current within the coil structure, as coil's magnetic field directionality matches with the direction of the RF field. Therefore, straight helical coils can provide imaging on one plane, due to their directionality which is on longitudinal axis within the scanner bore. On the other hand, tilted helical coils can provide imaging on more than one planar surface thanks to their ability to cover two directions partially at a time, however their peak efficiency is reached when the magnetic field is perpendicular to their tilting axis.

In this thesis study, straight helical coil geometry is planned to be used within marker device design.

4.3.1.1 Design and Simulation of Straight Helical Coil. Equations 4.3, 4.4 and 4.5 show the general mathematical expression of straight helixes in cartesian coordinate system. R is the radius of the curvature of the helix, h is the separation between turns, and θ is the angle in radians which defines the turn number when divided by 2π. Coil geometries used for design is generated adhering to these equations.

$$x(\theta) = rcos(\theta) \tag{4.3}$$

$$y(\theta) = rsin(\theta) \tag{4.4}$$

$$z(\theta) = h\theta \tag{4.5}$$

Several coils with different number of turns and lengths were simulated within COMSOL Multiphysics and HFSS simulation programs.

Inductance calculations of virtual coils were done by adding Single Turn Coil (STC) definition to preset physics with a boundary feed and ground port. One other study was run during simulations to calculate the resonance frequency directly without observing the plots or searching the effects of resonance. Electromagnetic wave propagation and resonant behavior were simulated to compute electromagnetic field distributions, transmissions, reflection, impedance, Q-factors, S-parameters, and power dissipation. Multiple physical effects can be coupled together and consequently affect all included physics during the simulation of an electromagnetic device or structure. For this study, eigenvalue solutions were generated to calculate the resonance frequency of device directly.

Simulated coil geometries were fabricated by hand with reasonable dimensions by using commercially available 100μm thick isolated copper wires over 3D printed plastic cores In order to confirm simulations' reliability.

The plot in Figure 4.27 includes the data points which are the results of the simulations and measurements of 5 and 10 mm diameter straight and tilted helical coils with 2 mm pitch having changing turn numbers. 24 different designs were simulated, and their inductance values were derived. It is clear that there is a linear relation in between number of turns and inductance value. This dependency were drawn by using linear interpolation approach.

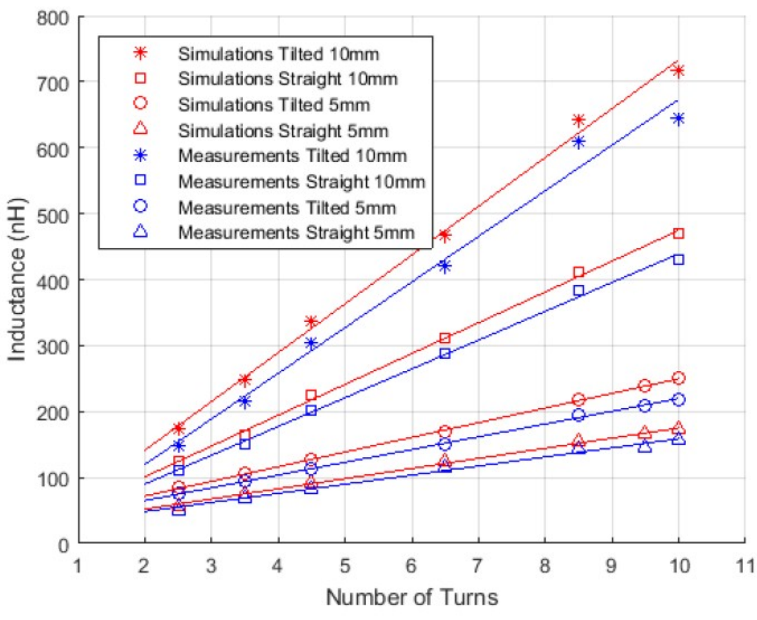

Figure 4.27 Inductance results of simulations and measurements.

Although there are many mathematical models for helical coil inductance calculations, almost all of them are custom models and use custom correction coefficients to calculate the inductance value. So that, since the simulation consistency and reliability are confirmed, simulation set-up was used to calculate required coil dimension for target inductance value. According to recent studies, an optimal inductance value is determined due to electrical length of coil, resistivity, visibility, etc. This optimal inductance value is determined as 120-130 nH [56]-[69]. When the simulation was run for a straight coil geometry with 2mm inner diameter (outer diameter of a 6Fr catheter), 5mm length and 125nH inductance, number of turns was calculated as 12.87. However, number of turns was decided to be 13 in order to use an integer value.

4.3.1.2 Capacitor Design. A capacitance is needed to be integrated to circuit in order to build a resonator. Equation 4.6 is used to calculate this value.

$$C = \frac{1}{L(2\pi f)^2} \tag{4.6}$$

f is the larmour frequency of 1.5T MR systems which is 63.66 MHz and L is determined as 125nH. By using these values capacitor value is calculated as 50 pF.

Coaxial capacitor design was used as the capacitor geometry, capacitance value of coaxial capacitor is calculated via Equation 4.7.

$$C = l\Big(\frac{2\pi\varepsilon}{\ln(\frac{b}{a})}\Big) \tag{4.7}$$

ε is the permittivity of dielectric constant which equals to $\varepsilon_0 \cdot \varepsilon_{Parylene}$. ε_0 equals to 8,854*10^{-12} and $\varepsilon_{Parylene}$ equals to 2.95. b is the radius of capacitor's second layer and a is the radius of capacitor was taken roughly 1,003mm (after parylene coating). Length of the capacitor is calculated roughly as 1mm for desired 50 pF of capacitance (when l=1 mm, c is calculated as 54pF).

After all the dimensions of circuit components are calculated, coil and capacitor were placed on the catheter wall side by side connected to each other. For connection between first and second layer of the circuit, an additional ring layer with the length of 3 mm was placed to the empty side of the coil. First layer design of the marker device is depicted in figure 4.28.

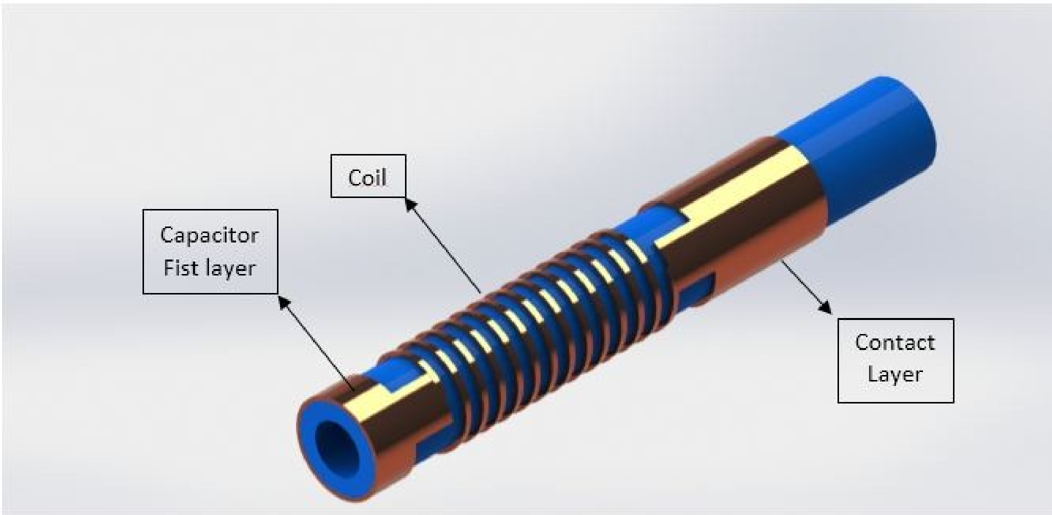

Figure 4.28 First layer of marker device design.

After first layer formation, a parylene layer was coated with the thickness of 3μm and second layer of the resonant circuit was formed on that parylene layer. On that second layer a final parylene layer was coated as an insulation layer. These fabrication steps and the final form of marker device are depicted in figure 4.29.

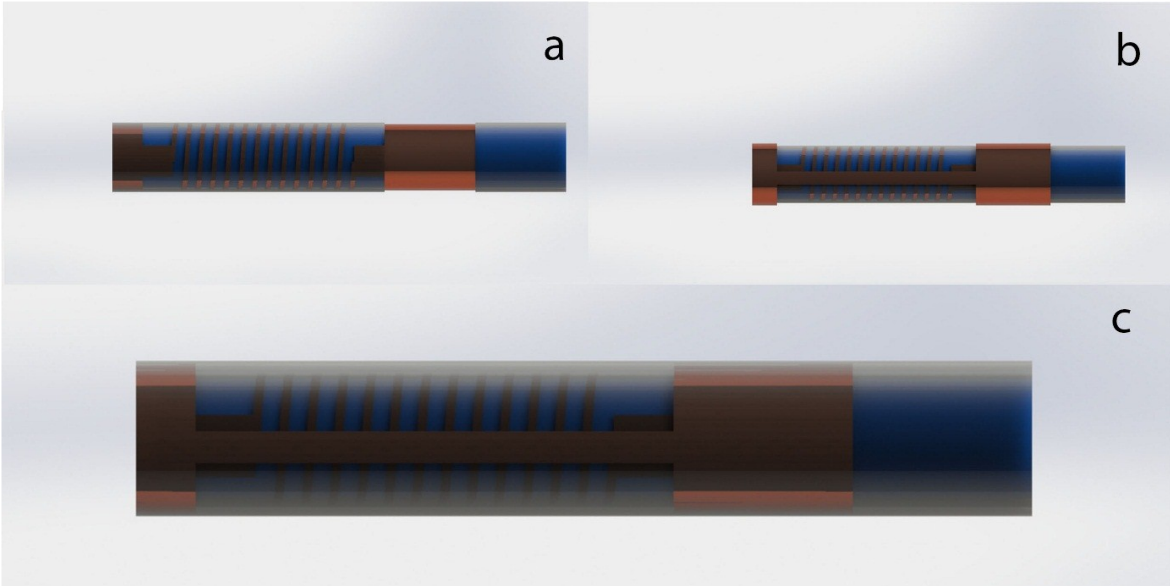

Figure 4.29 (a) Parylene coating on first layer, (b) second layer on parylene layer, (c) isolated final form of marker device.

Designed marker device so that the LC resonant circuit was simulated in HFSS simulation software. Figure 4.30 shows S11 plot of designed circuit. Due to simulation results, resonance frequency of circuit is calculated as 62.74 MHz. This frequency shift from 63.66 Mhz is caused by that roughly 1 mm is used for capacitor length instead of exact value. It was considered acceptable and design was planned to be left like this for flexibility. It is planned to trim the excessive portion of the capacitor within network analyzer measurements and tune the resonant circuit exactly to 63.66 MHz.

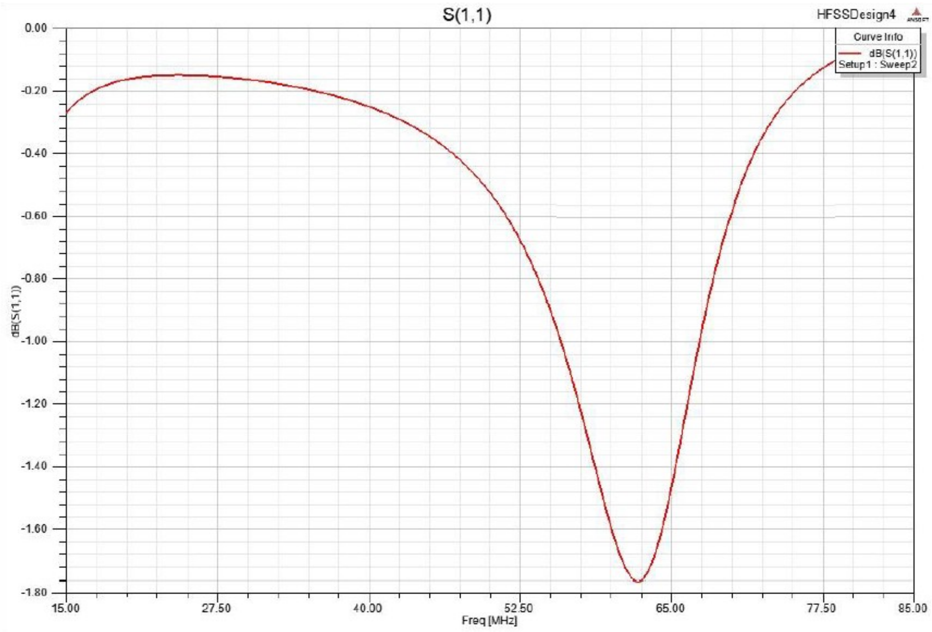

Figure 4.30 S11 plot of resonant circuit.

Figure 4.31 shows the simulated magnetic field around resonant circuit when it is used as a signal source.

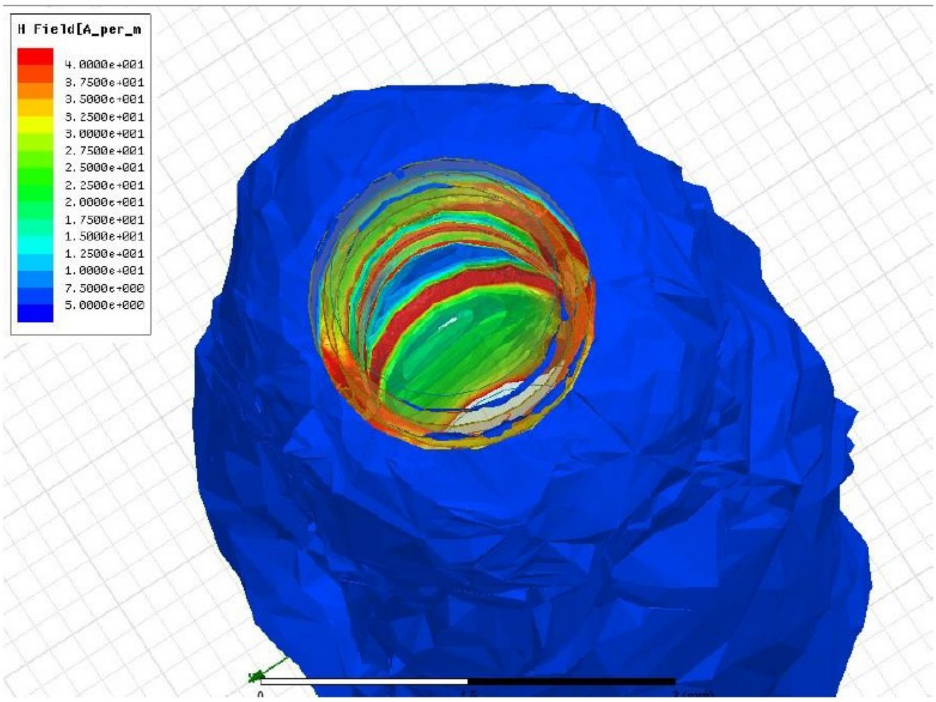

Figure 4.31 Magnetic field around the catheter.

4.3.2 Distal Tip Marker Device Fabrication

Depicted device design in figure 4.29 with coil and capacitor patterns were formed on a 6Fr catheter wall by using conductive ink. Thickness of the formed layer was measured to check if it meets the electrical characteristic requirements.

4.3.3 Printed Component Characterizations

Electrical characteristics of printed coil in terms of resistivity and inductance values were measured via vector network analyzer. One port measurement was performed during this laboratory study. First, network analyzer was calibrated for specifically designed probes.

4.3.3.1 Network analyzer calibration. One port measurement was carried out using the vector network analyzer in order to investigate the physical and electrical characteristics of the printed coil successfully. At the beginning of each study, the port has to be calibrated by using special probes. For this purpose, 3 different calibration probes were prepared using coaxial cables, and electrical components. One end of each of 3 coaxial cable parts with a length of 20 cm were bound to BNC connectors. The other end of the first of them was left unconnected to create an open circuit calibration probe. The inner conductor and outer conductor layer parts of the second coaxial cable were soldered together at its respective and to create a short circuit calibration probe. A 50Ω surface mount resistor with 0805 package were soldered between the conducting layers of the third probe to prepare the third and last calibration probe, which is the match probe.

As the calibration is done successfully, smith chart generated by network analyzer was used to determine electrical characteristics of the printed coil. Coil was connected to a measurement probe same as the open circuit calibration probe with one end is connected to inner conductor of the probe and the other end is to outer conductor layer of the probe. Measurement probe was connected to S11 port of network analyzer.

Thickness of printed layer needs to be increased regarding to two major problems. First one is the high resistance of printed coil and the second one is skin effect.

According to skin effect, high frequency alternating current has a tendency to be distributed within a conductor as the current density is largest near the surface area of the conductor and decreases through the deeper parts. As the frequency increases, alternating current flows mainly at the near-surface parts (skin) of the conductor, between edges of the conductor and a certain level called skin depth [88]. Skin depth can be calculated with the Equation 4.8.

$$\delta = \sqrt{\frac{\rho}{\pi f \mu}} \tag{4.8}$$

Where δ is the skin depth, ρ is the resistivity of the conductor, f is the frequency in Hertz and μ is the absolute magnetic permeability of the conductor

Skin depth for 63.66 MHz is calculated as 8.171μm for copper conductors and 7.944μm for silver conductors.

Thickness of the printed layer was increased by means of copper electroplating in order to overcome both resistivity and skin effect problems.

4.3.3.2 Seed layer Copper Electroplating. . Conductor layer thickness was increased to 15μm by copper electroplating the silver based conductive ink layer both to ensure that the thickness of coil conductor surpass the required skin depth and to decrease resistivity of conductor paths to a reasonable level. Even though the higher thickness means the lower resistivity so that the higher quality factor for the coil, as the thickness increases, flexibility of conductor decreases and it becomes more fragile.

Circuit path thickness was limited to 15μm in order to preserve the flexibility for structural integrity during steering.

Copper electroplating was applied for 8 minutes with 30mA current density to obtain this thickness. Resistivity of coil was also decreased to a reasonable level after copper electroplating.

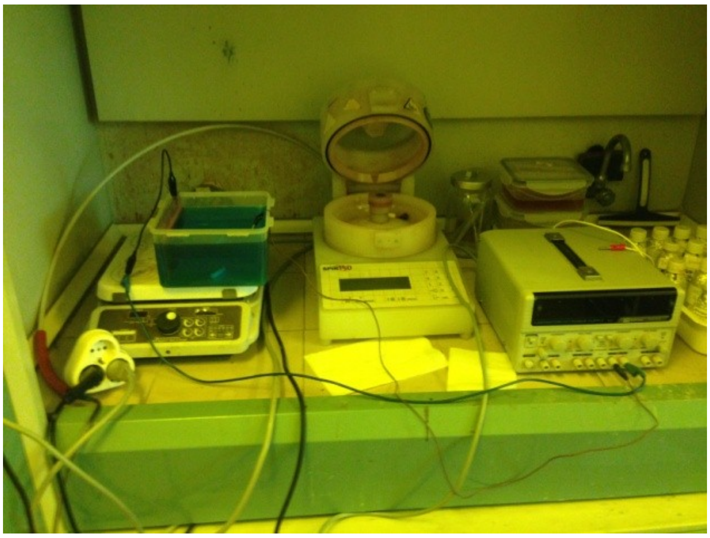

Figure 4.32 Copper electroplating setup.

4.3.3.3 Parylene Coating. A dielectric material is needed to be coated between two conductor plates in order to build a capacitor component. Parylene-C was used both as dielectric material and as final insulator within this thesis study. 3μm is targeted as dielectric material thickness and all capacitance calculations and capacitor designs were made according to this value. After several experiments, it was discovered that 2.4 grams of Parylene-C material is needed for coating of 3μm parylene layer. Final parylene coating thickness was measured with stylus profiler (Dektak XT, Bruker, MA, USA).

Second layer of the resonant circuit was printed onto parylene layer as depicted in figure 4.29.b. Copper electroplating was applied to the second layer in order to decrease second layer's resistivity and to provide enough skin depth.

4.3.3.4 Resonance Frequency Measurement. Before that the marker device is tested under MRI, it needs to be well tuned to larmour frequency. For that purpose, resonance frequency of final prototype was first measured in the air and then it was measured in a liquid phantom environment to mimic the human body. Final tuning of the resonance frequency was carried out in liquid phantom.

Since the final prototype is parylene coated and encapsulated, it is unable to measure its resonance frequency via physical contact. So that, it was measured by using a non-contact sniffer probe. Sample resonant circuit was placed to the center of this coil and a span of frequency is transmitted from sniffer probe. A power loss at the resonance frequency of measured circuit is expected due to inductive coupling between resonant circuit and transmitter. By observing this power loss, resonance frequency of sample resonator was measured.

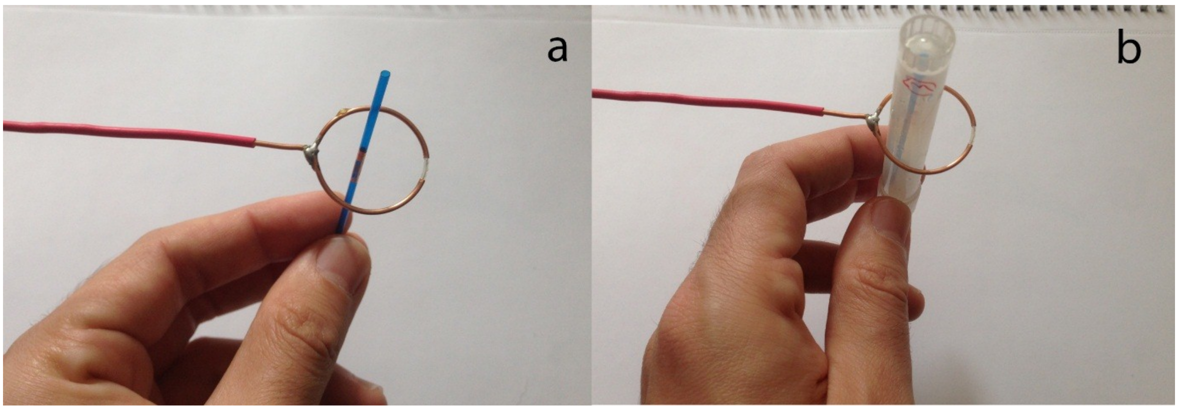

Figure 4.33 Non-contact measurement of resonant circuit (a) in the air, (b) in liquid phantom.

4.3.4 MRI Tests of Marker Device

Once the resonant marker device fabrication was done successfully and its consistency and tuning to 63.66 MHz in phantom environment were confirmed with laboratory studies, it was tested with MRI for visibility and RF induced heating purposes.

For that Purpose, 1.5T Siemens Espree (Siemens AG, Erlangen, Germany) MR scanner system allocated by Acıbadem Hospital (İstanbul, Turkey) was used. The visibility and MR safety performance of the resonant marker device was tested with a water filled phantom using SSFP and GRE sequences (16 interleaves, TE/TR =1.7/3.4 ms, flip = 5°, FOV = 300 mm, matrix = 192 x 192, slice thickness = 6 mm).

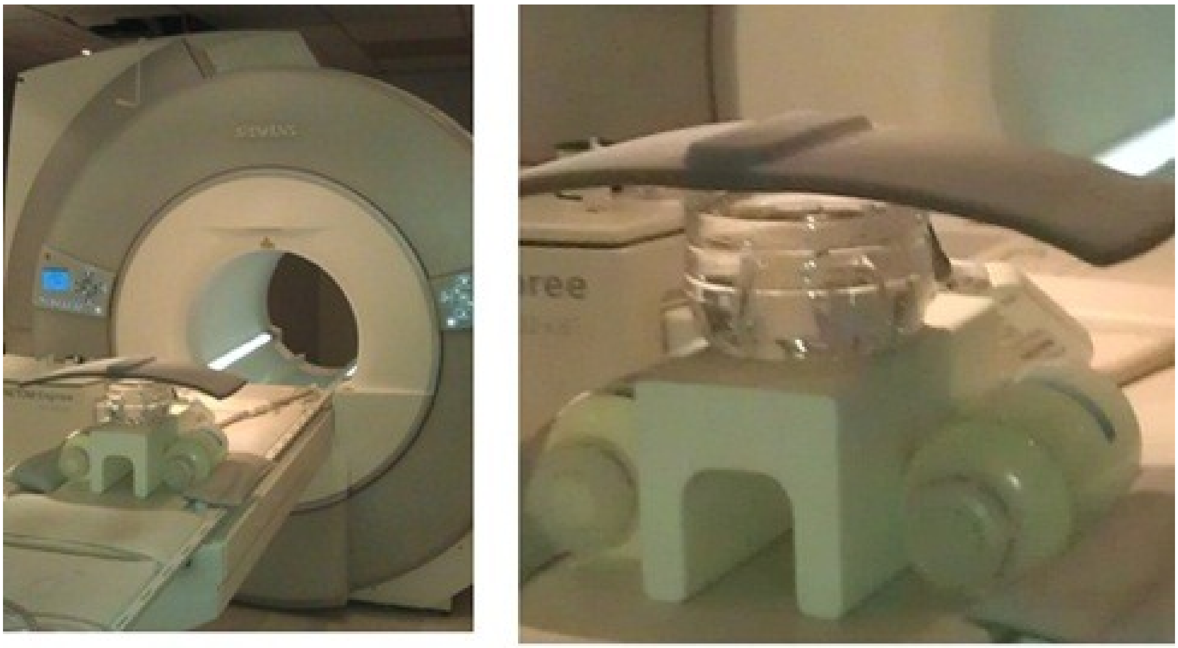

Figure 4.34 MR setup for visibility and safety performance tests.

5. RESULTS

5.1 System Calibration and test results

Mechanical accuracy tests were carried out to calibrate mechanical and dispenser system. Same tests were carried out after that the configuration of the controller was modified.

5.1.1 Measurements before Calibration

In figure 5.1, a test sample is shown (a) with 10 straight lines around a catheter wall with 1 mm distance between the lines.

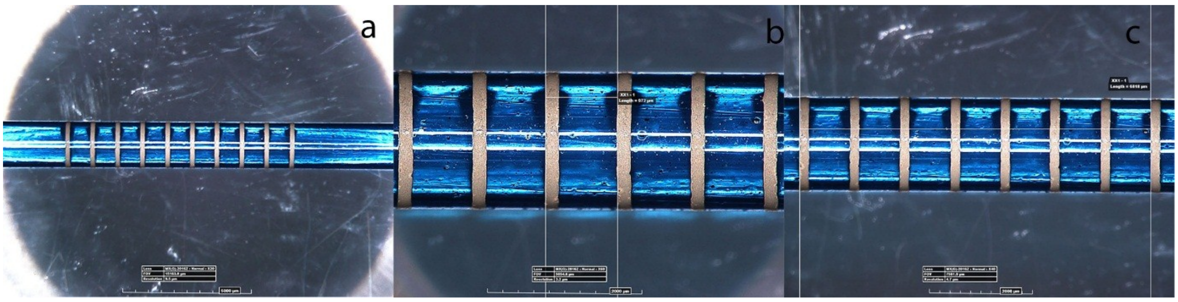

Figure 5.1 (a) 10 Straight lines with 1mm gap, (b) distance between two lines, (c) distance between eight lines.

The distance between two lines (b) was measured as 972 μm (figure 5.1) and the distance between first and eighth lines (c) was measured as 6818 μm (figure 5.1) for the first sample.

This measurement was repeated with 3 different samples and the results were measured as 972, 969 and 977 μm. The error was measured as 27.33 $\mp$ 3.3 μm.

In figure 5.2, a test sample is shown (a) with 5 straight lines around a catheter wall with 3 mm distance between the lines.

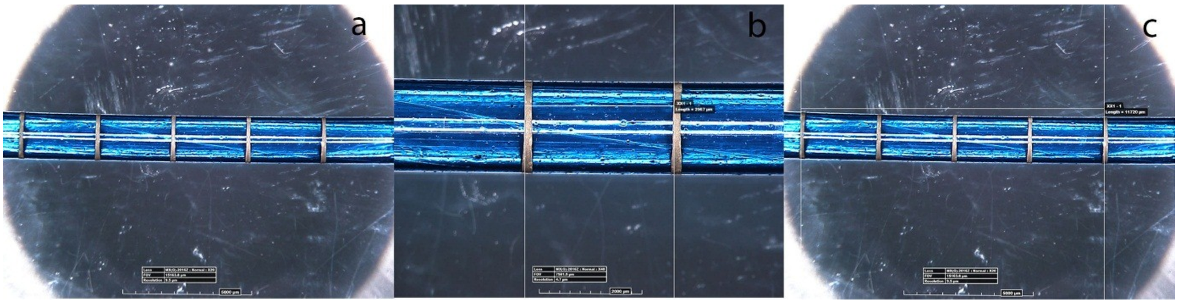

Figure 5.2 (a) Straight lines with 3 mm gap (b) distance between two lines, (c) distance between 4 lines.

The distance between two lines (b) was measured as 2967 μm (figure 5.2) and the distance between first and fifth lines (c) was measured as 11720 μm (figure 5.2) for the first sample.

This measurement was repeated with 3 different samples and the results were measured as 2967, 2955 and 2971 μm. The error was measured as 35.66 $\mp$ 6.8 μm.

In figure 5.3, a test sample is shown with (a) 3 straight lines around a catheter wall with 5 mm distance between the lines.

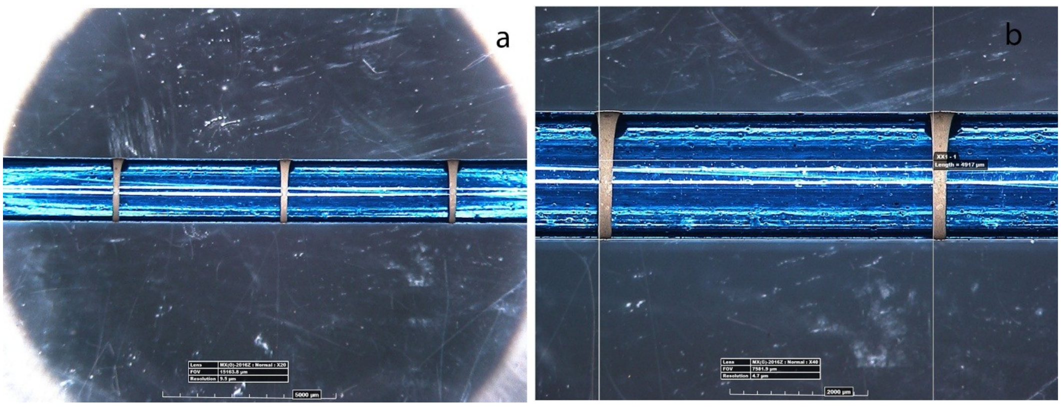

Figure 5.3 (a) Straight lines with 5 mm gap, (b) distance between two lines.

The distance between two lines (b) was measured as 4917 μm (figure 5.3) for the first sample.

This measurement was repeated with 3 different samples and the results were measured as 4917, 4901 and 4924 μm. The error was measured as 86 $\mp$ 9.62 μm.

In figure 5.4, a test sample is shown (a) with 2 straight lines around a catheter wall with 10 mm distance between the lines.

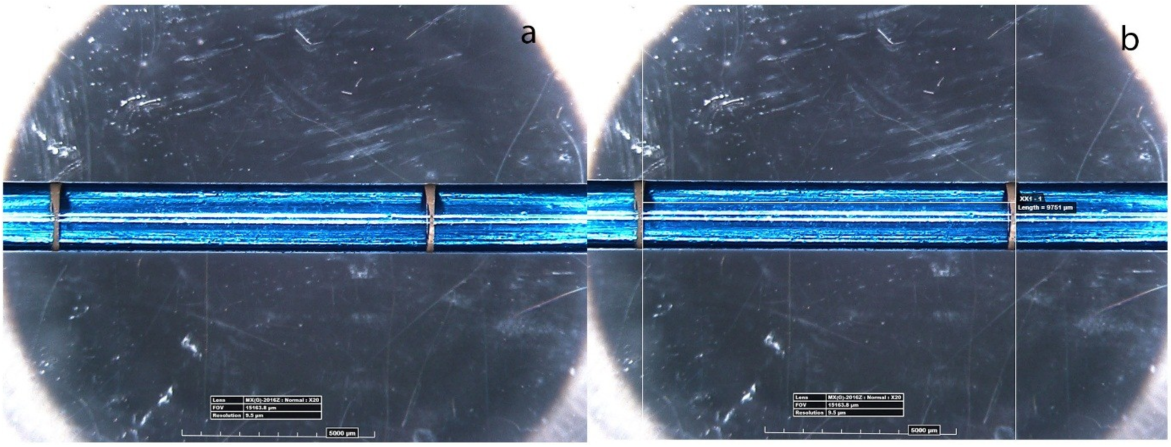

Figure 5.4 (a) Straight lines with 10 mm gap, (b) distance between two lines.

The distance between two lines (b) was measured as 9751 μm (figure 5.4) for the first sample.

This measurement was repeated with 3 different samples and the results were measured as 9751, 9714 and 9768 μm. The error was measured as 255.6 $\mp$ 22.5 μm.

Rotary axis' calibration was also tested by drawing a straight line horizontally on the catheter wall and then tube is rotated for 360°. Then same horizontal straight line is drawn again. By measuring the distance between two lines, error margin was measured. Since the two lines overlapped during tests, pulse number is not modified for rotary axis. Since, there is no transmission mechanism at rotary axis and the chuck is directly connected to electrical motor, no gap exist between parts so that this result was expected.

5.1.2 Measurements after calibration

Same tests and measurements were done for 1, 3, 5 and 10 mm distances in order to confirm calibration.

In figure 5.5, a test sample is shown with straight lines around a catheter wall with 1 mm distance between the lines.

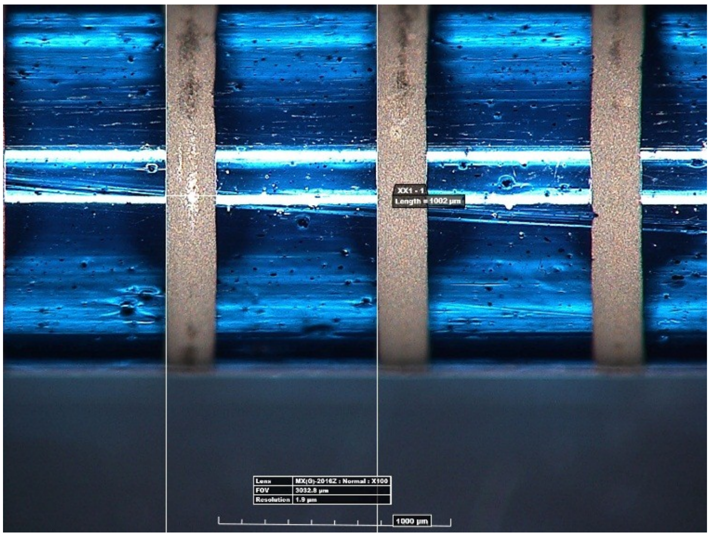

Figure 5.5 Distance between two lines after 1mm test.

After the calibration, result of 1 mm test was measured as 1002 μm for the first sample (figure 5.5).

This measurement was repeated with 3 different samples and the results were measured as 1002, 1002 and 1001μm. The error was measured as 1.66 ∓ 0.4 μm.

In figure 5.6, a test sample is shown with straight lines around a catheter wall with 3 mm distance between the lines.

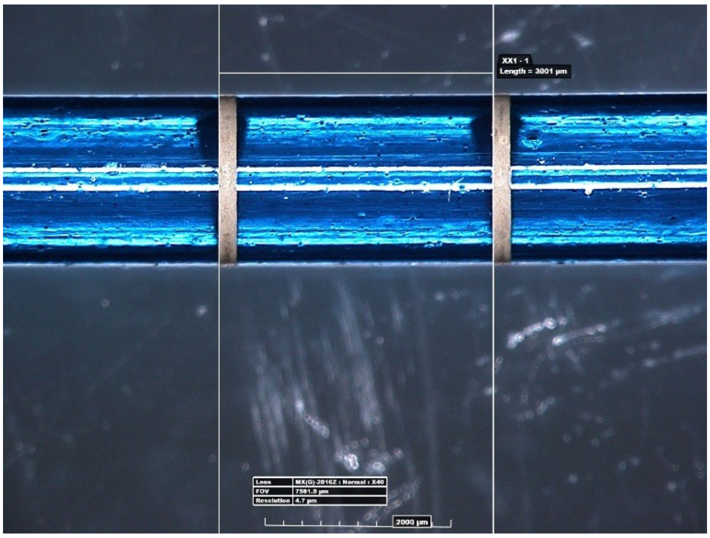

Figure 5.6 Distance between two lines after 3mm test.

After the calibration, result of 3 mm test was measured as 3001 μm for the first sample (figure 5.6).

This measurement was repeated with 3 different samples and the results were measured as 3001, 3003 and 3001μm. The error was measured as 1.66 ∓ 0.9 μm.

In figure 5.7, a test sample is shown with straight lines around a catheter wall with 5 mm distance between the lines.

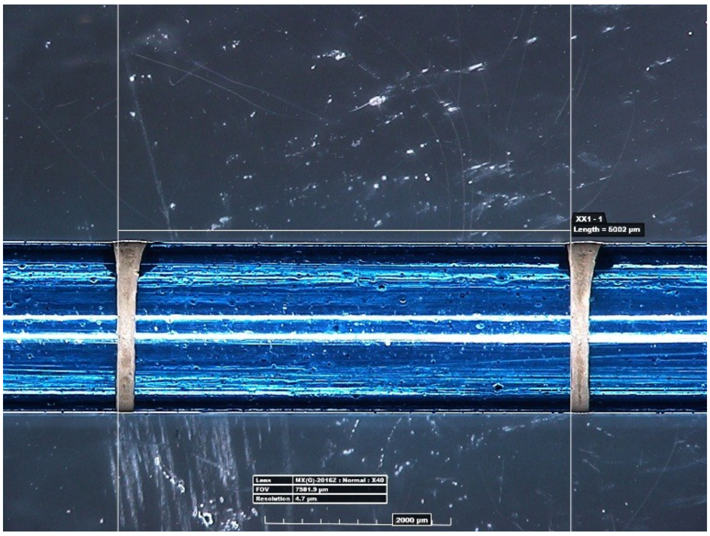

Figure 5.7 Distance between two lines after 5mm test.

After the calibration, result of 5 mm test was measured as 5002 μm for the first sample (figure 5.7).

This measurement was repeated with 3 different samples and the results were measured as 5002, 5001 and 5003μm. The error was measured as 2 ∓ 0.8 μm.

In figure 5.8, a test sample is shown with straight lines around a catheter wall with 10 mm distance between the lines.

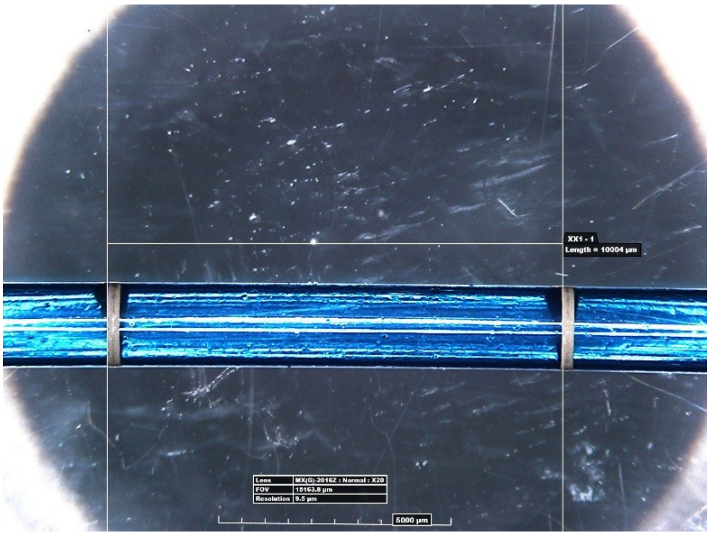

Figure 5.8 Distance between two lines after 10mm test.

Finally, the result of 10 mm test was measured as 10004 μm for the first sample (figure 5.8).

This measurement was repeated with 3 different samples and the results were measured as 10004, 10001 and 10002μm. The error was measured as 2.3 ∓ 2.24 μm.

After that the calibration is carried out successfully, mean error margin for 5mm distance was calculated as 2 ∓ 0.8 μm which is in desired range of design.

5.1.3 Backlash Measurement

Once completing the backlash test, distance between the lines at both ends was measured as 9856 μm (figure 5.9) and backlash of X axis was calculated as 144 μm.

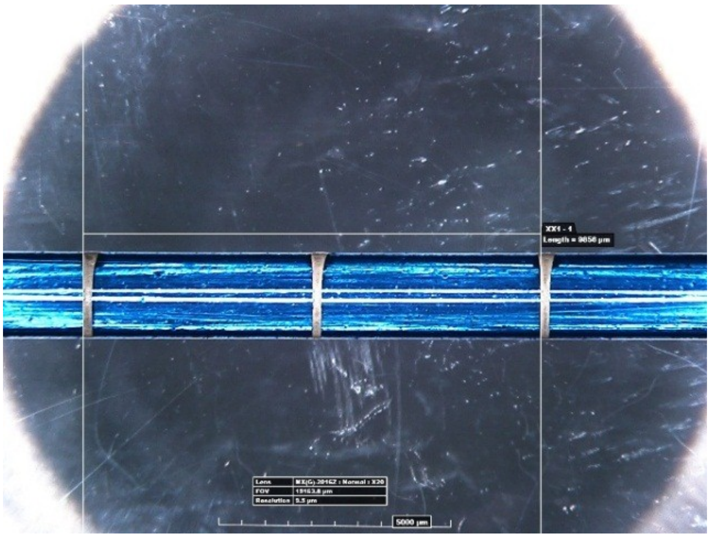

Figure 5.9 Backlash measurement, before calibration.

After configuring the control system regarding to backlash test results, same test was carried out and distance was measured as 10001 μm (figure 5.10).

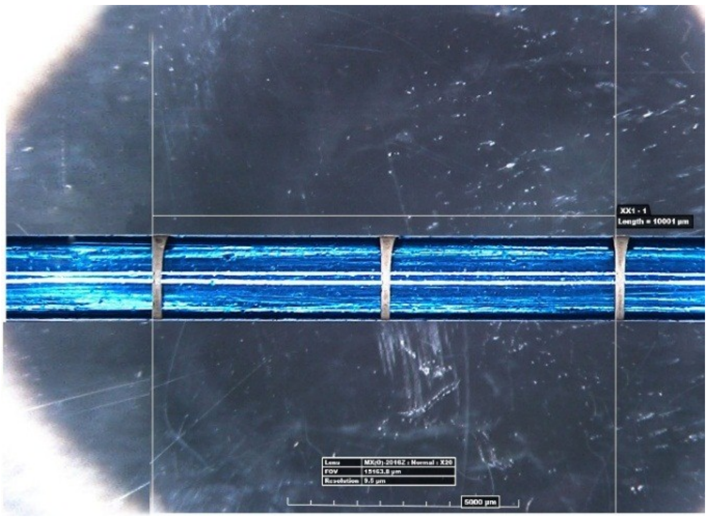

Figure 5.10 Backlash measurement, after calibration.

This test was repeated for three times and measurement results were 10001, 9998 and 10002 μm. The error was measured as 0.3 ∓ 1.69 μm.

5.1.4 Various Pattern Formations over Catheter Shaft.

Several resonator component geometries were formed over 6Fr catheter wall.

First, straight helical coil patterns with 150 μm line width were formed on the catheter shaft successfully (figure 5.11).

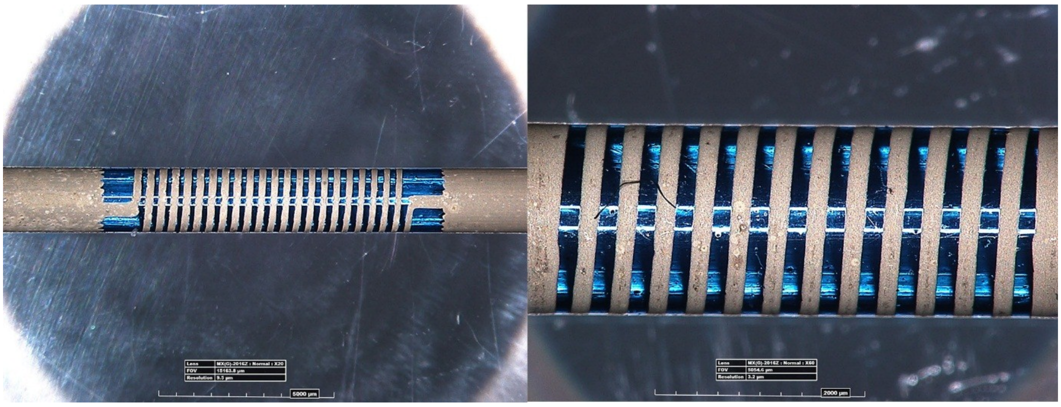

Figure 5.11 Straight coil pattern, formed on the catheter wall.

Second, tilted helical coil geometries with 150 μm line width were formed over catheter wall (figure 5.12).

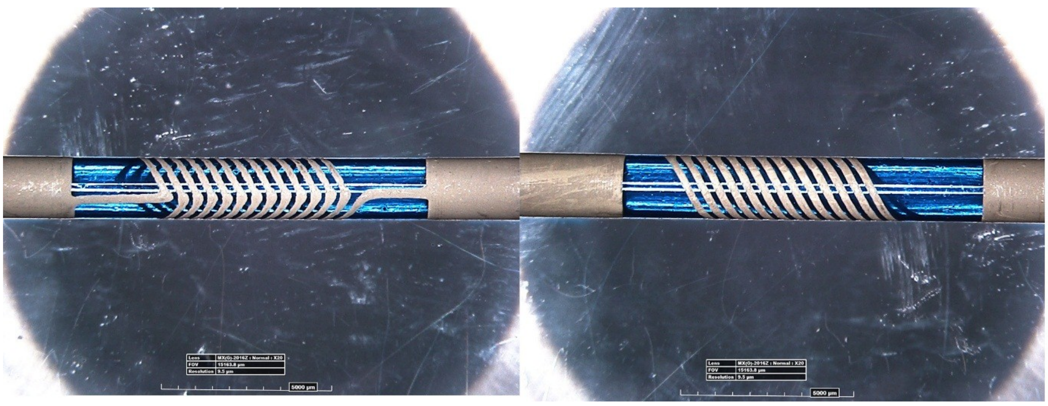

Figure 5.12 Tilted coil pattern formed on the catheter wall.

Then, segmented and ring capacitor designs and first layer capacitor designs for first layer LC tank circuits were formed (figure 5.13).

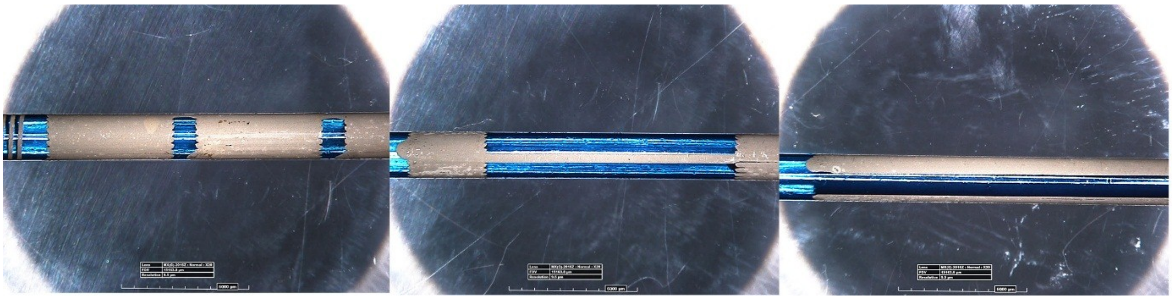

Figure 5.13 Different capacitor patterns, formed on catheter wall.

Once confirming the consistency of formed geometries, more complex designs like coil and capacitor combinations and stent geometries were formed over catheter shaft successfully (figure 5.14 and 5.15).

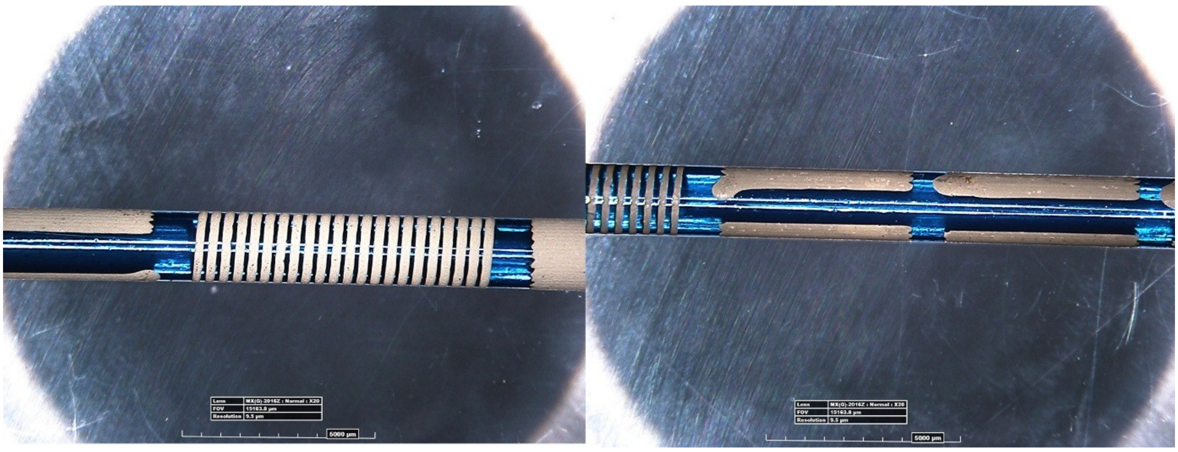

Figure 5.14 Combination of coil and capacitor patterns formed on the catheter wall.

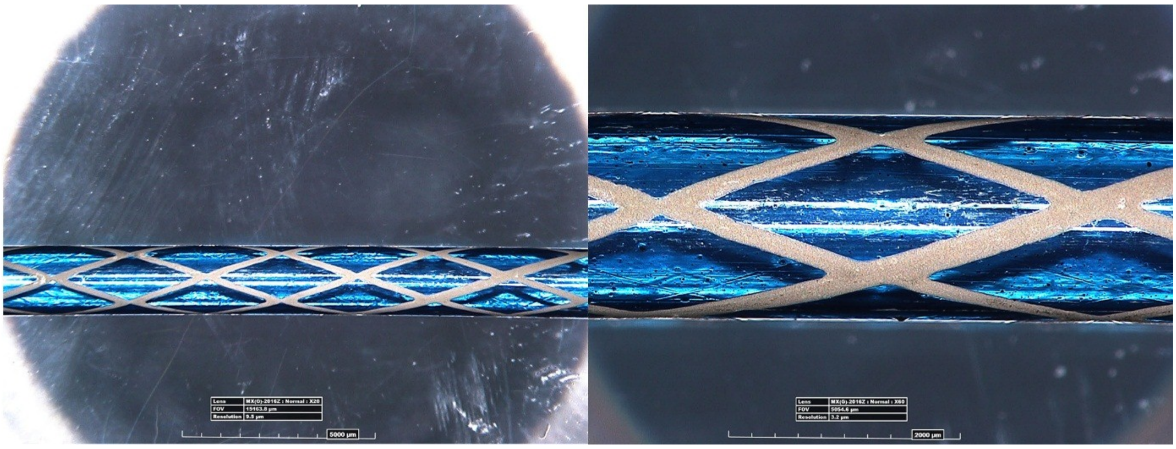

Figure 5.15 Basic stent geometries formed on the catheter wall.

5.1.5 Dispenser System Calibration Results

Dispensed volumes were controlled by custom smart dispenser control software. Dosing tests were repeated for three times and average measurement results can be seen in table 5.1.

Table 5.1
Dispensed volume test results.

Volume of Dispensed Volume (cc)	Theoretical Weight (g)	Measured Weight (g)
0.1	0.1147	0.1135
0.01	0.0114	0.0104
0.001	0.0011	0.0006

Results in table 5.1 shows that, dispenser unit works with %98.95 accuracy for 0.1cc, %91.22 accuracy for 0.01cc but %54.54 accuracy for 0.001 cc. These results shows that dispenser unit accuracy increases with the amount of dispensed volume. The reason why the accuracy drops to %54 for 0.001 cc was investigated and it was understood that, since the ejected amount is so little, a portion of the liquid cannot be ejected from the nozzle and remains in the ejection channel. Dispensing process for 0.001cc was repeated for 20 times to obtain 0.02cc ejection to test this small amount of ejection. At the end of 20th ejection cycle, rest of the process was carried out and the weight was measured as 0.0207g which is more than %90 accurate.

5.2 Resonant Marker Measurements

Resonant marker design incorporating a solenoid coil, a capacitor layer and a contact area with calculated dimensions was formed over catheter shaft.

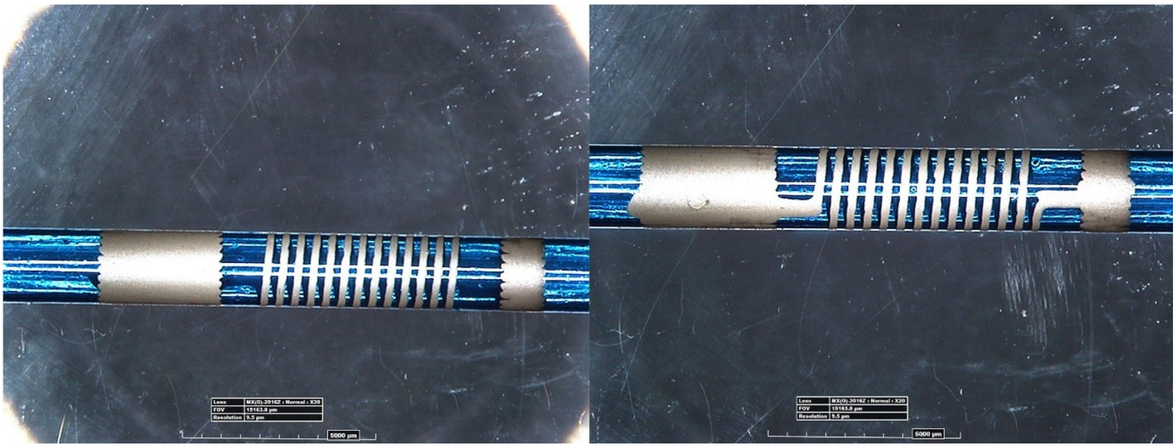

Figure 5.16 Printed coil and capacitor patterns on the catheter wall.

Length of contact layer was measured as 2997 μm, length of capacitor's first layer was measured as 1002 μm, coil length was measured as 5004 μm and the length of contact paths between coil - capacitor and coil - contact layer is measured as 1002 μm (figure 5.17).

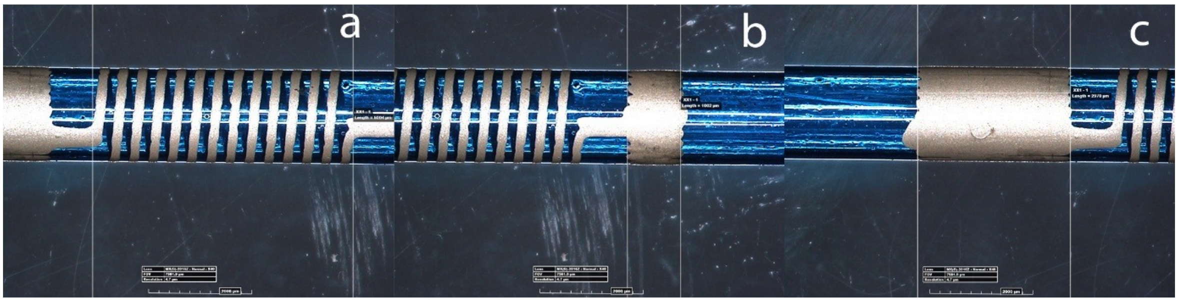

Figure 5.17 (a) Coil length measurement, (b) capacitor first layer length measurement, (c) contact layer length measurement.

Formed first layer thickness was measured as 7 μm (figure 5.18).

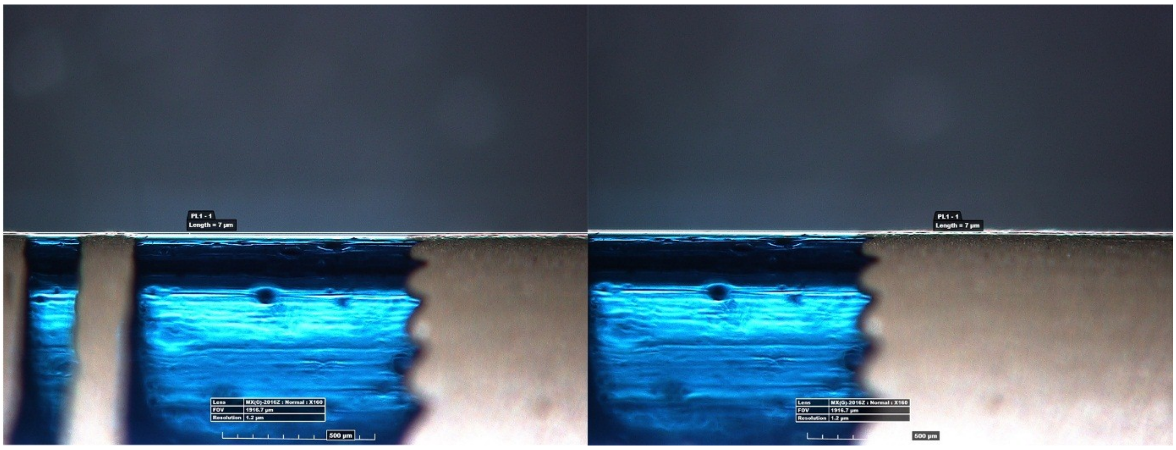

Figure 5.18 Printed conductive ink thickness measurement.

Inductance of the printed coil with 5 mm length and 13 turns, was measured as 123.1 nH, which was designed for 125 nH. Resistivity of the coil was measured as 41.1Ω + j49.4Ω (figure 5.19).

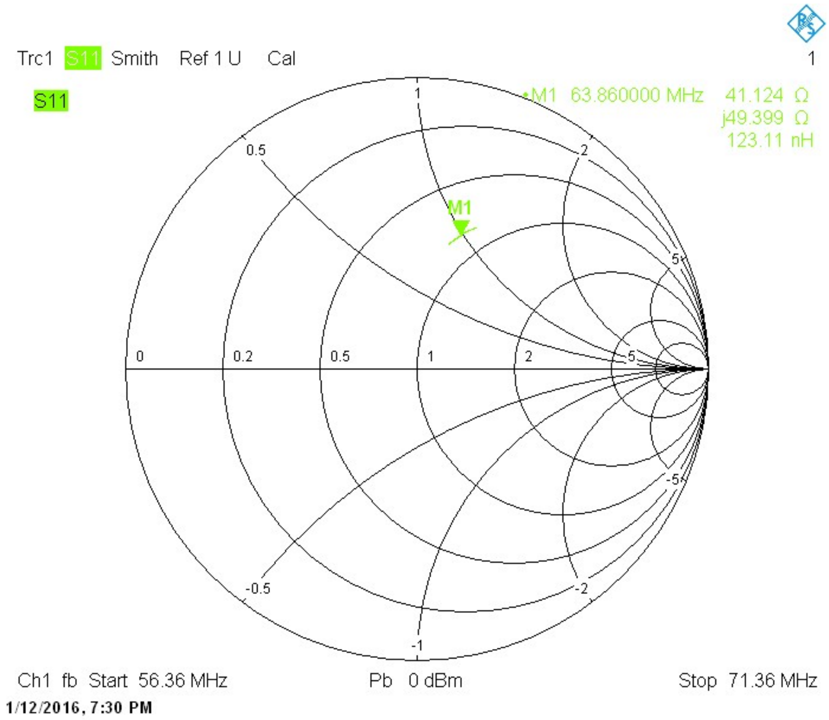

Figure 5.19 Smith chart diagram of coil measurement.

Copper electro-plating was applied to conductive ink layer with 30mA current for 8 minutes (Figure 5.20).

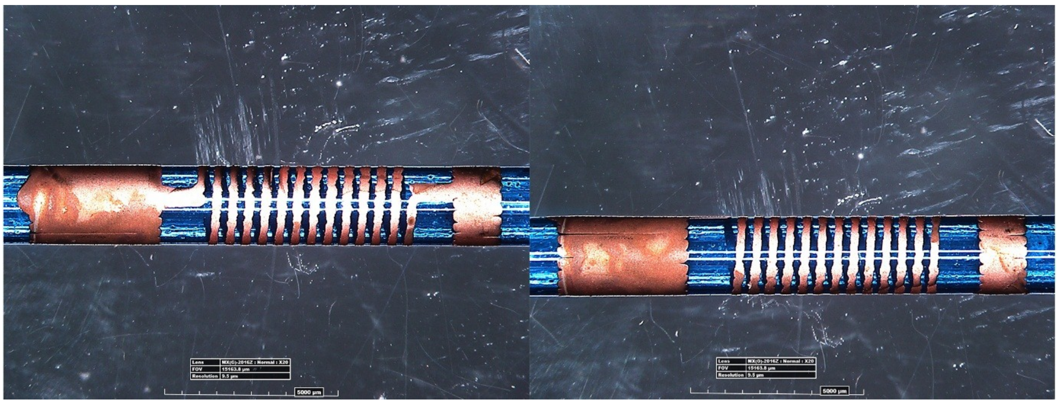

Figure 5.20 First layer of resonant circuit after copper electroplating.

After copper electroplating is applied, thickness of the first layer was measured as 15μm (figure 5.21).

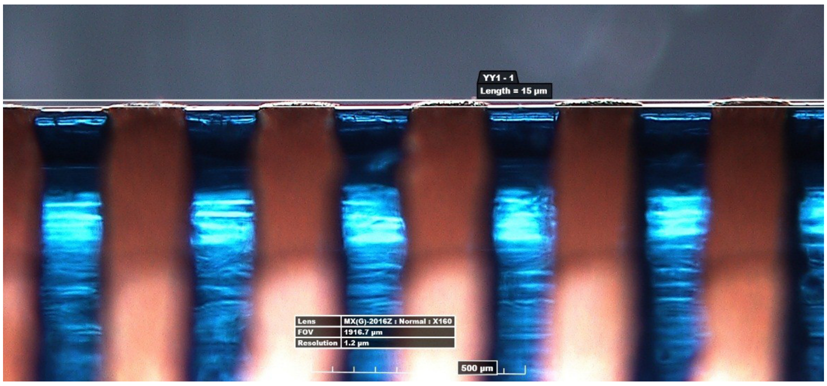

Figure 5.21 First layer thickness measurement after copper electroplating.

Resistivity of coil was also decreased to a reasonable level after copper electroplating is applied and it was measured as 2.64Ω + j48.49Ω (figure 5.22).

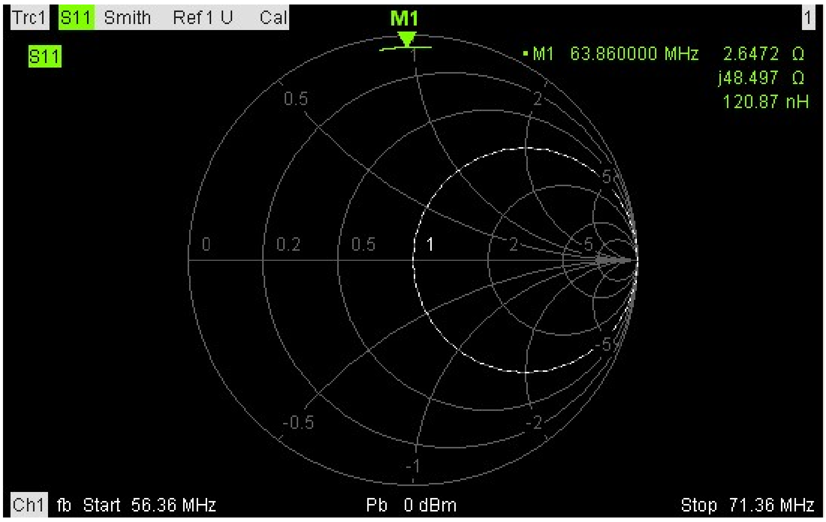

Figure 5.22 First layer thickness measurement after copper electroplating.

5.2.1 Parylene Coating Measurements

Parylene thickness after coating of 2.4g parylene was measured as 3μm. (figure 5.23)

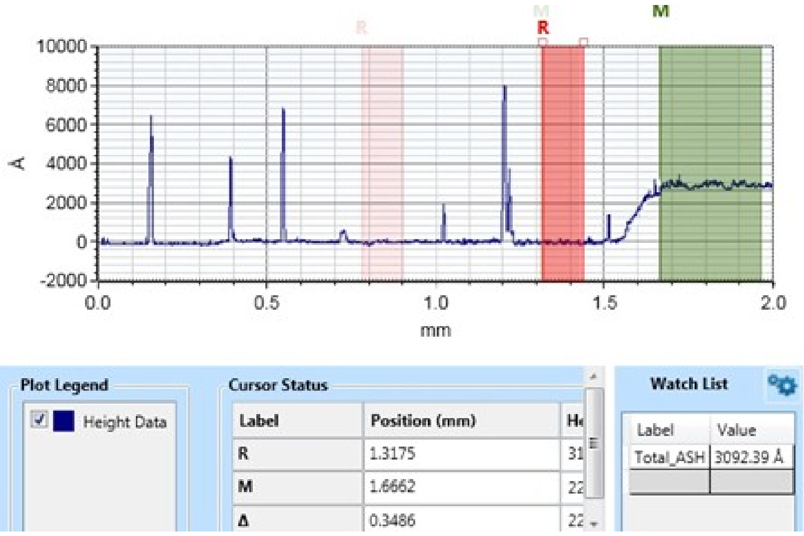

Figure 5.23 Parylene thickness measurement.

A slight decrease in inductance value of the coil was observed after parylene coating. This was expected because of the change in filling factor caused by surrounding parylene. Inductance value of the coil decreased to 119nH (Figure 5.24).

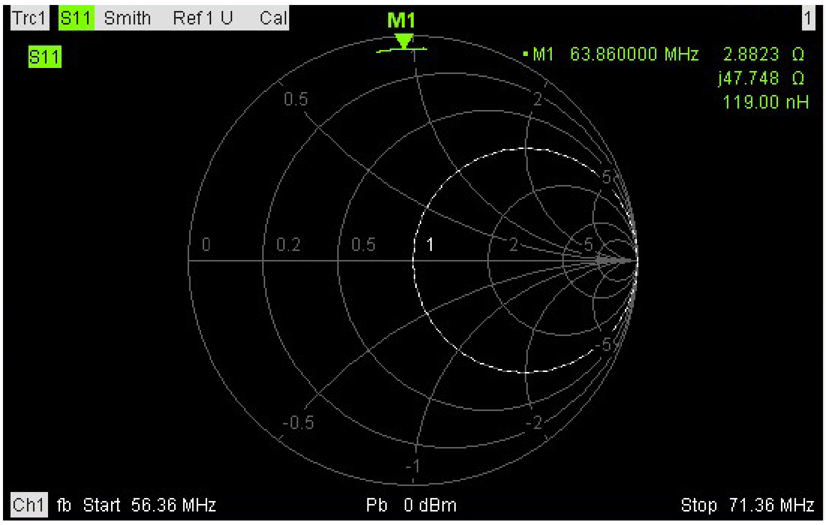

Figure 5.24 Inductance measurement after parylene coating.

Same procedure for the first layer was applied for the second layer also with a different geometry to complete marker device fabrication.

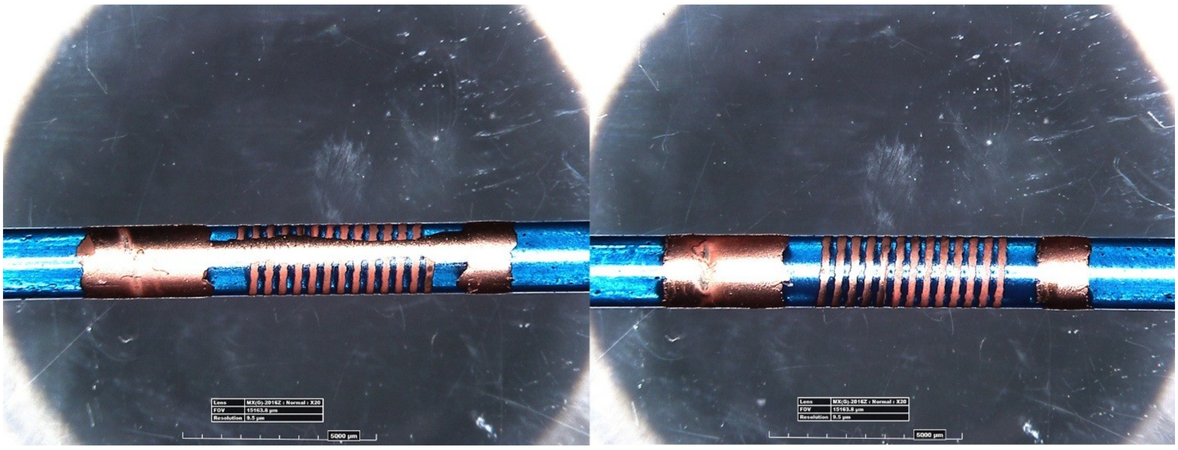

Figure 5.25 Second layer of the resonant circuit built on the first layer and copper electroplated.

Final thickness of marker device which includes two conductor layers and two parylene layers, was measured as 35μm.

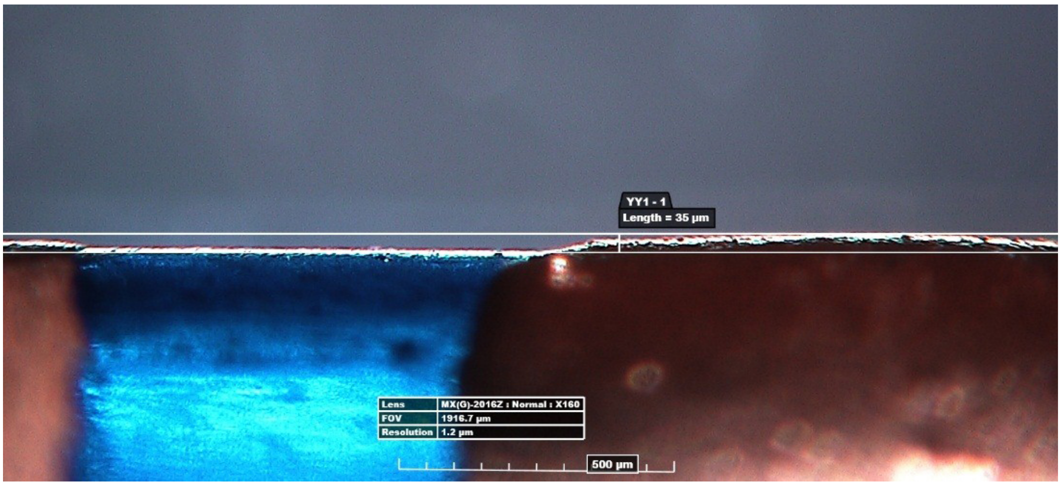

Figure 5.26 Measurement of device profile.

5.2.2 Resonance frequency Measurements

Resonance frequency of the resonant circuit was measured as 64.63 MHz in the air (figure 5.27) and 63.66 Mhz in the liquid phantom (figure 5.28). Gain of the marker was measured as -1.79 dB in the air and -1.14 dB in the liquid phantom.

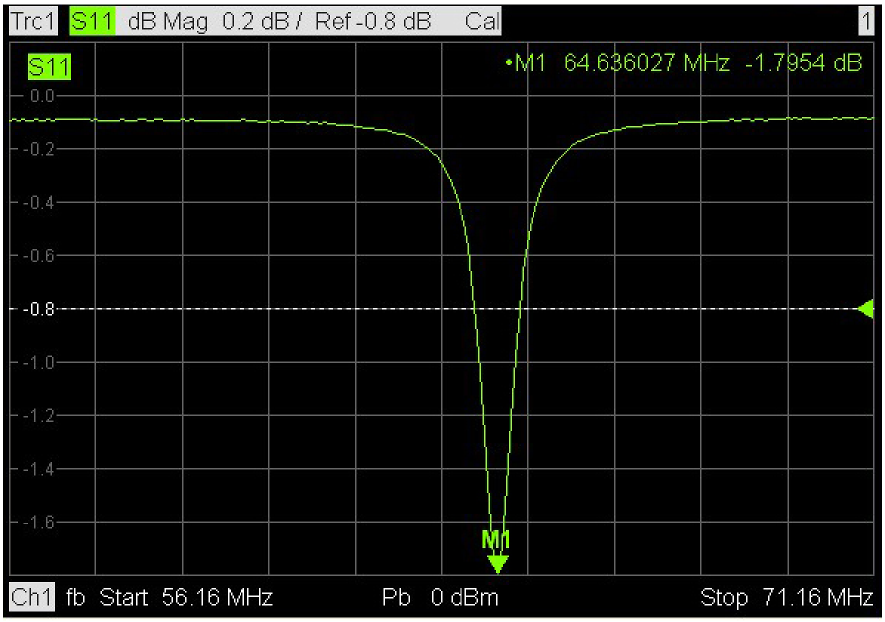

Figure 5.27 Resonance frequency of marker, in the air.

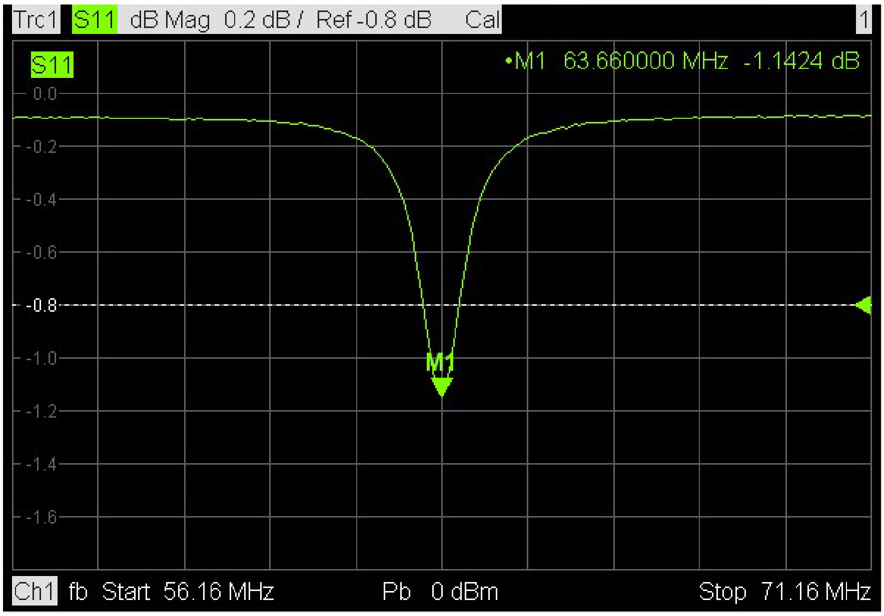

Figure 5.28 Resonance frequency of marker, in liquid phantom.

5.2.3 Resonant Marker Tests under MRI

Visibility and RF induced heating tests of prototyped marker were performed successfully under MRI.

5.2.3.1 Visibility Test. With both SSFP and GRE sequences with 5° Flip angle, fabricated marker device was spotted out as a distinguishable bright spot.

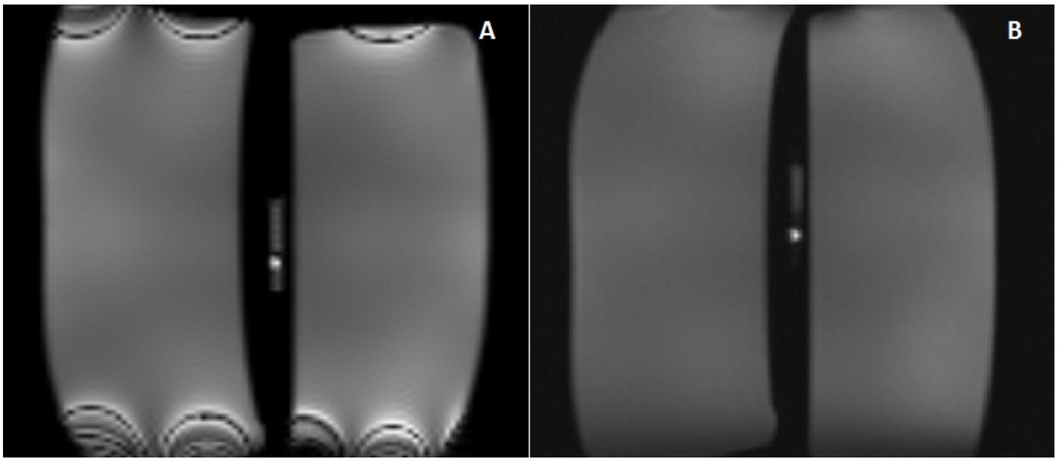

Figure 5.29 MR imaging of marker, performed in water filled phantom (A) SSFP Sequence Image (B) GRE Sequence Image.

5.2.3.2 MR Safety Test. Heating performance of the resonant marker under MRI was also tested (Catheterization Lab, NHLBI, National Institutes of Health, MD, USA) and it was observed that, RF induced heating risk is eliminated compared to same profile active device.

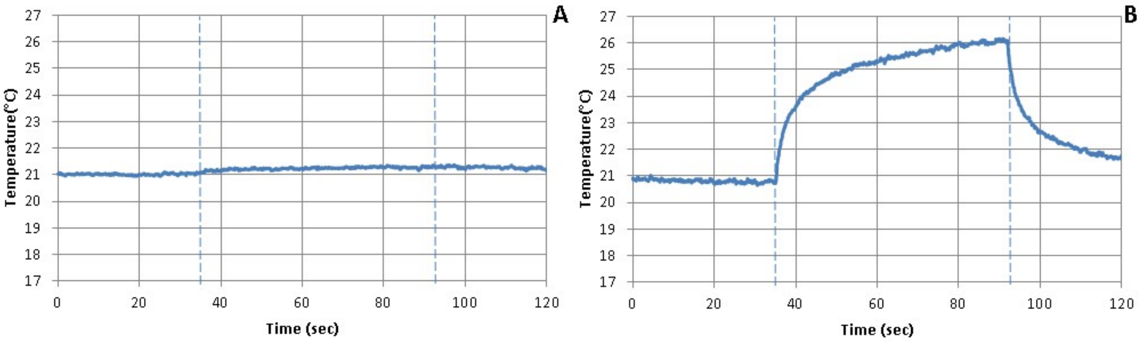

Figure 5.30 RF induced heating test of (A) conductive ink based semi-active marker (ΔT=0.35 °C), (B) active catheter marker (ΔT=5.34 °C) performed in water filled phantom. (Dash lines indicates the point of MR Scan Start and MR scan stop)

6. DISCUSSION

In this thesis study, a computer controlled MRI device fabrication system was designed and manufactured. Dimensions of the system were determined regarding to interventional MRI device dimensions that are planned to be fabricated within this fabrication system. Mechanical properties were customized to obtain minimum 4μm precision. Convenient electrical actuators with 2.2 Nm torque capacity were chosen in order to supply enough torque for moving parts. Electronic system was designed to provide computer control to the system. A commercially available control software which is commonly used by the industry was used in order to implement complex device designs by using developed CAM software posts.

Once the fabrication system design was finalized, whole system was prototyped. Calibration of the motion axes were done in order to compensate mechanical malfunctions and assembly faults. Motion system calibration was confirmed with the measurements of 1, 3, 5 and 10mm intervals under a well calibrated microscope. Average error margin for linear movement was measured as 2 ∓ 0.8 μm which is less than the linear motion resolution of the system.

A custom computer controlled liquid dispenser unit was designed and manufactured for conductive ink deposition. A custom software for controlling this unit in both automatic and manual mode was written. Control of this unit was also realized via the same software used for motion control. By weight measurement tests, accuracy of the dispenser unit was checked and accuracy of the system was calculated as %93.65 $\mp$ 3.74 for 0.1, 0.01 and 0.001 cc volumes.

Once the calibration of whole system was confirmed, different geometries were implemented over 6Fr catheter wall. Straight and tilted coil geometries were formed successfully and their inductance values were measured. Different capacitor patterns were also studied adhering to defined dimensions and the results were confirmed with microscope measurements. Since designed fabrication system is also planned to be used for complex stent geometries, some common stent patterns were printed and their consistency of the geometries were confirmed.

It was observed that the formed conductor path thickness and the line width changes proportional to velocity of axes and conductive ink deposition rate. Same patterns with different velocities and different deposition rates were tested.

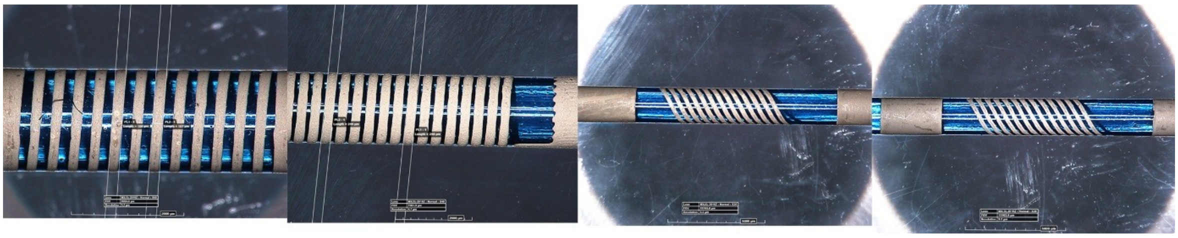

Figure 6.1 Line width changes with different velocity and deposition rates.

As a part of this study, a novel distal tip catheter marker was designed and fabricated by using computer controlled fabrication system based on former simulation results. Simulation results were confirmed with physical measurements of both straight and tilted helical coils which were fabricated adhering to simulated dimensions. Once this simulation setup was confirmed as a promising and reliable tool for coil and resonator design, a resonator marker was designed by incorporating a straight helical coil with 125nH inductance and a ring capacitor with 50pF capacitance which would have 63.66 MHz resonance frequency.

Designed coil and capacitor geometries were implemented on a 6Fr catheter wall. However, formed pattern thickness was 7μm which causes high resistivity and does not meet skin depth requirement which is around 8 μm. Thickness of the layer was increased to 15 μm by copper electroplating in order both to decrease resistivity and to get rid of skin effect. Electrical characteristics of formed coil component were measured via vector network analyzer as laboratory study and inductance value was measured as 120 nH which was calculated to be 125nH and resistance of the coil was measured as $2.64\Omega + j48.49\Omega$. Parylene-c was coated as the dielectric material over first layer with the 3μm thickness to build a capacitor. When the pin hole free coating of parylene was confirmed, second layer pattern of resonant circuit was implemented onto parylene layer. Again the second layer thickness was increased to 15μm by copper electroplating. Finally, second layer of resonant marker was coated with parylene for insulation purposes. When the resonant marker prototype was encapsulated with parylene, resonance frequency of the circuit was measured with vector network analyzer by using a non-contact sniffer probe. Resonance frequency of the marker was measured as 64.63 MHz in the air and 63.66 MHz in the liquid phantom which mimics human body loading conditions. Quality factor of the resonator was measured as 38.8 and gain was measured as -1.14 dB.

Gain of the resonator is relatively low for MRI applications and this is thought to be caused by low number of coil turns and relatively large conductor area used for connecting two circuit layers.

Fabrication time for one layer of the resonant circuit was measured about 60 seconds during several trials and for a complete resonant circuit, it was measured bout 8 hours (due to long vacuum times at parylene coating step). Other fabrication tools like shadow masks or chemical etchants which are used in lithography based fabrication methods, were not used for fabrication and designed patterns were implemented directly onto catheter wall by using conductive ink.

Fabricated resonant marker was tested under 1.5T MRI system in a liquid phantom with SSFP and GRE sequences. With both sequences, marker was visualized as a distinguishable bright spot. Heating test of the marker was performed with a 1.5T MR system and results were compared with a same profile active catheter. While fabricated resonant marker was heated just as 0.35 °C, active catheter marker device was heated as 5.34 °C because of the long transmission line. Electrical length of the resonant marker was calculated as 98,9mm by geometrical means and it is far less than wavelength of 63.66 MHz RF signal. So that, heating did not occur within MR scans.

Results of this study showed that, conductive ink based computer controlled fabrication system is a promising candidate for developing iMRI devices against conventional lithography based fabrication methods. This system allows fabrications in very short periods of time compared to conventional methods (necessary time for fabricating the same resonant marker with thermal evaporation method was measured as two days in previous studies conducted by our group). Thanks to ability of direct pattern implementation and fast process, any fault at fabrication steps or at designed pattern, can be retrieved immediately and this is not possible with conventional methods. Also, complex geometries and multilayer structures are allowed to be fabricated with an acceptable precision via this system without using any other mask or alignment tool. Overall, this fabrication system provided advantages as short fabrication times, elimination of additional fabrication tools like shadow masks, possibility of complex and multilayer device fabrication directly on the substrate with high precision and a reliable repeatability.

Finally, some improvements are planned for the developed fabrication system as the future work. First is to make modifications to implement insulation layers with parylene-like materials within this system to eliminate long vacuum times at parylene coating step. Second is to add another rotary axis to the system. With the help of this fifth axis, it will be possible to process spherical non-planar sample surfaces. Thanks to this ability, more complex geometries can be implemented on various devices like body implants or patient specific device designs. Also, fabrication of another resonant marker device is planned. This marker device incorporates two reversely tilted helical coils and a capacitor in order to cover all axes and to be visible in all orientations within MRI scans.

REFERENCES

1. Lauterbur, P. C., "Image formation by induced local interactions: examples employing nuclear magnetic resonance.," *Nature*, Vol. 242, no. 5394, pp. 190–191, 1973.

2. Garroway, Allen N., Peter K. Grannell, and Peter Mansfield. and P. Mansfield., "Image formation in nmr by a selective irradiative process.," *Journal of Physics C: Solid State Physics*, Vol. 724, no. 457, 1974.

3. Kantor HL, Briggs RW, Balaban RS. "In vivo 31p nuclear magnetic resonance measurements in canine heart using a catheter-coil.," no. 5, pp. 261–266, 1984.

4. Hurst GC, Hua J, Duerk JL, Cohen AM. "Intravascular (catheter) nmr receiver probe: preliminary design analysis and application to canine iliofemoral imaging.," no. 24, pp. 343–357, 1992.

5. Martin AJ, Plewes DB, Henkelman RM. "Mr imaging of blood vessels with an intravascular coil.," no. 9, p. 421, 1992.

6. Raval AN, Telep JD, Guttman MA, et al. "Real-time magnetic resonance imaging-guided stenting of aortic coarctation with commercially available catheter devices in swine.," no. 112, pp. 699–706, 2005.

7. Kleinerman, RA, "Cancer risks following diagnostic and therapeutic radiation exposure in children.," no. 36, pp. 121–125, 2006.

8. Cohen, L., "What can go wrong.," pp. 11–20, 1992.

9. Kleinman, C., "Heart disease in the young.," ch. 20, pp. 247–262, 1992.

10. Escaned J, Goicolea J, Alfonso F, Perez-Vizcayno MJ, Hernandez R, Fernadez-Ortiz A, Banuelos C, Macaya C. "Propensity and mechanisms of restenosis in different coronary stent designs.," in *J Am Coll Cardiol*, ch. 34, pp. 1490–1497, 1999.

11. Baptista J, di Mario C, Ozaki Y, Escaned J, Gil R, de Feyter P, Roelandt JR, Serruys PW. "Impact of plaque morphology and composition on the mechanisms of lumen enlargement using intracoronary ultrasound and quantitative angiography after balloon angioplasty.," in *Am J Cardiol*, ch. 77, pp. 115–121, 1996.

12. Fuster V, Badimon L, Badimon JJ, Chesebro JH. "The pathogenesis of coronary artery disease and the acute coronary syndromes.," in *II. N Engl J Med*, ch. 30, pp. 310–318, 1992.

13. Quick HH, Kuehl H, Kaiser G, Bosk S, Debatin JF, Ladd ME. "Inductively coupled stent antennas in mri," in *Magn. Reson. In Med*, ch. 48, pp. 781–790, 2002.

14. "National research council (u.s.). committee to assess health risks from exposure to low levels of ionizing radiation: Health risks from exposure to low levels of ionizing radiation:," in *BEIR VII Phase 2 Washington, D.C.: National Academies Press*, 2006.

15. Andreassi MG, Ait-Ali L, Botto N, Manfredi S, Mottola G, Picano E, "Cardiac catheterization and long-term chromosomal damagein children with congenital heart disease.," in *Eur Heart J*, ch. 27, pp. 2703–2708, 2006.

16. Omary RA, Green JD, Schirf BE, Li Y, Finn JP, Li D. “Real-time magneticresonance imaging-guided coronary catheterization in swine.,” in *Circulation*, ch. 107, pp. 2656–2569, 2003.

17. Kocaturk O, Saikus CE, Guttman MA, Faranesh AZ, Ratnayaka K, Ozturk C, McVeigh ER, Lederman RJ, “Whole shaft visibility and mechanical performance for active mr catheters using copper-nitinol braided polymer tubes„” in *J Card Magn Reson*, pp. 11–29, 2009.

18. Formica D, Silvestri S. “Biological effects of exposure to magnetic resonance imaging: an overview.,” in *Biomed Eng Online*, pp. 3–11, 2004.

19. Kanal E, Barkovich AJ, Bell C, et al. “Acr guidance document for safe mr practices,” in *AJR Am J Roentgenol*, ch. 188, pp. 1447–1474, 2007.

20. Saikus E, Lederman R.J, “Interventional cardiovascular magnetic resonance imaging: a new opportunity for image-guided interventions„” in *JACC Cardiovasc Imaging*, ch. 2, pp. 1321–1331, 2009.

21. Elgort DR, Hillenbrand CM, Zhang S, et al. “Image-guided and -monitored renal artery stenting using only mri.,” in *J Magn Reson Imaging*, ch. 23, pp. 619–627, 2006.

22. Raman VK, Karmarkar PV, Guttman MA, et al. “Real-time magnetic resonance-guided endovascular repair of experimental abdominal aortic aneurysm in swine.,” in *J Am Coll Cardiol*, ch. 45, pp. 2069–2077, 2005.

23. Raval AN, Karmarkar PV, Guttman MA, et al “Real-time magnetic resonance imaging-guided endovascular recanalization of chronic total arterial occlusion in a swine model.,” in *Circulation*, ch. 113, pp. 1001–1007, 2006.

24. Buecker A, Spuentrup E, Grabitz R, et al. “Magnetic resonance-guided placement of atrial septal closure device in animal model of patent foramen ovale.,” in *Circulation*, ch. 106, pp. 511–515, 2002.

25. Kuehne T, Yilmaz S, Meinus C, et al. “Magnetic resonance imaging-guided transcatheter implantation of a prosthetic valve in aortic valve position: feasibility study in swine.,” in *J Am Coll Cardiol*, ch. 44, pp. 2247–2249, 2004.

26. Susil RC, Yeung CJ, Halperin HR, Lardo AC, Atalar E. “Multifunctional interventional devices for mri: a combined electrophysiology/mri catheter.,” in *Magn Reson Med*, ch. 47, pp. 594–600, 2002.

27. Dukkipati SR, Mallozzi R, Schmidt EJ, et al. “Electroanatomic mapping of the left ventricle in a porcine model of chronic myocardial infarction with magnetic resonance-based catheter tracking.,” in *Circulation*, ch. 118, pp. 853–862, 2008.

28. Krueger S, Lips O, David B, et al. “Towards mr-guided ep interventions using an rf-safe concept.,” in *J Cardiovasc Magn Reson*, ch. 11, p. 84, 2009.

29. Ozgur Kocaturk, Christina E Saikus1, Michael A Guttman, Anthony Z Faranesh, Kanishka Ratnayaka, Cengizhan Ozturk, Elliot R McVeigh and Robert J Lederman. “Whole shaft visibility and mechanical performance for active mr catheters using copper-nitinol braided polymer tubes.,” 2009.

30. Sillerud LO, McDowell AF, Adolphi NL, Serda RE, Adams,DP, Vasile MJ, Alam TM, “H-1 nmr detection of superparamagnetic nanoparticles at 1 t using a microcoil and novel tuning circuit„” in *Journal of Magnetic Resonance*, ch. 2, pp. 181–190, 2006.

31. Rogers JA, Jackman RJ, Whitesides G.M., “Constructing single- and multiplehelical microcoils and characterizing their performance as components of microinductors and microelectromagnets„” in *Journal of Microelectromechanical Systems*, ch. 6, pp. 184–192, 1997.

32. Plewes DB, Kucharczyk W, “Physics of mri: A primer.,” in *J Magn Reson Imaging*, ch. 35, pp. 1038–1054, 2012.

33. Rubin DL, Ratner AV, Young SW, “Magnetic susceptibility effects and their application in the development of new ferromagnetic catheters for magnetic resonance imaging.,” in *Invest Radiol*, ch. 25, pp. 1325–1332, 1990.

34. Bakker CJ, Hoogeveen RM, Weber J, van Vaals JJ, Viergever MA, Mali WP. “Visualization of dedicated catheters using fast scanning techniques with potential for mr-guided vascular interventions.,” in *Magn Reson Med*, ch. 36, pp. 816–820, 1996.

35. Miquel ME, Hegde S, Muthurangu V, et al. “Visualization and tracking of an inflatable balloon catheter using ssfp in a flow phantom and in the heart and great vessels of patients.,” in *Magn Reson Med*, ch. 51, pp. 988–995, 2004.

36. Kozerke S, Hegde S, Schaeffter T, Lamerichs R, Razavi R, Hill DL. “Catheter tracking and visualization using 19f nuclear magnetic resonance.,” in *Magn Reson Med*, ch. 52, pp. 693–697, 2004.

37. Dharmakumar R, Koktzoglou I, Tang R, Harris KR, Beohar N, Li D. “Off-resonance positive contrast imaging of a passive endomyocardial catheter in swine.,” in *Phys Med Biol*, ch. 57, pp. 475–484, 2008.

38. Edelman RR, Storey P, Dunkle E, et al. “Gadolinium-enhanced off-resonance contrast angiography.,” in *Magn Reson Med*, ch. 57, pp. 475–484, 2007.

39. Marc E. Miquel, Sanjeet Hegde, Vivek Muthurangu, Benjamin J. Corcoran, Stephen F. Keevil, Derek L.G. Hill, and Reza S. Razavi. “Visualization and tracking of an inflatable balloon catheter using ssfp in a flow phantom and in the heart and great vessels of patients.,”

40. Quick HH, Zenge MO, Kuehl H, Kaiser G.M., Aker S, Eggebrecht H, Massing S, Ladd M.E., “Wireless active catheter visualisation:passive decopling methods and their impact on catheter visibility.,” in *Proc. Intl. Soc. Mag. Reson. Med.*, ch. 13, 2005.

41. Kuehne T, Fahrig R, Butts K. “Pair of resonant fiducial markers for localization of endovascular catheters at all catheter orientations.,” in *J Magn Reson Imaging*, ch. 17, pp. 620–624, 2003.

42. Quick HH, Zenge MO, Kuehl H, et al. “Interventional magnetic resonance angiography with no strings attached: wireless active catheter visualization.,” in *Magn Reson Med*, ch. 53, pp. 446–455, 2005.

43. Eggers H, Weiss S, Boernert P, Boesiger P. “Image-based tracking of optically detunable parallel resonant circuits.,” in *Magn Reson Med*, ch. 49, pp. 1163–1174, 2003.

44. Wong EY, Zhang Q, Duerk JL, Lewin JS, Wendt M. "An optical system for wireless detuning of parallel resonant circuits.," in *J Magn Reson Imaging*, ch. 12, pp. 632–638, 2000.

45. Celik H, Uluturk A, Tali T, Atalar E. "A catheter tracking method using reverse polarization for mr-guided interventions.," in *Magn Reson Med*, ch. 58, pp. 1224–1231, 2007.

46. Dumoulin CL, Souza SP, Darrow RD. "Real-time position monitoring of invasive devices using magnetic resonance.," in *Magn Reson Med*, ch. 29, pp. 411–415, 1993.

47. Ocali O, Atalar E. "Intravascular magnetic resonance imaging using a loop-less catheter antenna.," in *Magn Reson Med*, ch. 37, pp. 112–118, 1997.

48. Kocaturk O, Kim AH, Saikus CE, et al. "Active two-channel 0.035" guide-wire for interventional cardiovascular mri.," in *J Magn Reson Imaging*, ch. 30, pp. 461–465, 2009.

49. Pictet J, Meuli R, Wicky S, van der Klink JJ. "Radiofrequency heating effects around resonant lengths of wire in mri.," in *Phys Med Biol*, ch. 47, pp. 2973–2985, 2002.

50. Ladd ME, Quick HH. "Reduction of resonant rf heating in intravascular catheters using coaxial chokes.," in *Magn Reson Med*, ch. 43, pp. 615–619, 2000.

51. Weiss S, Vernickel P, Schaeffter T, Schulz V, Gleich B. "Transmission line for improved rf safety of interventional devices.," in *Magn Reson Med*, ch. 54, pp. 182–189, 2005.

52. Bell JA, Saikus CE, Ratnayaka K, Wu V, Sonmez M, Faranesh AZ, Colyer JH, Lederman RJ, Kocaturk, O, "A deflectable guiding catheter for real-time mri guided interventions.," in *J Magn Reson Imaging*, ch. 35, pp. 908–915, 2012.

53. Schneck, JF, "The role of magnetic susceptibility in magnetic resonance imaging: Mri magnetic compatibility of the first and second kinds," in *Med. Phys*, ch. 23, pp. 815–850, 1996.

54. Barker GJ, Simmons A, Arridge SR, Tofts PS,"A simple method for investigating the effect of non-uniformity of radiofrequency transmission and radiofrequency in mri„" in *Br. J. Radiol.*, ch. 71, pp. 59–67, 1998.

55. Bentum PJM, Janssen JWG, Kentgens APM„ "Towards nuclear magnetic resonance l-spectroscopy and l-imaging„" in *Analyst*, ch. 129, pp. 793–803, 2004.

56. Webb, A., "Radiofrequency microcoils in magnetic resonance," in *Prog. Nucl. Magn. Reson. Spectrosc.*, ch. 31, pp. 41–42, 1997.

57. Mohmmadzadeh M, Baxan N, Badilita V, Kratt K, H. Weber , Korvink JG, Wallrabe U, Hennig J, von Elverfeldt, D, "Characterization of a 3d mems fabricated micro-solenoid at 9.4 t„" in *J Magn Reson*, pp. 20–26, 2011.

58. Demas V, Bernhardt A, Malba V, Adams KL, Evans L, Harvey C, Maxwell RS, Herberg JL, "Electronic characterization of lithographically patterned microcoils for high sensitivity nmr detection," in *Journal of Magnetic Reonance*, ch. 20, pp. 56–63, 2009.

59. Goloshevsky AG, Walton JH, Shutov MV, De Ropp JS, Collins SD, McCarthy M., "Development of low field nuclear magnetic resonance microcoils„" in *Review of Scientific Instruments*, pp. 76–78, 2005.

60. Walton JH, de Ropp J, Shutov MV, Goloshevsky,AG McCarthy MJ, Smith RL, S.D. Collins, “A micromachined double-tuned nmr microprobe,” in *Analytical Chemistry*, ch. 19, pp. 5030–5036, 2003.

61. Peck TL, Magin RL, Kruse J, Feng M,, “Nmr microspectroscopy using 100-lm planar rf-coils fabricated on gallium arsenide substrates,,” in *IEEE Transactions on Biomedical Engineering*, ch. 41, pp. 706–709, 1994.

62. Massin C, Boero C, Vincent F, Abenhaim J, Besse PA, Popovic RS, “High-q factor rf planar microcoils for micro-scale nmr spectroscopy,,” in *Sensors and Actuators A: Physical*, ch. 97, pp. 280–288, 2002.

63. Woytasik M, Grandchamp JP, Dufour-Gergam E, Gilles JP, Megherbi S, Martincic E, Mathias H, Crozat P, “Two- and three-dimensional microcoil fabrication process for three-axis magnetic sensors on flexible substrates,” in *Sensors and Actuators A: Physical*, pp. 2–7, 2006.

64. Sillerud LO, McDowell AF, Adolphi NL, Serda RE, Adams,DP, Vasile MJ, Alam TM, “H-1 nmr detection of superparamagnetic nanoparticles at 1 t using a microcoil and novel tuning circuit,,” in *Journal of Magnetic Resonance*, pp. 181–190, 2006.

65. Rogers JA, Jackman RJ, Whitesides G.M. “Constructing single- and multiplehelical microcoils and characterizing their performance as components of microinductors and microelectromagnets,” in *Journal of Microelectromechanical Systems*, ch. 6, pp. 184–192, 1997.

66. Rogers JA, Jackman RJ, Whitesides GM, Olson DL, Sweedler JV, “Using microcontact printing to fabricate microcoils on capillaries for high resolution proton nuclear magnetic resonance on nanoliter volumes,,” in *Applied Physics Letters*, ch. 70, pp. 2464–2466, 1997.

67. Malba V, Maxwell R, Evans LB, Bernhardt AE, Cosman M, Yan K, “Laser-lathe lithography a novel method for manufacturing nuclear magnetic resonance microcoils,,” in *Biomedical Microdevices*, ch. 5, pp. 21–27, 2003.

68. Jackson DD, Aracne-Ruddle C, Malba V, Weir ST, Catledge SA, Vohra YK, “Magnetic susceptibility measurements at high pressure using designer diamond anvils,,” in *Review of Scientific Instruments*, ch. 74, pp. 2467–2471, 2003.

69. S. Goto, T. Matsunaga, Y. Matsuoka, K. Kuroda, M. Esashi and Y. Haga, and Y. Haga, “Development of high-resolution intraluminal and intravascular mri probe using microfabrication on cylindrical substrates,” pp. 329–332, 2007.

70. J G Kim, N Takama, B J Kim and H Fujita, “Optical-softlithographic technology for patterning on curved surfaces.,” p. 19, 2009.

71. Dario Mager, Andreas Peter, Laura Del Tin, Elmar Fischer, Patrick J. Smith, JÃ$\frac{1}{4}$rgen Hennig, and Jan G. Korvink, “An mri receiver coil produced by inkjet printing directly on to a flexible substrate,,” in *IEEE Transactions On Medical Imaging*, ch. 29, 2010.

72. Li WJ and Mai JD, “Sensors and actuators on non-planar substrates,” in *Sensors and Actuators*, pp. 80–88, 1999.

73. Jackson DD, Aracne-Ruddle C, Malba V, Weir ST, Catledge SA, Vohra YK, “Magnetic susceptibility measurements at high pressure using designer diamond anvils,,” in *Review of Scientific Instruments*, pp. 2467–2471, 2003.

74. Nakagawa S, Ozasa H, and Misawa H,"Development of micro-wiring on the outer wall of a catheter,," in *The 1st Itn. Micromachine Symp*, pp. 123–126, 1995.

75. Jackman R J, Wilbur JL, and Whitesides GM, "Fabrication of submicrometer features on curved substrates by microcontact printing," in *Science*, ch. 269, pp. 664–666, 1995.

76. Hane K, Sasaki M, Hagihara T, and Nogawa S, "Rolling patterns transfer technique for lithography on cylindrical surface," in *IEEJ Technical meeting on sensors and micromachines*, ch. 10, pp. 47–51, 1998.

77. Joshima Y, Kokubo T, and Horiuchi T, "Application of laser scan lithography to fabrication of microcylindrical parts," in *J. J. Appl. Phys*, ch. 43, pp. 4031–4035, 2004.

78. Jacobsen SC, Wells DL, Davis CC, and Wood E, "Fabrication of micro-structures using non-planar lithography (npl)," in *Proc. of the Micro Electro Mechanical Systems*, pp. 44–50, 1991.

79. Richard G. Budynas, J. Keith Nisbett, "Shigley's mechanical engineering design, eigth edition," pp. 349–460, 2006.

80. Robert C. Junivall, Kurt M. Marshek, "Fundementals of machine component design," p. 423, 2008.

81. Richard G. Budynas, J. Keith Nisbett, "Shigley's mechanical engineering design, eigth edition," p. 403, 2008.

82. "https://tech.thk.com/en/products/thkdlinks.php?id=357."

83. "http://www.skf.com/group/products/bearings-units-housings/ball-bearings/deep-groove-ball-bearings/single-row-deep-groove-ball-bearings/single-row/index.html?designation=634-Zunit=metricUnit."

84. Jose Luis R. Arrondo, Alicia Alonso, "Advanced techniques in biophysics," pp. 1–27, 2006.

85. Kok Kiong Khan, Sunan Huang, "Precision motion control: Design and implementation," in *Advances in Industrial Control*, pp. 1–83, 2002.

86. "Conductive compounds, ag-610 technical datasheet," pp. 1–7, 2014.

87. J. Alonso, A. Soleilhavoup, A. Wong, A. Guiga, D. Sakellariou, "Double helix dipole design applied to magnetic resonance:a novel nmr coil," in *Journal of Mag. Res*, 2013.

88. Fink, Donald G.; Beaty, H. Wayne. "Standard handbook for electrical engineers (14th ed.)," pp. 2–50, 2000.